

RÉPUBLIQUE ALGÉRIENNE DÉMOCRATIQUE ET POPULAIRE
MINISTÈRE DE L'ENSEIGNEMENT SUPÉRIEUR ET DE LA RECHERCHE SCIENTIFIQUE

THÈSE

Présenté à l'Université de BISKRA

Faculté des Sciences Exactes, des Sciences de la Nature et de la Vie

Département de Sciences de la Matière

En vue de l'obtention du diplôme de

Doctorat en Physique

Par

Tibermacine Toufik

*Caractérisation des Défauts Profonds dans le Silicium Amorphe
Hydrogéné et autres Semiconducteurs Photo-Actifs de type III-V
par la Méthode de Photocourant Constant: CPM*

Soutenu le : 17/02/2011, devant le jury :

Pr. Sengouga Nouredine	Professeur	Président	Université de Biskra
Pr. Amar Merazga	Professeur	Directeur de thèse	Université de Taif, Arabie Saoudite.
Pr. Chahdi Mohamed	Professeur	Examineur	Université de Batna
Pr. Saidane Abdelkader	Professeur	Examineur	Université d'Oran
Pr. Aida Mohamed Salah	Professeur	Examineur	Université de Taibah, Arabie Saoudite.
Dr. Ledra Mohamed	M.C.(A)	Examineur	Université de Biskra

ACKNOWLEDGMENTS

I am greatly indebted to Dr. Merazga Amar for supervising my Doctorat thesis. He has offered me the occasion to realize the present thesis in Laboratory of Metallic and Semiconducting Materials (LMSM) at University of Biskra in Algeria. His advises and comments greatly helped me in my scientific life.

I am glad that I could visit Epicenter laboratory at University of Dundee in UK. I met there very freindly atmosphere. Especially, I wish to thank C. Main and S. Reynolds for their hospitality during a research visit to Dundee University where the CPM experiment has been done.

I am grateful to the Algerian Ministry of Higher Education and Research for support.

I also thank my family who supported me during my postgraduate studies.

Last, but not least, I would like to thank all my colleagues from LMSM laboratory, for fruitful cooperation and pleasant atmosphere at the laboratory.



Supervisor & me in front of

***EPICenter Laboratory
University of Abertay Dundee, UK.***

ملخص

الهدف من مذكرة الدكتوراه هو تحديد الخواص الضوئية المتمثلة في معامل الإمتصاص الضوئي ($\alpha(h\nu)$) و الخواص الإلكترونية المتمثلة في التوزيع الطاقوي لكثافة الحالات الإلكترونية (DOS) لمجموعة من العينات التالية: السيليسيوم اللامتبلور المهدرج (a-Si:H)، الميكرو سيليسيوم المهدرج (μ -c-Si:H) و زرنيخيد الغاليوم المطعم بالكروم (SI-GaAs:Cr). من أجل هذه الغاية قمنا بقياس معامل الإمتصاص لهذه العينات باستعمال طريقة تثبيت التيار الضوئي (CPM) من خلال تغيير شدة الضوء المسلط بنمطين مختلفين: نمط مستمر (DC-CPM) و نمط متناوب (AC-CPM) باستعمال ترددات مختلفة. إنطلاقاً من هذه القياسات قمنا باستخراج التوزيع الطاقوي لكثافة الحالات الإلكترونية لهذه العينات داخل الفاصل الطاقوي ("gap"). لاحظنا اختلاف فيما يخص معامل الإمتصاص المقاس و كثافة الحالات الإلكترونية العميقة المستخرجة بين النمط DC و النمط AC من جهة وبين مختلف ترددات الضوء المستعملة في النمط AC. إلى جانب ذلك قمنا بدراسة تأثير الضوء الشديد المسلط لمدة طويلة على خصائص هذه العينات. لاحظنا أن معامل الإمتصاص يزداد كلما زادت مدة تسليط الضوء الشديد إلى جانب ارتفاع في قيمة كثافة الحالات الإلكترونية العميقة إلى غاية التشبع لكن بنسب مختلفة بين كثافة الحالات الإلكترونية السلبية (D^-) و الحيادية (D^0).

إلى جانب القياسات قمنا بانجاز برنامج يقوم بمحاكاة رقمية للتقنية CPM في النمط DC و AC بحيث أخذنا بعين الإعتبار كل الإنتقالات الحرارية و الضوئية الممكنة بين الحالات الإلكترونية المتمركزة داخل الفاصل الطاقوي بناء على نموذج "Defect Pool" و عصابتي التكافؤ و النقل. المحاكاة الرقمية بينت لنا من جهة الإختلاف بين النمطين DC و AC الملاحظ في التجربة، و كشفت لنا من جهة أخرى أهمية الأخذ بعين الإعتبار معاملي الإمتصاص الضوئي الناتجين عن الإلكترونات الحرة من جهة و الثقوب الحرة من جهة أخرى. بالفعل المحاكاة الرقمية بينت لنا، في حالة النمط AC، إمكانية استعمال معامل الإمتصاص الضوئي الناتج عن الإلكترونات الحرة لتحديد التوزيع الطاقوي لكثافة الحالات الإلكترونية المملوءة القريبة من حدود عصابة التكافؤ بينما يمكن استعمال معامل الإمتصاص الضوئي الناتج عن الثقوب الحرة لتحديد التوزيع الطاقوي لكثافة الحالات الإلكترونية الشاغرة القريبة من حدود عصابة النقل.

الكلمات المفتاحية: معامل الإمتصاص الضوئي، كثافة الحالات الإلكترونية، a-Si:H، μ -c-Si:H، SI-GaAs:Cr، DC-CPM، AC-CPM.

ABSTRACT

We present in this thesis the optical and electronic properties of a number of semiconductor materials namely undoped and P-doped hydrogenated amorphous silicon a-Si:H prepared by Plasma Enhanced Chemical Vapour Deposition (PECVD), hydrogenated micro-crystalline silicon ($\mu\text{c-Si:H}$) prepared by Very High Frequency Plasma-Enhanced Chemical Vapor Deposition (VHF-PECVD) and semi-insulating Cr-doped GaAs (SI-GaAs:Cr) prepared by the Liquid Encapsulated Czochralski (LEC) method. Sub-band gap optical absorption spectra α ($h\nu$) of all samples have been measured by the constant photocurrent technique in dc and ac excitation (dc-CPM and ac-CPM). Then, these absorption coefficients are converted into electronic density of states (DOS) distribution within the mobility gap by applying the derivative method of Pierz et al. We present in this thesis the relationship between the optical excitation frequency and the optical and electronic properties of semiconductors materials in particular a-Si:H, $\mu\text{c-Si:H}$ and GaAs.

We have developed a code program to simulate the dc and ac-CPM sub-band-gap optical absorption spectra. This numerical simulation includes all possible thermal and optical transitions between extended states and gap states. Our numerical results shows that (i) a discrepancy between dc mode and ac mode in absorption spectrum and gap state distribution particularly in defect region; (ii) extraction of DOS distribution using ac mode is better than using dc mode specially at high frequency (iii) DOS distribution can be reasonably reconstructed over a wide range of energy, especially at ultra high frequency, using both $\alpha_n(h\nu)$ $\alpha_p(h\nu)$ corresponding to optical transitions associated with free electrons and free holes creation, respectively. In addition and to validate our simulation results, we have measured α ($h\nu$) for all samples at several frequencies. Our experimental results prove the simulation ones and showed that a significant difference between dc- and ac-absorption spectra is observed in defect region and that the determination of the density of the occupied states within the gap mobility of the material is better for high frequencies than for low frequencies. The evolution of the sub-band-gap absorption coefficient α ($h\nu$) and the CPM-determined density of gap-states distribution within the gap versus the illumination time leads to: (i) an increase in the deep defect absorption without any significant changes in the Urbach tail (exponential part), (ii) a presence of more charged than neutral defects as predicted by the

defect pool model, and (iii) a saturation point of the degradation of both optical absorption coefficient and density of deep states of slightly P-doped sample measured by *dc-CPM*. The constant photocurrent technique in dc-mode as a spectroscopy method for the defect distribution determination is, therefore, most reliable to study the light soaking effect on the stability of hydrogenated amorphous silicon layers used in solar cells manufacturing.

The constant photocurrent method in the ac-mode (*ac-CPM*) is also used in this work to determine the defect density of states (DOS) in microcrystalline silicon ($\mu\text{c-Si:H}$) and to investigate the defect levels of semi-insulating Cr-doped GaAs from the optical absorption spectrum. The microcrystalline absorption coefficient spectrum $\alpha(h\nu)$ is measured under *ac-CPM* conditions at 60Hz and then is converted by the *CPM* spectroscopy into a DOS distribution covering a portion in the lower energy range of occupied states. By deconvolution of the measured optical absorption spectrum of SI-GaAs: Cr, we have extracted the distribution of the deep defect states. Independently, computer simulations of the *ac-CPM* for both materials are developed. Using a DOS model for microcrystalline which consistent with the measured *ac-CPM* spectra and a previously measured transient photocurrent (TPC) for the same material, the total *ac- $\alpha(h\nu)$* is computed and found to agree satisfactorily with the measured *ac- $\alpha(h\nu)$* . Using a DOS model for gallium arsenide which consistent with the measured *ac-CPM* spectra and a previously measured modulated photocurrent (MPC) for the same material, the total *ac- $\alpha(h\nu)$* is computed and found to agree satisfactorily with the measured *ac- $\alpha(h\nu)$* . The experimentally inaccessible components $\alpha_n(h\nu)$ and $\alpha_p(h\nu)$, corresponding to optical transitions associated, respectively, with free electron and free hole creation, are also computed for both semiconductors. The reconstructed DOS distributions in the lower part of the energy-gap from $\alpha_n(h\nu)$ and in the upper part of the energy-gap from $\alpha_p(h\nu)$ fit reasonably well the DOS model suggested by the measurements. The results are consistent with a previous analysis, where the sub-gap *ac- $\alpha(h\nu)$* saturates to a minimum spectrum at sufficiently high frequency and the associated DOS distribution reflect reliably and exclusively the optical transitions from low energy occupied states.

Keywords: a-Si:H; $\mu\text{c-Si:H}$; SI-GaAs:Cr; *ac-CPM*; *dc-CPM*; Optical Absorption Spectrum; Deep Defect Density; Light Soaking.

RESUME

Le but de ce travail est de déterminer les propriétés optiques et électroniques en termes de coefficient d'absorption optique et densité d'états électronique d'un certain nombre de semi-conducteurs à savoir le silicium amorphe hydrogéné (a-Si:H), silicium microcristallin ($\mu\text{-Si:H}$), arséniure de gallium dopé au chrome (SI-GaAs:Cr). Pour cette raison, on a mesuré le coefficient d'absorption optique des échantillons par la méthode de photo-courant constant en régime continu (DC-CPM) et en régime périodique (AC-CPM) pour plusieurs fréquences d'excitation optique. Ensuite on a convertit les spectres d'absorption mesurés en densité d'états électronique à l'intérieure du gap de mobilité. Une différence est observée concernant le coefficient d'absorption optique et la densité d'états profonds entre le régime périodique et le régime continu d'un coté et entre les différentes fréquences d'un autre coté. On a aussi, mesuré l'évolution du coefficient d'absorption et la distribution d'états électronique avec l'illumination. Cette mesure montre une augmentation de la densité de défauts profonds, une présence de défauts chargés plus importante que les défauts neutre et une saturation pour des temps d'illuminations très longues. En outre, on a développé un programme pour modéliser la technique CPM en mode DC et AC qui tient en compte toutes les transitions optiques possibles. Notre modélisation nous a démontré l'importance de considérer les deux coefficients d'absorption celles du aux électrons et celle due aux trous. Ceci est essentiel pour reconstituer la distribution des états occupés et non occupés en utilisant ces deux coefficients surtout pour des hautes fréquences. Au fur et à mesure que la fréquence augmente, les propriétés optiques en termes de spectre d'absorption optique sont plus en plus sous-estimées quand aux propriétés électroniques en termes de densité d'états électronique sont plus en plus bien déterminées.

Mots clés : Spectre d'absorption optique ; Densité des défauts profonds ; a-Si:H ; $\mu\text{-Si:H}$; SI-GaAs :Cr ; AC-CPM ; DC-CPM ; Illumination Intense.

TABLE OF CONTENTS

Title	i
Acknowledgements	ii
Abstract	v
Table of contents	viii

Chapter 1. General introduction

1.1. Introduction	1
1.2. Background and Motivation	3
1.3. Objectives and outline of the thesis	6
References	

Chapter 2. Introduction to amorphous semiconductors

2.1. Introduction	11
2.2. Fundamental properties of hydrogenated amorphous silicon	11
2.2.1. Structural properties	11
2.2.2. Electronic structure	18
2.2.3. Effects of doping	22
2.2.4. Metastability and Staebler-Wronski effect	24
2.2.5. Optical properties of a-Si:H	25
2.2.6. Mechanisms of transport	29
2.2.7. Phenomena of recombination	30
2.3. Fundamental properties of hydrogenated micro crystalline silicon	31
2.3.1. Deposition methods of hydrogenated micro crystalline silicon	31
2.3.2. Atomic structure	31
2.3.3. Electrical and optical properties	32
2.3.4. Advantages of μc -Si:H	33
References	

Chapter 3. Characterization techniques of amorphous semiconductors

3.1. Introduction	37
3.2. Dark conductivity	38
3.3. Steady state photoconductivity	40
3.4. Constant photocurrent measurement	44
3.5. Photothermal deflection spectroscopy	49
3.6. Dual beam photoconductivity	52
References	

Chapter 4. Constant photocurrent technique: Theory and modeling

4.1. Introduction	57
4.2. Density of states distribution models for a-Si:H	57
4.3. Trapping and recombination	63
4.4. Absorption and generation	65
4.5. Function occupancy	70
4.5.1. Thermal equilibrium	70
4.5.2. Steady state equilibrium	71
4.5.3. Dynamic equilibrium	73
4.6. Implementation of numerical model	74
4.6.1. Steady state equilibrium: DC contribution	74
4.6.2. Dynamic equilibrium: AC contribution	76
4.6.3. Deconvolution procedure	78
References	

Chapter 5. Constant photocurrent technique: Results and discussion

5.1. Introduction	81
5.2. Experimental procedure	82
5.3. Dark conductivity and activation energy measurements	85
5.4. Reflectance-Transmittance measurements	88
5.5. Optical absorption spectrum measurement: Constant Photocurrent Method	91
5.6. Density of states	95
5.7. Results and discussion	96
5.7.1. Hydrogenated amorphous silicon a-Si :H: Undoped sample Intersolar ISB4	96
5.7.2. Hydrogenated amorphous silicon a-Si :H: Doped sample : P272	104
5.7.3. Hydrogenated micro-crystalline silicon μ c-Si :H : OCC354 sample	109
5.7.4. Semi-insulating Cr doped Gallium arsenide :SI- GaAs :Cr sample 1713	117
5.7.5. Ultra high frequency effect	121
5.7.6. Light Soaking effect	123
References	

Chapter 6. Summary and conclusions

6.1. Conclusions	129
6.2. Suggestions for further work	132
Appendix A	136
Appendix B	139
Appendix C	141
Appendix D	142
Appendix E	143
Appendix F	145

CHAPTER 1

GENERAL INTRODUCTION

1.1. Introduction

Solar cell technology is an attractive alternative to conventional sources of electricity for it provides non-polluting and renewable energy. Due to the dwindling supply of fossil fuels and the environmental concerns, demand for new sources of energy is ever increasing worldwide. Though solar cells hold the promise of clean and renewable source of energy, the cost aspect of the solar cell technology has been a drawback to the wide-spread use of solar cells. However, the recent advances in realizing a lower cost of solar cells will eventually lead to a significant impact of solar cells on to the global energy market. In thin-film silicon solar cells, the deposited silicon is a different phase compared to crystalline silicon c-Si: it is hydrogenated amorphous silicon ($a\text{-Si:H}$) or hydrogenated microcrystalline silicon ($\mu\text{c-Si:H}$). Most solar cells are made from single crystalline silicon. The production of single crystal silicon cells is very costly and the cells made from it have several other factors that limit the extent to which the costs can be further reduced. The absorptivity of single-crystal silicon is very low requiring thick cells in order to achieve the required efficiency. This makes single-crystalline cells rather expensive to produce.

Amorphous silicon may provide the answer to inexpensive production of solar cells. The absorptivity of amorphous silicon is far greater than that of single-crystal silicon. Therefore, $a\text{-Si:H}$ solar cells can be made very thin $d \sim 0.5 \mu\text{m}$. The other advantages of amorphous silicon solar cells is the extreme abundance of the raw material from which they can be made and the low fabrication temperatures which facilitate the use of a variety of low-cost substrates. Based on this concept, in 1976 the first experimental $a\text{-Si:H}$ $p\text{-i-n}$ solar cell was made by Carlson and Wronski with an energy conversion efficiency of 2.4%. Nowadays, such cells can be made with initial conversion efficiencies η greater than 10%.

The drawback of amorphous silicon based solar cells is that their efficiencies appear to be considerably less than their crystalline counterparts. Another problem is that amorphous silicon suffers from light induced metastable effects known as Staebler-Wronski effect (SWE). This means that upon illumination the material degrades over time, reducing the percentage of light that can be converted to electricity. Despite this drawback, the low cost of this material and the attractiveness of large area production still makes amorphous silicon ideally suited for low cost solar cells. The improvements in the stabilized efficiency of a-Si:H have been achieved mostly through material improvements, adopted cell designs and light trapping techniques. This still leaves many fundamental questions unanswered regarding the growth and material properties of amorphous silicon as well as the electronic characteristics of the solar cells.

Recently, hydrogenated microcrystalline silicon ($\mu\text{c-Si:H}$) has attracted much interest for being used in optoelectronic applications. As compared to hydrogenated amorphous silicon (a-Si:H), it offers a higher stability against light and current induced degradation and a wider absorption bandwidth extending into the near infrared. In 1992 Faraji *et al.* reported a thin-film silicon solar cell with a $\mu\text{c-Si:H:O}$ *i*-layer. The first solar cell with a $\mu\text{c-Si:H}$ *i*-layer was reported in 1994 by Meier *et al.* at IMT Neuchâtel, Switzerland with $\eta = 4.6\%$. In the following years, at this institute the concept of “micromorph” tandem cells was developed: a tandem with a microcrystalline bottom cell and an amorphous top cell. In 2002, Meier *et al.* published a micromorph tandem with $\eta = 10.8\%$ stable (12.3% initial) of which the bottom cell (thickness of $d = 2 \mu\text{m}$) was deposited at a rate of $rd = 0.5 \text{ nm/s}$. The highest initial efficiency of 14.7% was reported by Yamamoto *et al.* of Kaneka, Japan. Because of the fact that not only the efficiency but also the manufacturing costs of the solar cell determine the feasibility as an industrial product, the trend in research has moved towards higher deposition rates, while reducing the loss in material properties and cell performance to a minimum.

Further development and optimization of a-Si:H/ $\mu\text{c-Si:H}$ tandems will remain very important because it is expected that in the near future (first half of this century) its market share will be considerable. For example, in the European Roadmap for PV R&D, it is predicted that in 2020 the European market share for thin-film silicon (most probably mainly a-Si:H/ $\mu\text{c-Si:H}$ tandems) will be 30%. This shows the importance of second generation solar cells.

1.2. Background and Motivation

One of the central issues of the physics of amorphous solids is the nature of the band tails in the electronic density of states (DOS). Particular issues include the following: (i) what is the origin of the exponential shape of the tails seen in optical absorption measurements? (ii) How does the spatial character of the electronic eigenstates change from the highly local midgap states to the extended states interior to the valence or conduction bands? The nature of the electronic states for electron energies ranging between midgap (localized) to valence or conduction (extended) is of obvious interest to the theory of doping and transport.

Hydrogenated amorphous silicon (a-Si:H)

Hydrogenated amorphous silicon (a-Si:H) was discovered by Chittick et al in 1969 and the possibility of doping was demonstrated by Spear and LeComber in 1975. Since then, hydrogenated amorphous silicon is extensively used in diverse optoelectronic applications. This material is nowadays used for sensors, for thin film transistors, and not in the least for solar cells. a-Si:H has particular properties such as adjustable gap mobility by combining it with nitrogen, carbon or germanium, direct band gap, absorption in the visible wavelength region is about 100 times higher than that of crystalline silicon, easy to prepare on glass substrates and at low temperatures, can be directly produced in a form that can cover a very large area.

Hydrogenated amorphous silicon is the non-crystalline form of silicon. In the crystalline state, the atoms form a periodic array with each one bonded to four others; the bond lengths and angles are similar for each atom and long range order exists. In the amorphous state, the long range order does not exist. There is, however, still short-range order, i.e., most silicon atoms have four neighbors in a nearly diamond like structure. As a result of the short-range order, a-Si:H has a band structure and the common semiconductor concept of conduction and valence bands can be used. However, the absence of long-range order means that these bands are not sharp and have tails that extent into the band gap. Physically these band tails represent energy levels of strained silicon-silicon bonds, resulting from bond-angle and/or bond-length distributions. The width of these band tails is more or less a measure for the amount of disorder in the material. In addition to the band tails there is a quasi-continuum of states throughout the band tails related to broken bonds, usually referred to as dangling bonds.

These dangling bonds can capture charge carriers and have three charge states: the D^- has two electrons, the D^0 has one electron and the D^+ has no electrons. Fortunately most of these dangling bonds are passivated by hydrogen that is incorporated most commonly through the process of Plasma Enhanced Chemical Vapor Deposition (PECVD) and hence the dangling bonds density is reduced from about 10^{21} cm^{-3} in pure amorphous silicon (a-Si) to 10^{15} cm^{-3} , i.e., less than 1 dangling bond per million atoms. Although hydrogenated amorphous silicon contains more hydrogen than defects, still not all the defects are passivated. Presently, the general agreement is that there is equilibrium between the width of the tail states (i.e., the density of weak or strained Si-Si bonds) and the defect density. Unfortunately, D. Staebler and C. Wronski discovered, more than 30 years ago, the degradation of the electronic properties of a-Si:H under prolonged illumination by an intense light. Even at moderate light intensities (e.g., by exposure to sunshine), the dark conductivity and photoconductivity can be significantly reduced. This Staebler-Wronski effect increase the number of dangling bonds through a mechanism for the breaking of weak Si-Si bonds from less than 10^{16} cm^{-1} in as deposited intrinsic layers to about 10^{17} cm^{-1} in degraded layers.

Hydrogenated microcrystalline silicon ($\mu\text{c-Si:H}$)

Hydrogenated microcrystalline silicon ($\mu\text{c-Si:H}$) appears to be a more stable alternative. $\mu\text{c-Si:H}$ was first reported by Veřprek *et al.* in Europe in 1968 and in Japan by Matsuda *et al.* and Hamasaki *et al.* in 1980. The electronic properties and performance of $\mu\text{c-Si:H}$ films are correlated with the deposition parameters and the structural properties. It is in fact heterogeneous in nature, which leads to difficulties in the explanation of its electronic transport properties. Therefore, the detailed knowledge of the gap density of states (DOS) in $\mu\text{c-Si:H}$ is of great importance to understand the transport mechanism. However, as $\mu\text{c-Si:H}$ is a phase mixture of crystalline and amorphous regions separated by grain boundaries and voids, little is known about the nature and the energy distribution of the DOS. It is therefore not surprising if there exists no conclusive DOS map and the understanding does not go in many cases beyond a phenomenological description. In contrast to crystalline silicon, the presence of band-tail states and deep defects opens additional transport paths that might act as traps or form barriers for charge carriers. There is a wide range of possible structures in $\mu\text{c-Si:H}$ material which explain the large spread in reported drift mobilities and transport

properties, but the similarity between $\mu\text{-Si:H}$ and a-Si:H suggest that structural disorder is common feature and transport in $\mu\text{-Si:H}$ might take place by trap-limited band motion (multiple trapping) or by direct tunneling between localized states (hopping) at low temperature.

Constant Photocurrent Method: CPM

The tail states and the dangling bonds have a large effect on the electronic and optical properties of amorphous semiconductors. Sub-band gap absorption coefficient of these materials can provide useful information on their electronic transport and optical properties. It can be used to infer the spectral distribution of the density of gap states of such materials. Many sub-band gap absorption spectroscopy methods have been applied in order to determine DOS but the sensitivity of each technique is not the same in the different regions of the band gap. The most extensive are the constant photocurrent method (CPM), the photo-thermal deflection spectroscopy (PDS) and the dual beam photoconductivity (DBP) which have been used to evaluate the DOS in the lower energy range of the band gap near the valence band, whereas the transient photoconductivity (TPC) and the modulated photocurrent (MPC) have been used to determine the DOS in the upper energy range of the gap, close to the conduction band.

The constant photocurrent method was originally developed for crystalline semiconductors and then applied to amorphous materials by Vanecek et al. in 1981. CPM is one of the sub-band gap absorption measurements used to characterise N-type, intrinsic or P-type a-Si:H materials. By means of this optical spectroscopy method we can measure the sub-band gap optical absorption spectrum of amorphous semiconductor using steady (dc-CPM) or modulated (ac-CPM) sub-gap illumination. This latter gives us access to the density of states since photons can excite electrons from filled defect states to the conduction band or from the valence band to the empty defect states. Unfortunately, this technique is based on a number of assumptions, causing its applicability and validity to have often been questioned. Bube et al. noted that to determine the midgap defect densities the dc-CPM have to be corrected. Mettler et al. concluded that there is a “working point” at which the basic CPM conditions are fulfilled. Zhang et al. found that an inhomogeneous spatial distribution of defects have a strong influence on the CPM determined defect density. Schmidt et al. reported that the

absorption coefficient measured with dc-CPM is dependent on the constant photocurrent chosen to perform the measurement. The constant photocurrent method can be also performed in the ac mode where the sub-band-gap excitation light is chopped at different frequencies. Nevertheless, discrepancies between the dc and ac modes have been observed and studied by several authors. Conte et al. reported the discrepancy between measurements by dc and ac-CPM and also observed experimentally the dependence of the dc-CPM spectra on the magnitude of the adopted constant photocurrent. Sládek and Thèye found that the difference between dc and ac measurements results by the fact that the response time of the photocurrent is too slow and reduces with photon energy at room temperature since the difference disappear at low temperatures. Hasegawa et al. found this difference and concluded that the response time increase for low value of $h\nu$. Main et al. in recent work explained this discrepancies in terms of the relative contribution of phonon assisted transitions in the generation process. Following these different interpretations, one can conclude that the subject is still open to discussion and needs more explanations.

1.3. Objectives and outline of the thesis

Defect levels in semiconductor band gaps determine the electrical and optical properties devices. These properties are determined by the relative position of the level and the capture cross section of the carriers. The defect levels can capture minority, majority carriers or both carriers for the deep states in this case they act as recombination centers. Capture and emission of majority and minority carriers at defect levels in semiconductors materials are characterized, most usually, by DLTS and MCTS. For semi-insulating (SI) crystals like GaAs and amorphous materials like a-Si:H and $\mu\text{c-Si:H}$ other techniques must be used such as TPC, MPC and CPM.

On the simulation side, great effort was deployed to model the TPC in a-Si:H and $\mu\text{c-Si:H}$, while modeling has been less employed to elucidate the experimental results of the CPM technique in a-Si:H and $\mu\text{c-Si:H}$, particularly in the ac mode.

In a previous ac-CPM analysis, Main et al demonstrate that the ac-CPM may be more reliable than the dc-CPM in probing the DOS distribution in disordered semiconductors in the energy range of occupied states below the Fermi-level. In this analysis, the electron transitions fall into two categories, the direct optical transitions from occupied states below the Fermi-level

to the conduction band, creating free electrons (Fig. 1 (a)), and the indirect double transitions where electrons are optically excited from the valence band to unoccupied states above the Fermi-level and from there are thermally emitted to the conduction band (Fig. 1 (b)). As the chopper frequency increases, the thermal emissions with frequencies lower than the chopper frequency cause the corresponding indirect transitions to loose contribution to the ac-photocurrent. This requires increasing the photon flux to maintain the ac-photocurrent constant, which lowers the absorption coefficient. Thus, at sufficiently high chopper frequency, comparable to the highest emission frequency from the shallowest energy level, all the indirect transitions loose participation to the ac-photocurrent. This requires maximum photon flux spectrum to keep the photocurrent constant, leading to a minimum $ac-\alpha(h\nu)$. It is evident that the DOS distribution associated with this minimum $ac-\alpha(h\nu)$ reflects reliably the direct transitions from deep energy occupied states. However, one might argue that the indirect transitions generate free holes which have been ignored in this simple one carrier type (electron) analysis and could contribute to the ac-photocurrent, which might have effect on the analysis.

In the present work, we use the dc-CPM and ac-CPM to measure the $dc-\alpha(h\nu)$ and $ac-\alpha(h\nu)$ in VHF-PECVD-prepared a-Si:H and μc -Si:H and apply the derivative method of Pierz et al to convert the measured data into a DOS distribution in the lower part of the energy-gap. We complete the μc -Si:H DOS model, in the upper part of the energy-gap, by previous DOS data based on transient photocurrent (TPC) spectroscopy and, around the mid-gap, by a-Si:H-like dangling bond defect DOS with appropriate parameters from literature. On the basis of the complete DOS model, we develop numerical simulations of the dc-CPM and ac-CPM, as a generalisation to Main analysis to include both carrier types in the absorption and transport processes. We compute the components dc & $ac-\alpha_n(h\nu)$ and dc & $ac-\alpha_p(h\nu)$, of the total dc & $ac-\alpha(h\nu)$, corresponding to electron transitions, respectively from filled states in the lower energy range to the conduction band (free electron creation) and from the valence band to empty states in the upper energy range (free hole creation). We then use the derivative method of Pierz et al to reconstruct from each component the corresponding DOS distribution. It turns out that the reconstructed DOS is a good fit to the DOS model partially suggested by the DOS portions determined from the measured total $ac-\alpha(h\nu)$ and total TPC. It will then be

concluded that the measured $\text{ac-}\alpha(h\nu)$ is mainly due to direct optical transitions of the electrons occupying the defect states in the lower half of the gap.

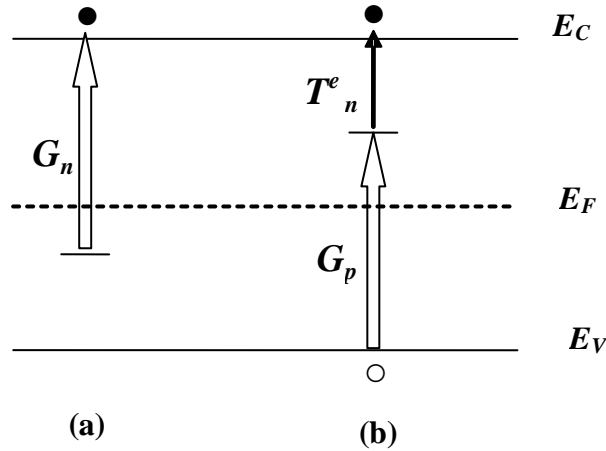


Figure 1. Two optical transition categories according to Main ac-CPM analysis:

- (a) Direct transitions creating free electrons (\bullet) with rate $G_n(E, h\nu, \omega)$.
- (b) Indirect double transitions creating free holes (\circ): an optical transition from the valence band to an empty state at E above E_F , with rate $G_p(E, h\nu, \omega)$, followed by a thermal transition from E to the conduction band with rate $T_n^e(E)$.

In this thesis, we combine experimental and computer modeling studies aimed at understanding the difference between two modes dc and ac-CPM of amorphous silicon, microcrystalline silicon and III-V semiconductors particularly Si GaAs Cr doped. The scope of the thesis encompasses the application of the microscopic models describing the distribution of midgap defect states to numerical simulations of the optical absorption coefficient of a set of semiconductors. We have developed computer modeling schemes for simulating the CPM technique of amorphous and microcrystalline silicon films taking into account the nature and distributions of dangling bond states depicted by defect pool model. Specific research objectives of this thesis therefore include (1) experimental understanding of constant photocurrent measurements in the steady and periodic regime of several semiconductors materials ; (2) development of a simulation technique for CPM experiment taking into account all possible optical and thermal transitions between localized and extended states ; (3) the understanding of the dc and ac contributions in the measured and

simulated absorption spectra by means of CPM technique ; (4) the understanding of the dc and ac contributions in the measured and simulated density of states by means of CPM technique.

Therefore, we propose in this thesis to study by simulation and experimentation the electronic structure, represented by the defects density, in the a-Si:H, $\mu\text{c-Si:H}$ and other semiconductor materials of the type III-V, by means of the Constant Photocurrent Method (CPM). The present thesis is structured into five chapters. Chapter 2 deals with the review of literature which gives the necessary background for the approach undertaken in this study. It covers the properties of amorphous materials that are the deposition methods, atomic and electronic structure and optical properties. Chapter 3 gives the principle of a diverse sub-band gap absorption experiments used to characterize disorder semiconductors such as photothermal deflection spectroscopy or PDS and dual beam photoconductivity or DBP. Chapter 4 explains the modeling approach, describing the electrical and optical modeling of a-Si:H and $\mu\text{c-Si:H}$ films using dc-CPM and ac-CPM modes. This include the dc and ac optical absorption spectrum and electronic states distribution within the gap of a-Si:H, $\mu\text{c-Si:H}$ and SI-GaAs:Cr. The contribution of the continuous regime (dc mode) and the periodic regime (ac mode) for numerical modeling of the constant photocurrent method in both modes are also given in this chapter. Chapter 5 is the last chapter, it covers a detailed discussion of the different results obtained from modeling and experimentations in both modes ac and dc and compares between them in terms of absorption spectrum and distribution and density of states within the gap of a-Si:H, $\mu\text{c-Si:H}$ and SI-GaAs:Cr films. Finally at the end of this present work, we present the conclusions and perspectives of future work pertaining to the study of a-Si:H, $\mu\text{c-Si:H}$ and III-V materials.

REFERENCES

- [1] H. Matsuura, “Electrical properties of amorphous/crystalline semiconductor heterojunctions and determination of gap-state distributions in amorphous semiconductors”, Ph.D.thesis, Kyoto University, Japan, 1994.
- [2] D. P. Webb, “Optoelectronic properties of amorphous semiconductors”, Ph.D.thesis, University of Abertay, Dundee, UK, October 1994.
- [3] K. Haenen, “Optoelectronic study of phosphorous-doped n-type and hydrogen-doped p-type CVD diamond films”, Ph.D.thesis, Limburgs Universitair Centrum, Belgium, 2002.
- [4] S. Heck, “Investigation of light-induced defects in hydrogenated amorphous silicon by low temperature annealing and pulsed degradation”, PhD Thesis, der Philipps-Universität Marburg, Marburg/Lahn 2002.
- [5] F. R. Shapiro, “Computer simulation of the transient response of amorphous silicon hydride devices”, PhD thesis, Massachusetts institute of technology, UK, May 1998.
- [6] A. Merazga, “Steady state and transient photoconductivity in n-type a-Si”, Ph.D.thesis, Dundee Institute of Technology, Dundee, UK, 1990.
- [7] A. Mettler, “Determination of the deep defect density in amorphous hydrogenated silicon by the constant photocurrent method: A critical verification”, Ph.D. thesis, faculty of sciences, university of Neuchatel, Switzerland (1994).
- [8] I. Zrinscak, “Application and analysis of the constant photocurrent method in studies on amorphous silicon and other thin film semiconductors”, Ph.D.thesis, University of Abertay, Dundee, UK, June 2005.
- [9] N. Sengouga, “Hole traps in GaAs FETs: Characterization and backgating effects”, Ph.D.thesis, Lancaster University, UK, 1991.
- [10] Zdenek Remes, Ph.D. thesis, “Study of defects and microstructure of amorphous and microcrystalline silicon thin films and polycrystalline diamond using optical methods”, faculty of mathematics and physics, Charles university, Prague, Czech Republic, 1999.

CHAPTER 2

INTRODUCTION TO AMORPHOUS SEMICONDUCTORS

2.1. Introduction

Amorphous silicon belongs to the family of the semiconductors; it is often compared with crystalline silicon in terms of advantages and disadvantages. The great advantages which it offers this material are the possibility of depositing it on great non-plane and flexible surfaces, a facility of manufacture and a strong absorption of the light. However, it has low free carriers mobilities, much of defects in the structure and its electric properties are degraded under continuous illumination. In the following sections, we will present a brief review concerning the methods of deposition and the structural and physical properties of amorphous materials particularly hydrogenated amorphous silicon (a-Si:H) and hydrogenated microcrystalline silicon ($\mu\text{c-Si:H}$).

2.2. Fundamental properties of hydrogenated amorphous silicon

2.2.1 Structural properties

A. Deposition methods of hydrogenated amorphous silicon

The search for a-Si:H with improved properties (low defect density, higher carrier mobility, enhanced stability, etc) has led researchers to explore a large number of deposition methods and the effects of each process parameters. There are several techniques of amorphous silicon deposition in thin layer of which most usually used are those which are based on the chemical

decomposition in gas phase or CVD. One can quote the CVD assisted by plasma or PECVD and the CVD with hot wire or HWCVD. The other methods are those which are based on the epitaxy, thermal evaporation and cathode sputtering [1, 2].

Figure 2.1 schematically describes the processes involved in a-Si:H deposition, which can be decomposed into four steps: [2]

- The dissociation of the gas precursors;
- The plasma physics and chemistry, which determine the flux and nature of reactive species to the substrate;
- The plasma-surface interactions;
- The reactions taking place in a growth-zone where cross-linking reactions result in the formation of the film.

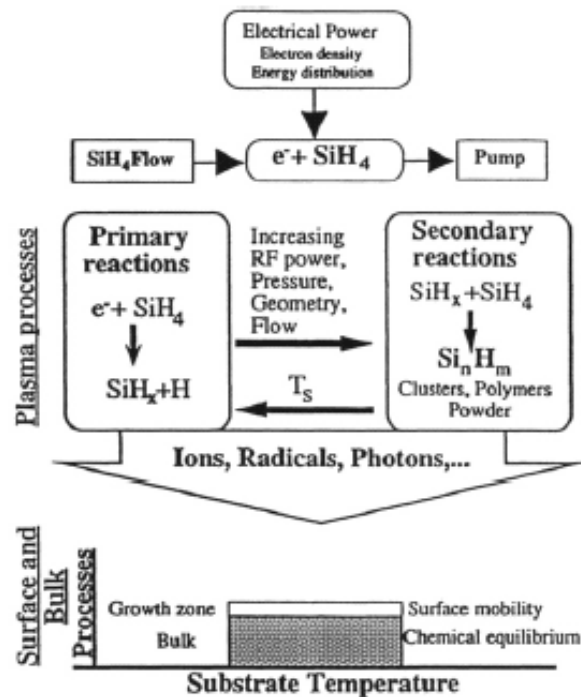


Figure 2.1: Schematic representation of the processes involved in a-Si:H deposition.

The PECVD method consists in dissociating, through a vacuum chamber containing two electrodes, the gas of silane SiH_4 injected with low pressure (0.1 to 10 Torr) in very active chemical elements. The formed plasma results from the electric discharge between the electrodes by applying an alternative electric field of a frequency generally equal to

13.56MHz. It contains the radicals Si, Si-H, Si-H₂; Si-H₃ accompanied by the positive and negative ionic species and the electrons what ensures total electric neutrality.

Turban [3] studied the chemical reactions and the mechanisms of dissociation of silane in such plasma. The ionized molecules are deposited on the heated substrate (150-300°C) by forming a thin film of hydrogenated amorphous silicon with a few Angströms per second deposition rate. These depositions are generally carried out on glass substrates or glass covered with a transparent and conducting layer (TCO).

Interestingly, with the growth of a-Si:H by PECVD dopants can be mixed with silane in a controlled way to achieve the desired doping level. The most common dopants have been used are phosphine and diborane; phosphine PH₃ for a layer of N type and diborane B₂H₆ for a layer of P type. The electric quality of the layers deposited depends in general on the excitation frequency mode, the pressure and the flow of the gases, the level of vacuum, the nature and the temperature of the substrate. [4]

PECVD decomposition of silane is schematically presented on figure 2.2.

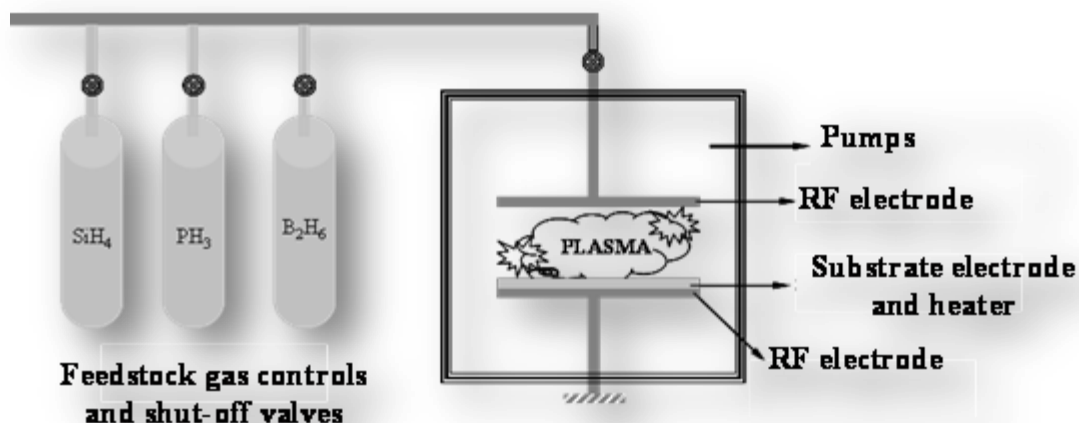


Figure 2.2: System of deposition of hydrogenated amorphous silicon layers

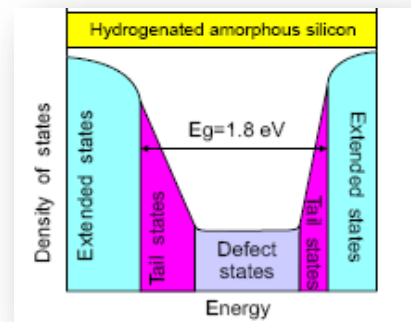
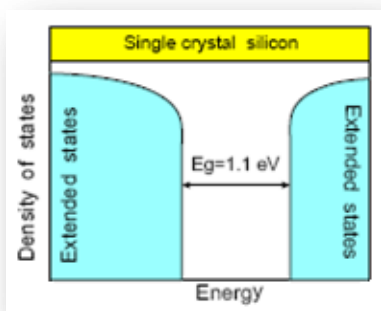
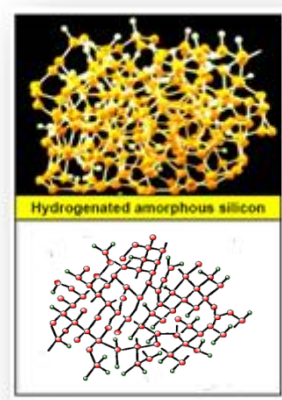
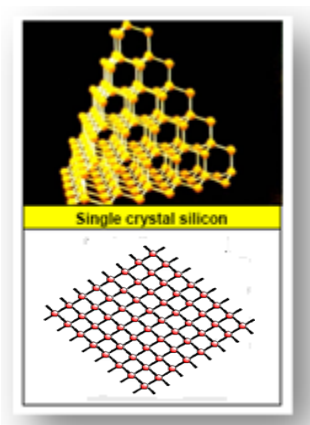
B. Atomic structure

Amorphous silicon (a-Si), unlike crystal silicon (c-Si), does not have a regular atomic organization at long distance. In fact, a short range order persists i.e. the tetrahedral configuration characteristic of the hybridization sp^3 where each atom is related to its four neighbours by covalent bonds Si-Si is satisfied.

The distribution of the atoms of crystal silicon is periodic and regular in terms of coordination, length and angles of the interatomic bonds (fig. 2.3.a). On the other hand, the amorphous silicon shows a light variation on the level of the distance and angle of the bonds. The magnitude of this disorder grows as one move away from the atom of reference. The positions are distributed and a significant fraction of covalence bonds are broken, they represent the dangling bonds. These latter form and act as recombination centres for the free carriers and then determine the behaviour of material.

The amorphous silicon contains so much defects what makes it very difficult to be doped so unusable for the optoelectronics applications. In a large majority of the cases the methods of saturation of the dangling bonds by incorporating from 5 to 15% of hydrogen atoms in the network during the deposition is favored in order to remove the large density of defect states in the band gap and eliminate most of the trapping and recombination centers. In fact, by its small size, it is possible to reduce the no satisfied bonds what improves considerably the properties of the materials (fig. 2.3.b). Thus, the possibility of doping of the a-Si:H was demonstrated by W.E.Spear [5].

Infra-red absorption shows that with slight hydrogen concentration (lower than 10%), the radicals present are SiH and SiH₂ while with high hydrogen concentration the radicals present are (SiH₂)_n [6]. Let us note that the addition of hydrogen not only passivates dangling bonds but preserves also the short-range order and increases the band gap width by the fact that the binding energy Si-H (3.4eV) is higher than the weak bonds Si-Si (2.2eV) [7].



(a) *c-Si*

(b) *a-Si:H*

Figure 2.3: Atomic and energy structure of:
 (a) Crystalline silicon; (b) Hydrogenated amorphous silicon.

C. Chemical bonding and network coordination

In spite of the structural disorder in a-Si:H, a general resemblance of the overall electronic structure between amorphous and crystalline silicon exist. This is caused by the similarity of the short-range atomic configuration and bonding structure in the two types of material. Silicon has four valence electrons with ground state configuration corresponding to $3s^2 3p^2$.

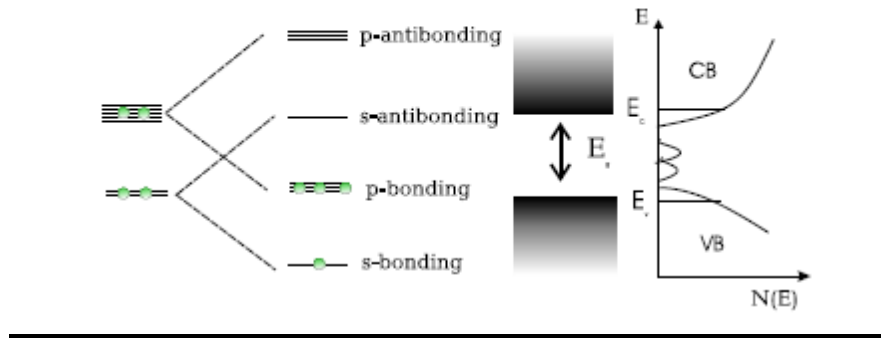


Figure 2.4: Schematic diagram of the electron levels in a-Si, showing the origin of valence and conduction band states. The s and p states of the atom hybridize to form bonding and antibonding orbital which then evolve into the conduction and valence bands.

Each atom in the network is tetrahedrally coordinated, sharing eight valence electrons (two electrons per bond) with all four nearest neighbors. The tetrahedral coordination in silicon is a natural outcome of the chemical bonding requirement and is energetically favorable because bonds are easily created when the bonding states have lower energy than the isolated atomic levels. The bond strength is a function of the overlap of the wave functions (atomic orbital) of the two electrons on neighboring atoms. In a silicon network, this overlap is enhanced by promotion of the paired electrons in an orbital to an orbital of higher energy. When atoms approach each other to form a silicon network, an electron on the s-level is excited to the p-level. This arrangement of orbital is called hybridization and the four orbital formed are called sp^3 hybrids (see Figure 2.2). While atomic orbital correspond to the ground state of an atom, hybridized orbital do not. Their energy is higher by orders of 5-10 eV compared to atomic orbital [2]. However, when electron bonds are formed between atoms with sp^3 orbital this energy is recovered. The interaction between the atoms contributes substantial amounts of energy to the network; hence the resulting bonding level is lower in energy than the ground

atomic state. The increase in energy caused by the formation of these bonds is conventionally known as cohesion energy. The atomic interaction within the structural network causes the orbital to broaden into bands separated by the band gap of the material as shown in Figure 2.2. It is meaningful to note that this explanation is not dependent on symmetry considerations and therefore also applies to amorphous solids. While the anti-bonding states are empty, the bonding states (valency) have the lowest energy and are usually occupied. Interposed on Figure 2.2 is an illustration of the density of states as a function of energy for such a band diagram. We note the existence of states at energy levels lying in the middle of the gap. These states are the non-bonding states attributed to structural defects such as dangling bonds in amorphous silicon. Obviously, the origin of the similarities in the overall electronic structure of a-Si:H and c-Si reflect the chemistry of the silicon atom. It follows that the same chemical interactions that control the structure of crystalline silicon are present in amorphous silicon. However, a complete description of the roles of local chemistry in amorphous and crystalline silicon requires specification of the network topology that defines the way in which atomic sites are interconnected with each other. For covalent systems such as silicon, chemical ordering is predicted by the so called “8-N rule” formulated by Mott [5], where N designates the number of valence electrons. This means that, if for example elements X and Y are in columns a and b of the periodic table, the coordination of X and Y atoms has an optimal number of coordinations given by $z_a = 8 - a$ and $z_b = 8 - b$. The 8-N rule is only applicable to elements belonging to columns IV-VII of the periodic table. The rule suggests that each atom adopts a coordination which results in fully occupied bonding states and empty non-bonding states [6]. With this analysis, it is easy to speculate about the origins of the electronically induced structural reactions that are prevalent in amorphous silicon since any non-optimal value of the coordination number z will result in a high energy configuration. For covalent solids, it is found that the atom can form a defect center when z deviates from the 8-N rule [7]. In crystalline silicon, the equilibrium position of each atom is when its coordination number, its bond lengths and its bond angles are optimized to achieve the lowest energy state. Amorphous silicon is not the lowest energy structure of the silicon network; it has deviations from the optimal atomic coordination which result into coordination defects (dangling bonds) and deviations from optimal bond lengths or bond angles which result into strained bonds. Both dangling bonds and strained bonds can yield localized states in the gap of a-Si as described in the following sections of this chapter.

2.2.2 Electronic structure

The general discussion of the above sections provide a very useful step in understanding the electronic structure of a-Si:H. In the following section, we shall discuss the connection between the atomic structure and the electronic properties of this material. It was shown that the local bonding structure of the material is in a large part responsible for establishing the significant features of amorphous to that of crystalline silicon. Thus the observed similarities in the electronic structure of the two materials reside in a realization that many attractive properties of amorphous silicon are controlled by the bonding chemistry as they are in crystalline silicon. Nevertheless, the disorder which characterizes the structure of the amorphous semiconductors such as irregular interatomic distances and angles and unsaturated bonds by hydrogen, leads to an electronic energy structure different from that of the crystalline semiconductors where the Bloch theorem is pertinent [8]. Consequently, the band diagram is represented by an electronic distribution of states located in the forbidden band and an asymmetry of the conduction and valence bands. One uses then the band gap mobility term instead of forbidden band and edges of mobility instead of edges of bands.

a) Extended states

The energies of the electronic states are perturbed and the band broadens as a consequence of the disorder represented by fluctuations in atomic configuration which causes in turn fluctuations in the potential acting on an electron. In these circumstances, the sharp features prevalent in crystalline density of states become smeared and form band tails which extend into the forbidden gap. It is for this reason that, the sharply defined band edges of the valence and conduction bands are non-existent in amorphous silicon.

b) Tail states or weak bonds

Calculations based on the tight-binding approach [8] have shown that the energies of anti-bonding orbitals (s-like) and bonding orbitals (p-like) are differently affected by material disorder. For example, the energies of the p states are more sensitive to the bonding disorder than are the energies of the s-like states [8]. Consequently the shapes of the band tails in amorphous silicon are not symmetrical, with fewer states in the conduction band tail than in valence band tail. The existence of the tail states was predicted by the theory of Anderson [9], and their presences in the gap of a-Si: H was established in experiments by various techniques

such as the technique of photoemission or PES [5] and the technique of the time of flight or TOF [10]. The valence band tail or VBT and conduction band tail or CBT are the direct result of the weak bonds (irregular interatomic distances and abnormal angles of bonds). They are localized states near to edges of mobility of which their density decrease exponentially according to the following formula: [11]

$$D(E) = N_{v,c} \exp\left(\frac{\pm(E - E_{v,c})}{K_B T_{v,c}}\right) \quad (2.1)$$

Where N_v et N_c are density of states at E_v et E_c edges respectively;

T_v et T_c denote characteristic temperature for VBT and CBT respectively.

The states of VBT, known also under the name of Urbach tail (Urbach 1953) and determined by the optical techniques [5], have typically a slope $K_B T_v$ about 45-55meV. It is broader opposite the slope $K_B T_c$ of the states CBT which is typically about 20-30meV because the states of VBT are more influenced by the disorder compared to the states of CBT. As a result of the asymmetry in the distribution of localized states, the position of the Fermi level is affected. As an example, in an undoped sample of amorphous silicon, the Fermi level in the dark is generally shifted closer to the bottom of the conduction band. Hence, these states determine several electrical properties of the material by controlling the process of multi-trapping by their acceptors-like character close to the valence band or VB (they are neutral when they are empty) and donors-like character close to the conduction band or CB (they are neutral when they are filled).

c) Dangling bonds or deep defects

In addition to the states close to the band edges mobility, the amorphous silicon contains also deep localized states close to the center of the gap mobility in spite of the addition of hydrogen during the deposition of a-Si: H. These states come from the unsaturated defects by hydrogen, where certain bonds are still broken. They present an amphoteric character i.e. they can be neutral D^0 (has an electron), charged positively D^+ (does not have any electron) or negatively D^- (has two electrons) (figure 2.5).

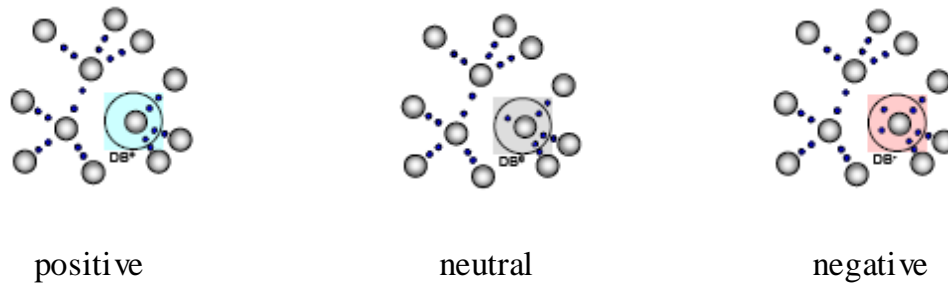


Figure 2.5: Dangling bonds charge states

A positive energy gap called energy of correlation U [12] exists and separates the maxima of the distributions, presumed Gaussian [13], of the dangling bonds D^0/ D^+ and D^- . It varies between 0.2 and 0.5eV and it given by: [5, 14]

$$U = \frac{q^2}{4\pi\epsilon_0\epsilon r} - W \quad (2.2)$$

where q is electron charge and r is effective distance between two electrons.

The first term of the equation (2.2) corresponds to the energy of Coulomb repulsion between two electrons and the second term represents the energy of relaxation.

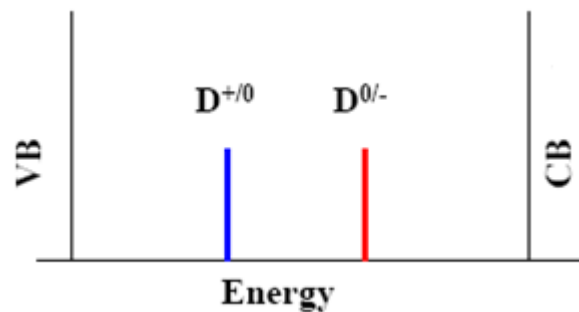


Figure 2.6: Transition energy levels D^{+0} and D^{0-}

Several experiments such as electron spin resonance or ESR [5], the photothermal deflection spectroscopy or PDS [2] and the space charge limited current or SCLC [10, 11] showed that energy U is positive. In other words, within thermodynamic equilibrium the majority of the defects are neutral. Nevertheless, some authors lead to negative correlation energy [12].

To measure the energy distribution of the deep defects one has resort to various techniques which can be classified in two categories; the first category those which consider and exploit

the thermal transitions like deep level transient spectroscopy or DLTS [11] and the second category are those which consider and exploit the optical transitions such as PDS. Differences were found concerning the nature, the distribution and the density of states of D^0 , D^+ and D^- . The most used are the standard model and the defect pool model [15, 16]. The latter model is adopted in our study.

d) Density of states

The DOS defines the number of allowed electronic states per unit volume per unit energy. The interpretation of the electronic structure of a-Si:H is summarized in the band model of this material as shown in Figure 2.7. This figure qualitatively illustrates the density of states or DOS as function energy in logarithmic scale.

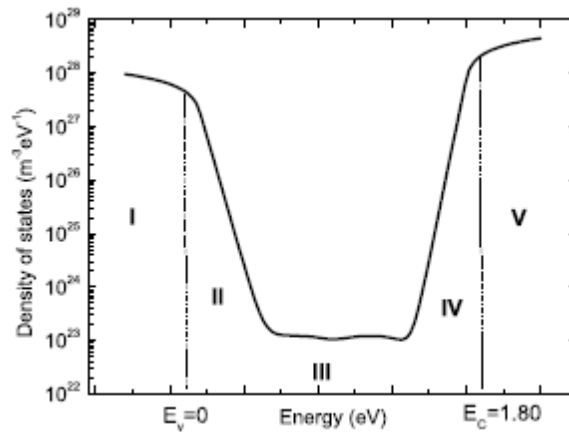


Figure 2.7: Schematic diagram for the density of states in amorphous silicon.

Regions I and V: Extended states, regions II and IV: Tail states and

Region III: Midgap states

One can differentiate three different regions: Region I and V corresponds to extended states. In this region the carriers have a finite mobility, in short they are free carriers and their wave functions are non-localized. Region II and IV corresponds to the band tails whose states are localized and a carrier occupying them has small chance of moving away as its mobility is reduced strongly. Region III corresponds to midgap states originating from structural and coordination defects (dangling bond states) in amorphous silicon. The dangling bond states play a major role in the electrical transport of amorphous silicon by controlling trapping and recombination processes. The localized and delocalized states are demarcated by mobility

edges E_C and E_V as proposed by Mott and Davis (1979). The mobility gap E_{mob} is defined as the region between these two energies. The hypothesis advanced by Mott [9], asserts that at zero absolute temperature ($T=0$), the extended states offer finite mobility of the carriers and zero mobility for localized states. This statement suggests an abrupt transition of mobility at the band edge energies E_C and E_V . However, the gradually decreasing densities of states from extended to localized states suggest that localization of the electron wave function varies smoothly as we move from extended states to states deep in the band gap. Obviously, the shallowest states will generally have less localized electronic wave functions than the deepest states near the center of the gap. This examination entails a smoothly increasing mobility from localized to extended states. Unfortunately, the exact behavior of the properties of states near the mobility edges is still not well known. There is no available quantitative technique for characterizing these states [10].

2.2.3 Effects of doping

As soon as Spear and LeComber deferred in 1975 that a-Si: H can be doped by adding small quantities of atoms of phosphorus or boron, the explanation and the exploitation of the effect of doping on the properties of this material took a great importance.

As in crystalline silicon, if one introduces doping elements like boron or phosphorous in amorphous structure, one hopes to achieve p-type or n-type doping. It appears that the doping efficiency, which is defined as the fraction of introduced dopant atoms which indeed are electrically active, is tremendously low in amorphous silicon. The reason that effective doping in defect-rich material is not possible stems from the 8-N rule. The network topology of amorphous silicon is such that various values of the coordination number z occur. In crystalline silicon the value z can only be 4, but in amorphous silicon network values of 3 and 5 are also quite possible. Mott's rule states that normally a foreign element will prefer a site in the network at which the coordination is such that a number of valence electrons n , together with the number z of electrons from possible covalent bonds at this site, should add up to a full shell, i.e 8, in order to minimize the energy at this position. In other words one can conclude from this rule that elements like boron or phosphorus which are added to an unhydrogenated amorphous silicon network will in general not show doping effects, since they choose e.g a 3-fold coordination, in which no donor or acceptor states can be formed. This interpretation of course generally applies only when the atoms indeed have possibilities

to choose, i.e. when they are mobile and also not yet fully built in. This is a situation which occurs during deposition and growth of doped layer and can occur afterwards only at elevated temperatures. The presence of hydrogen however serves to stabilize the network and, more specifically, to greatly reduce the number of unpaired electrons or dangling bonds. In such a network many dopant atoms therefore are forced in four-fold coordinated sites, in which they will produce a doping effect in terms of donor or acceptor states. It may be understood that the doping efficiency will be low, as compared to crystalline silicon. In the crystalline silicon the efficiency of doping is of the order of unity, while in hydrogenated amorphous silicon it can range from 10^{-4} to 10^{-2} , depending on the deposition temperature. The details of the doping process in amorphous silicon are more complicated than what has been described above. It appears that there exists an intimate relation between the number of electrically active dopants and the number of defects in the material. The doped materials are richer with defects than undoped hydrogenated amorphous silicon.

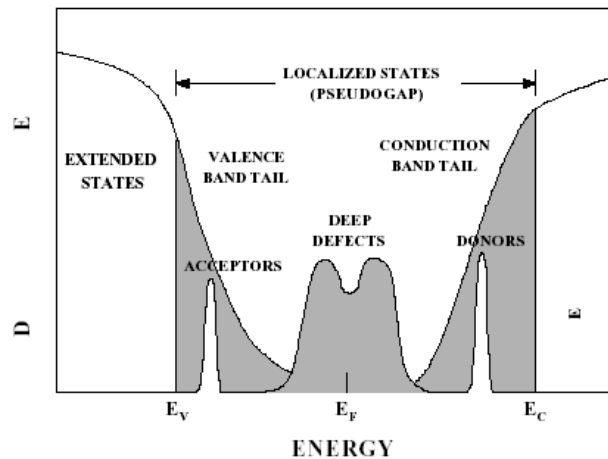


Figure 2.8: Doping effect on the Density of states of *a-Si: H*

As a final point, the diverse doping effects can be resumed in the following points:

- Conductivity changes a factor of 10^8 with doping by the displacement of the Fermi level towards the edges mobility. Indeed, the activation energy E_{σ} passes from 0.7 to 0.8eV for the undoped case and to 0.15eV for N type doped and to 0.3eV for P type doped [5, 11]. In other words, conductivity type P is lower than conductivity type N because the VBT is broader than the CBT.

- The doping introduced into the crystalline semiconductors donors or acceptors electronic levels close to the conduction or the valence band. Regarding to the amorphous semiconductors, in addition to these shallow states (see fig. 2.8), doping increases the density of the defects N_D following the empirical relation: [2,5]

$$N_D = 3.10^{19} \sqrt{c_R} \quad \text{cm}^{-3} \quad (2.3)$$

with c_R is the doping density factor.

- Doping reduces also the gap width and increases the slope of the CBT and VBT what involves the reduction in the mobility of electrons and the holes [17].

2.2.4. Metastability and Staebler-Wronski effect

The phenomenon of metastability is caused either by a rise in the temperature to a value higher than the equilibrium temperature T_f (higher than approximately 220°C), or by a strong and prolonged illumination (approximately 100 mWcm⁻²). This last effect is known by the Staebler-Wronski effect, it was discovered by Staebler and Wronski at laboratory RCA since 1977. This harmful effect on the electronic properties of material is characterized not only by the slow reduction in photoconductivity σ_{ph} under strong illumination but also by the reduction in the dark conductivity σ_d . (Fig. 2.9)

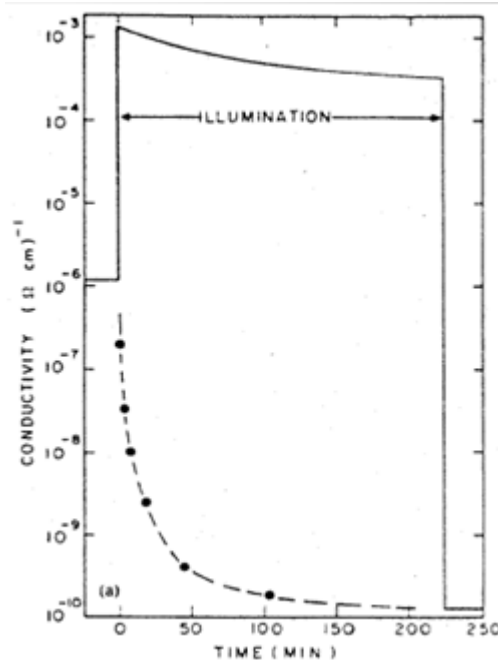


Figure 2.9: Dark conductivity (broken line) and photoconductivity (continuous line) according to the duration to the light

The initial properties of material can be recovered by an annealing of a few hours at a temperature of 150°C (423K), it is a phenomenon known as reversible.

In spite of the intense attempts for the comprehension of this effect in a-Si:H, it still needs more explanations. One can recapitulate the critical points related to this effect in the following way:

- The dominant metastable defects are the dangling bonds. Their densities pass from 10^{16}cm^{-3} in an initial state to 10^{17}cm^{-3} in a degraded state of the material [7];
- Photoconductivity can decrease by a factor of 10 [18];
- The effect only appears in intrinsic films, while in strongly doped films the effect does not appear [19];
- The majority of the theories include S-W effect in volume. Though, the probability of the creation of the metastable defects on the surface remains possible [6];
- Several microscopic models were proposed to explain the mechanism of creation of defects under the strong and prolonged illumination; one of them is based on the break of the weakest bonds silicon-silicon (Si-Si) where hydrogen plays a significant role [20,21];
- The shift of the Fermi level toward the middle of the gap of mobility under the illumination involves the reduction in σ_d . This is due to the increasing of DB density;
- The rose factor γ which connects the photoconductivity to the intensity of the optical excitation ($\sigma_{ph} \propto G^\gamma$), pass from 0.5 before to 0.9 after the illumination [7];
- Fortunately, the S-W effect is reversible and there is a saturation point of the degradation which depends on the conditions of deposition [4, 18].

2.2.5. Optical properties of the a-Si:H

a) Optical gap

We have earlier mentioned that the structure of a-Si:H can be described as a continuous random network, but in a real a-Si:H network the short range order may differ from one site to another. The slight distortions in the atomic configuration results into random distribution of charged centers leading to a non-periodic potential. A disordered potential can lead to strong electronic scattering and a short coherence length of the electron wave function. In amorphous silicon the coherence length is approximately of the order of the lattice spacing and the

resulting uncertainty in the wave vector is of the same amount as the wave vector itself. Under these conditions the momentum is no longer a good quantum number and is not conserved in optical transitions. Thus all optical transitions in amorphous silicon can be considered as direct. The probability of optical transitions in direct band gap material is greater than that of an indirect band gap, for this reason the absorption coefficient of a-Si:H is higher compared to crystalline silicon. The absorption coefficient can be calculated from the optical band gap E_{opt} . In fact, the optical gap E_{opt} of the a-Si:H is linked to the absorption coefficient α and the frequency of the incidental wave ν by using Tauc's rule [4,5]:

$$\sqrt{\alpha h \nu} = B (h \nu - E_{opt}) \quad (2.4)$$

where h indicates the constant of Plank and B is a constant of proportionality.

The $(\alpha h \nu)^{1/2}$ behavior is predicted for an amorphous semiconductor if the band edges are parabolic and the matrix elements for optical transitions are independent of energy [11]. Thus, one can by a simple linear extrapolation of $\sqrt{\alpha h \nu} = f(h \nu)$ graph, determine the value of the optical gap (Fig. 2.10).

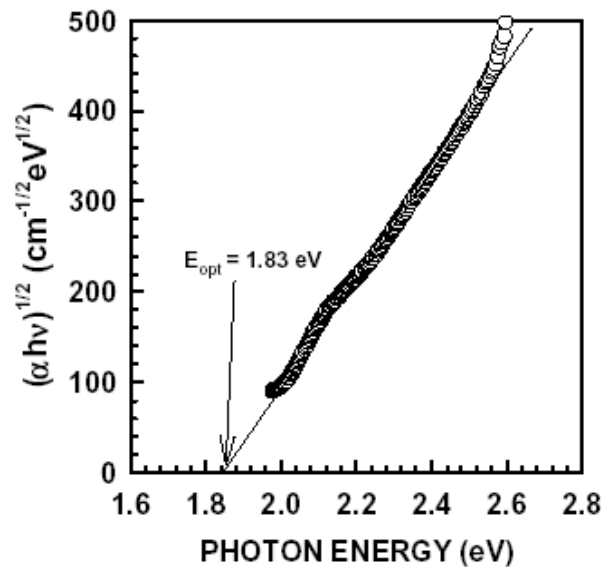


Figure 2.10: Method of determination of the optical gap of the a-Si:H

However the quadratic energy dependence of the optical band gap is not universally observed. The distribution near the band gap edges can be linear and a cubic energy dependence $(\alpha h \nu)^{1/3}$ has been predicted for the optical band gap [12]. The optical gap does not define the band gap of amorphous silicon; instead the mobility gap is generally used to define the band gap of amorphous silicon material. The optical gap is slightly smaller than the mobility gap.

Since the energy of the mobility edge depends strongly on the extent of material disorder, the band gap of amorphous silicon can be varied according to the degree of disorder. The optical gap depends, independently of the method of deposition of film, the hydrogen concentration and doping [4]. The optical gap can be used to estimate the energy of photons that can be absorbed by a-Si:H. By decreasing the optical gap, one can increase the part of the solar spectrum that is absorbed by a-Si:H.

b) Optical absorption

The optical absorption properties of amorphous silicon are very important for understanding the operation of a solar cell and for optimizing its conversion efficiency. Thus the weight of understanding the absorption processes in a-Si:H stems from their use as a probe for the local structure of a-Si:H network. From absorption measurements, one can deduce information on both the tail and defect states.

Figure 2.11 indicates the shape of the curve of optical absorption $\alpha(h\nu)$ according to energy $h\nu$. Three principal areas are distinguished; the first represents absorption for energies higher than the energy of the optical gap thus translating the direct optical transitions between valence and conduction band, while with the second area i.e. for the photons of moderate energy and lower than the energy of the optical gap, absorption decrease quickly according to an exponential law:

$$\alpha(h\nu) = \alpha_o \exp\left(\frac{h\nu}{E_o}\right) \quad (2.5)$$

This decrease whose slope is in direct relation with the Urbach tail, is generally associated the optical transitions starting from the localized states of the VBT towards the extended states of the VB.

Regarding the last region, for low energies the decrease of absorption with energy is slower compared to the preceding area. In this area absorption is due to the optical transitions starting from the deep localized states towards the extended bands. According to Mott and Davis [22], there is a convolution between the energy distribution of the dangling bonds and the optical absorption coefficient in this interval of energy.

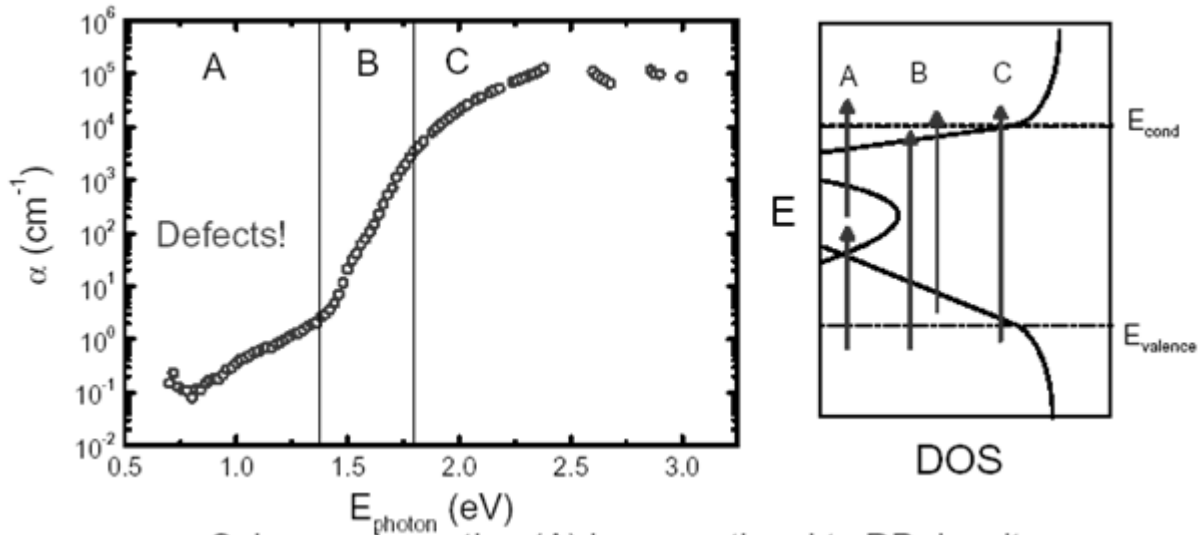


Figure 2.11: Optical absorption spectrum of the *a*-Si:H and corresponding optical transitions

Let us note that the dependent hydrogen concentration and the nature of the bonds can be extracted by measuring $\alpha(h\nu)$ [23, 24]. One sees immediately that accurate measurement of absorption spectrum for various temperatures and illuminations, allows us to know various properties of material studied in an initial or degraded state for instance the mechanisms of transport and nature, creation and dynamics of the deep defects [25] (Fig.2.12 and Fig.2.13).

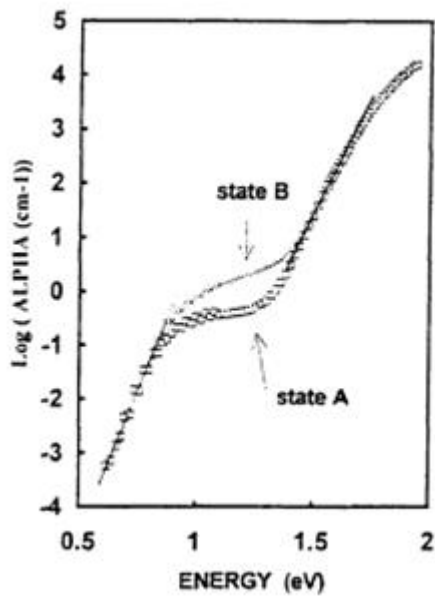


Figure 2.12: Optical absorption spectrum of the *a*-Si:H measured by CPM before (state A) and after (state B) illumination

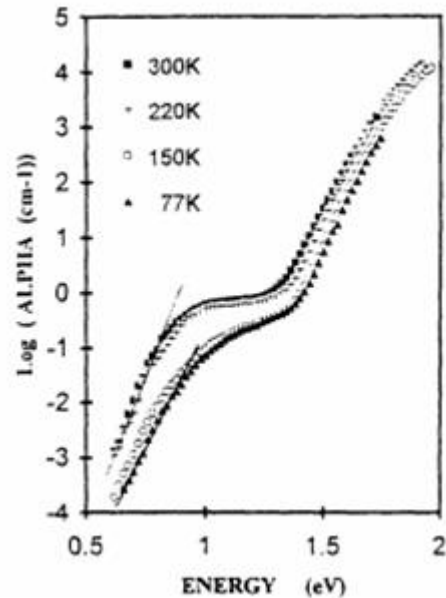


Figure 2.13: Optical absorption spectrum of the *a*-Si:H measured by CPM for a range of temperatures

2.2.6. Mechanisms of transport

In absence of the illumination the mechanism of transport in the amorphous semiconductors depends on the temperature and thus presents three regions [9, 26, 27]: (Fig.2.14)

- For low temperatures (lower than 100K for a-Si:H) conduction is dominated by the displacement of the carriers by jump between the localized states (hopping transport).
- For high temperatures (higher than 420K for a-Si:H), the atomic configuration and thereafter the distribution energy of electronic states DOS are not stable and they change with the temperature;
- For intermediate temperatures, the mechanism of transport is controlled by the process of multi-trapping where the charge carriers coming from the localized states are thermally activated in the extended states.

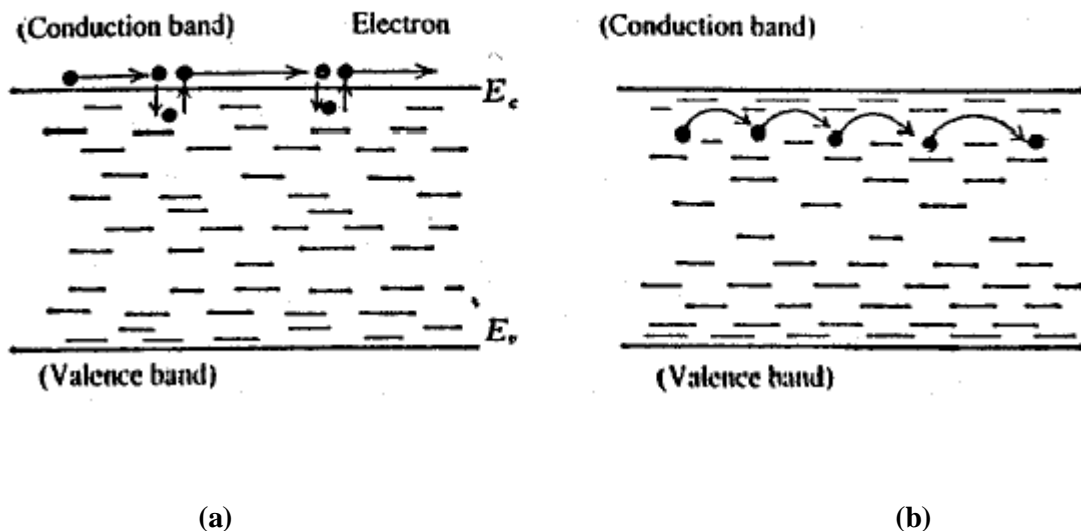


Figure 2.14: Mechanism of transport: (a) multi-trapping; (b) hopping

Following to the electronic structure of a-Si: H, two types of capture and emission can exist; capture and emission by the tail states and by the deep states. The coefficients of capture and emission of each localized state determine if this state behaves like a trap or a center of recombination. For differentiated, one uses what is called energy of demarcation E_d . The latter is defined as being a state satisfying the equality between the probability of emission and recombination of the trapped charge carrier. Thus, the trapped electrons, for example, by the states being with the lower part of E_d have the tendency to recombine while the electrons

trapped in the states being located at the top of E_d have the tendency to be emitted towards the conduction band.

2.2.7. Phenomena of recombination

The recombination is defined as being the net difference between the capture and the release rate of the free carriers by the states of the band gap mobility. The recombination of the excess charge carriers created by an optical excitation occurs in order to establish thermodynamic equilibrium. The process of recombination is composed of two stages. Firstly, the electron carries out multiple transitions (multi-trapping and thermalisation) then, it releases its energy while recombining with a hole. This release can be radiative by emission of photons or not radiative by emission of phonons. The radiative recombination between the localized states is observed for low temperatures and the non-radiative recombination between the extended states and the deep states is met for temperatures higher than 100 K [28, 29] (Fig.2.15).

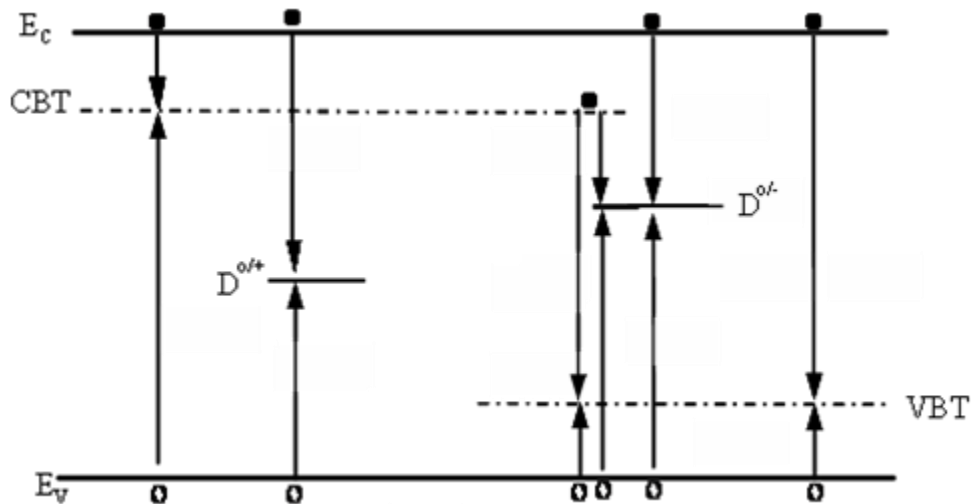


Figure 2.15: Mechanisms of recombination o: hole •: Electron

In addition, there are other types which must be taken into account in the amorphous semiconductors. Among them, there is the direct electron-hole recombination which occurs in the case of the strong light intensities where the free carrier's density remains less than the charges density trapped in the tail and the defects states. Moreover, there is the recombination on the surface and interface which is more probable for low thicknesses like the case of the solar cells.

The recombination centres are mainly the dangling bonds for the *a*-Si:H, because these bonds are close to the medium of the gap where the probability that a charge carrier recombined is higher than the probability of being emitted.

2.3. Fundamental properties of hydrogenated micro crystalline silicon μc -Si:H

2.3.1. Deposition methods of hydrogenated micro crystalline silicon

Usually, to obtain microcrystalline deposition, additional hydrogen source gas is added during the deposition. Fortunately, a diversity of methods is used for the deposition of μc -Si:H. Microcrystalline silicon grown by PECVD, is a promising material for the application as an intrinsic absorber layer in solar cells: Best efficiencies have been obtained using this technique. For the deposition of high-quality material at high deposition rates, conditions of source gas depletion at high pressure (HPD: high-pressure depletion), PECVD regimes featuring higher RF frequencies (VHF: very high frequency), and altered electrode designs are explored. Alternative techniques exist to deposit μc -Si:H at high growth rate such as hot-wire chemical vapor deposition (HWCVD), micro-wave plasma-enhanced chemical vapor deposition (MW-PECVD) and expanding thermal plasma (EPT).

2.3.2. Atomic structure

Microcrystalline silicon is a mixed phase material consisting of *c*-Si, *a*-Si:H, nano-crystallites, and grain boundaries. During the layer growth, crystallite formation starts with nucleation after an amorphous incubation phase. In the continuing layer deposition, clusters of crystallites grow (crystallization phase) till a saturated crystalline fraction is reached.

These processes are greatly dependent on the deposition condition. Generally, it can be stated that these processes are enhanced by the presence of atomic hydrogen due to the chemical interaction with the growing surface [30, 31]. Figure 2.16 show a schematic representation of the incubation and crystallization phase as a function of the source gas dilution with hydrogen. The incubation phase and crystallization phase are of immense significance for the optoelectronic material properties.

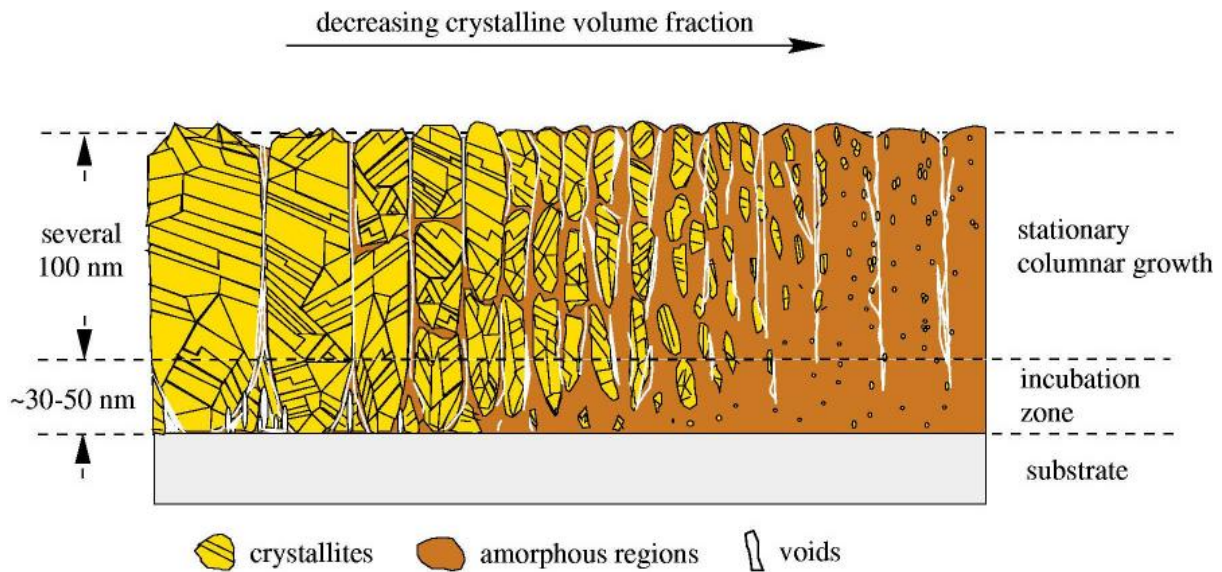


Figure 2.16: Schematic representation of structure features found in μc -Si:H. From left to right the film composition changes from highly crystalline to amorphous according to reference [31]

2.3.3. Electrical and optical properties

In general, the photoconductivity of a semiconductor is dependent on the balance between the generation and recombination of charge carriers as well as their mobility. In the mixed phase material μc -Si:H, the transport mechanism is not well understood yet. Whether the electrical properties are determined by the amorphous or the crystalline fraction is dependent on the transport path. If the crystalline fraction is sufficiently high, percolation takes place along interconnected paths through the crystallites. Hence, the grain boundary properties play an important role.

The optical absorption in μc -Si:H is due to absorptions from both the amorphous and crystalline fraction. Compared to a -Si:H, the absorption of high energy photons ($h\nu \geq 1.7$ eV) is lower due to the indirect band gap of the c -Si fraction, while in the low energy part the μc -Si:H absorption is relatively higher due to the smaller band gap (although indirect). Photons with energy exceeding the optical band gap, are absorbed in the film. The optical absorption spectrum of μc -Si:H compared to a -Si:H and c -Si is plotted in Figure 2.17.

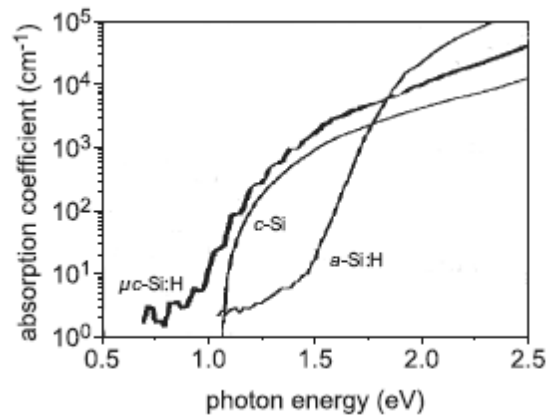


Figure 2.17: The absorption coefficient α of $c\text{-Si}$, $a\text{-Si:H}$, and $\mu c\text{-Si:H}$ according to reference [6].

2.3.4 Advantages of $\mu c\text{-Si:H}$

Microcrystalline silicon intrinsic layers are advantageous for i -layer use in thin-film silicon solar cells because the lower apparent band gap compared to amorphous silicon makes that combination of $\mu c\text{-Si:H}$ and $a\text{-Si:H}$ in a tandem solar cell better matched to the solar spectrum than either $a\text{-Si:H}$ or $\mu c\text{-Si:H}$ alone (see Figure 2.18). Theoretical calculations show that the combination of band gaps of $a\text{-Si:H}$ and $\mu c\text{-Si:H}$ is close to the best possible combination for maximum efficiency. Microcrystalline silicon with a sufficiently high crystalline volume fraction does not show light-induced degradation of optoelectronic properties [31, 32], but $a\text{-Si:H}$ shows an increasing defect density upon light soaking (Staebler-Wronski effect). The material costs of thin film microcrystalline silicon are far low compared to the $c\text{-Si}$ wafer because, when deposited on a substrate, the required thickness is two orders of magnitude thinner. Light trapping techniques can be used to enhance the absorption in the thin layer. The production costs are also lower compared to $c\text{-Si}$ because thin-film silicon is deposited with a low temperature process and a high deposition rate.

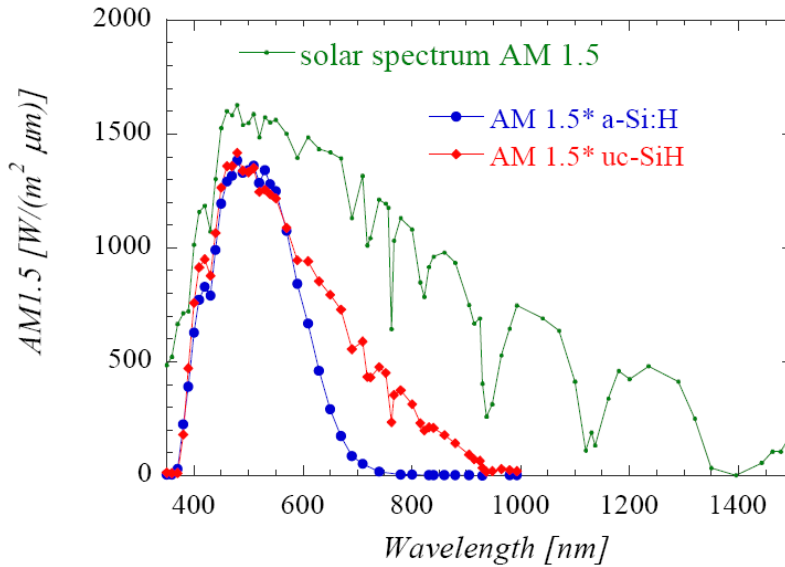


Figure 2.18: AM 1.5 solar spectrum and spectral curves of the light absorbed by μc -Si:H and a -Si:H solar cells calibrated on AM 1.5 according to reference [32]

Microcrystalline silicon doped layers are suitable as window layer because it has a low optical absorption above $h\nu = 2$ eV compared to a -Si:H. In this energy range, the loss of photons in window layers can be significant. The electrical properties of μc -Si:H doped layers are encouraging compared to a -Si:H, because it can be more efficiently doped. The activation energies of dark conductivity are smaller compared to a -Si:H, because the Fermi level is closer to the conduction and valence band for n - and p -type doped layers respectively. Therefore, the built-in voltage of the solar cell is higher when μc -Si:H doped layers are used.

References

- [1] Peter Munster, "Silicium intrinsèque et dopé in situ déposé amorphe par SAPCVD puis cristallisé en phase solide", Thèse d'état, Université de Rennes 1, France, 17 Juillet 2001.
- [2] T. Searle, "Properties of Amorphous Silicon and its Alloys", Edited by University of Sheffield, UK, 1998.
- [3] G. Turbin, "Dissociation et transport dans un plasma de silane durant la croissance de couches minces de silicium amorphe hydrogéné", Thèse d'état, Université de Nantes, France, 1981.
- [4] Alain Ricaud, "Photopiles solaires, de la physique de la conversion photovoltaïque aux filières matériaux et procédés", Presses polytechniques et universitaires romandes, 1997.
- [5] R. A. Street, "Hydrogenated amorphous silicon", Cambridge university press, 1991.
- [6] Zdenek Remes, Ph.D. thesis, "Study of defects and microstructure of amorphous and microcrystalline silicon thin films and polycrystalline diamond using optical methods", faculty of mathematics and physics, Charles university, Prague, Czech Republic, 1999.
- [7] K. Takahashi & M. Konagai, "Amorphous silicon solar cells", North Oxford academic publishers Ltd., 1986.
- [8] C. Kittel, "Physique de l'état solide", Edition Dunod, Paris, France, 1998.
- [9] M. F. Thorpe and L. Tichy, "Properties and Applications of Amorphous Materials", Proceedings of NATO Advanced Study Institute, Czech Republic, 25 June-7 July 2000.
- [10] G. Seynhaeve, "Time-Of-Flight Photocurrents in Hydrogenated Amorphous Silicon", Ph.D.thesis, Leuven, 1989.
- [11] A. Treatise, "Semiconductors and Semimetals", Volume 21, Part C, Academic Press Inc., Orlando, Florida, USA, 1984.
- [12] N.Orita, T. Matsumura, H. Katayama-Yoshida, Journal of Non-Crystalline Solids 198-200 (1996) 347-350.
- [13] C.-Y. Lu, N. C.-C. Lu, C.-S. Wang, Solid-State Electronics 27 (1984), No. 5, p. 463-466.
- [14] J.H. Zollondz, "Electronic Characterisation and Computer Modelling of Thin Film Materials and Devices for Optoelectronic Applications", Ph.D.thesis, University of Abertay, Dundee, UK, 2001.
- [15] H.Dücker, O. Hein, S. Knief, W. von Niessen, Th. Koslowski, Journal of Electron Spectroscopy and Related Phenomena 100 (1999) 105-118.
- [16] J. Schmal, Journal of Non-Crystalline Solids 198-200 (1996) 387-390.

- [17] K. Pierz, B. Hilgenberg, H. Mell and G. Weiser, *Journal of Non-Crystalline Solids* 97& 98 (1987) 63-66.
- [18] Christian Hof, “Thin film solar cells of amorphous silicon: influence of i-layer material on cell efficiency”, UFO atelier für Gestaltung & Verlag, Band 279, ISBN 3-930803-78-X, 1999.
- [19] V. Nadazdy, R. Durny, I. Thurzo, E. Pinicik, *Journal of Non-Crystalline Solids* 277- 230 (1998) 316-319.
- [20] M. Stutzmann, W. B. Jackson and C. C. Tsai, *Physical Review B*, Vol. 32, No.1, pp. 23-47, July 1985.
- [21] R. A. Street, *Physica B* 170(1991) 69-81.
- [22] N. F. Mott and E. A. Davis, *Electronic Processes in Non-Crystalline Materials*, Clarendon Press, U.K., 1979.
- [23] M. Yamanaka, I. Sakata and T. Sekigawa, *Jpn. J. Appl. Phys.*, Vol. 39 (2000), pp. 3302-3307, Part 1, No. 6A, June 2000.
- [24] I. Sakata, M. Yamanaka, T. Sekigawa and Y. Hayashi, *Solid State Phenomena*, Vols. 44-46,(1995) pp. 127-134.
- [25] P. Sládek and M. L. Thèye, L. Chahed, *Journal of Non-Crystalline Solids* 164-166 (1993) 363-366.
- [26] A. Merazga, “Steady state and transient photoconductivity in n-type a-Si”, Ph.D.thesis, Dundee Institute of Technology, Dundee, UK, 1990.
- [27] H. Overhof, *Journal of Non-Crystalline Solids* 227-230 (1998) 15-22.
- [28] T. Pisarkiewicz, T. Stapinski, P. Wojcik, 43rd International Scientific Colloquium, Technical University of Ilmenau, September 21-24, 1998.
- [29] F. Vaillant, D. Jousse, and J.-C. Bruyere, *Philosophical Magazine B*, Vol. 57, No.5, 649-661, 1988.
- [30] Vetterl, O. Finger, F. Carius, R. Hapke, P. Houben, L. Kluth, O. Lambertz, A. Muck, A. Rech, and B. Wagner, 2000, *Solar Energy Materials and Solar Cells* 62 97.
- [31] Von Thorsten Dylla, “Electron Spin Resonance and Transient Photocurrent Measurements on Microcrystalline Silicon”, PhD. thesis, Fachbereich Physik, Freie Universität Berlin, Germany, 2004.
- [32] Urs Samuel Graf, “Single-chamber process development of microcrystalline Silicon solar cells and high-rate deposited intrinsic layers”, PhD. thesis, Université de Neuchâtel, October 2005.

CHAPTER 3

CHARACTERISATION TECHNIQUES OF AMORPHOUS SEMICONDUCTORS

3.1. Introduction

The totality of optoelectronic properties of a-Si:H films are related directly to the density of electronic states $D(E)$ in a-Si:H. In order to enhance the performance of a-Si:H based devices such as solar cells, photodetectors and thin-film transistor where undoped a-Si:H layers play the most important role, a low $D(E)$ in undoped a-Si:H is essential. Measurement of the $D(E)$ and understanding of the nature of gap states are, therefore, very imperative. The development of various techniques is so very significant and justified and the problem has received considerable interest to conclude the $D(E)$. These comprise both electrical and optical methods.

Transient capacitance methods like deep-level transient spectroscopy (DLTS) [1,2] and isothermal capacitance transient spectroscopy (ICTS) [1], which usually make use of a Schottky barrier junction, are tested techniques for determining the $D(E)$ below the Fermi level. However, these methods are limited in their application to doped samples of low resistivity. For high resistivity materials, such as undoped or compensated a-Si:H films, the dielectric relaxation times are too long for the measurement of the capacitance which can reflect the depletion width in the junction. SCLC-TOF [3] measurements do give quantitative estimation of the $D(E)$, but only above the Fermi level. However, the determination of the $D(E)$ below the Fermi level for undoped films is important, because gap states located below the Fermi level include singly-occupied Si dangling bonds which are considered to be main

midgap states. Moreover, those midgap states would determine the optoelectronic properties of the film and would, therefore, affect the performance of devices based on these films.

Photothermal deflection spectroscopy or PDS [4, 5], dual beam photoconductivity or DBP [6, 7] and constant photocurrent measurements or CPM [8, 9]; give the variation of the optical absorption coefficient α versus the photon energy $h\nu$ in the material. These techniques are capable of measuring the absorptance down to values of about 10^{-5} . The density of defects and the capture section of the charge carriers are related to the absorption coefficient. Indeed, the optical absorption coefficient is associated with a joint density of the initial and final states. However, it is rather difficult to distinguish one from the other. The main results obtained by PDS and DBP are considered to show information on the valence-band-tail in the case of hydrogenated amorphous silicon-based alloys. In this chapter, details on the experimental techniques for the characterization of the thin-film materials are presented.

3.2. Dark conductivity

The dark conductivity as function of the temperature $\sigma_d(T)$ of hydrogenated amorphous silicon (a-Si:H) is often determined to evaluate the underlying electronic transport properties of thin-film samples. It is activated thermally according to the distance which separates the Fermi level E_F and the conduction band (valence band) for N type semiconductor (P type). It is what is called the activation energy E_a .

The experimental measurement of the dark conductivity is normally performed using either a sandwich or coplanar electrode configuration as illustrated schematically in figure 3.1. Data collected as a function of temperature T are conventionally plotted as $\log(\sigma_d)$ against inverse temperature as shown schematically in figure 3.2 and analyzed according to the Arrhenius expression;

$$\sigma_d(T) = \sigma_o \exp\left(-\frac{E_a}{K_B T}\right) \quad (3.1)$$

where σ_o is the conductivity extrapolated to $1/T=0$ and K_B is Boltzmann's constant. The measured activation energy E_a is normally interpreted as being equal to $E-E_F$ where E is the energy at which majority carrier conduction occurs.

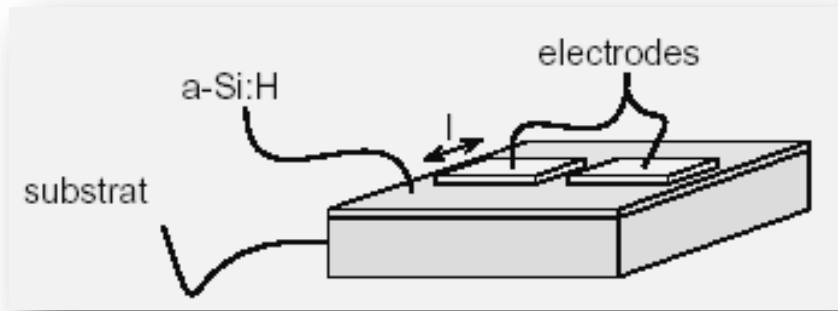


Figure 3.1: Co-planar electrode configuration for thin film a-Si:H conductivity measurement

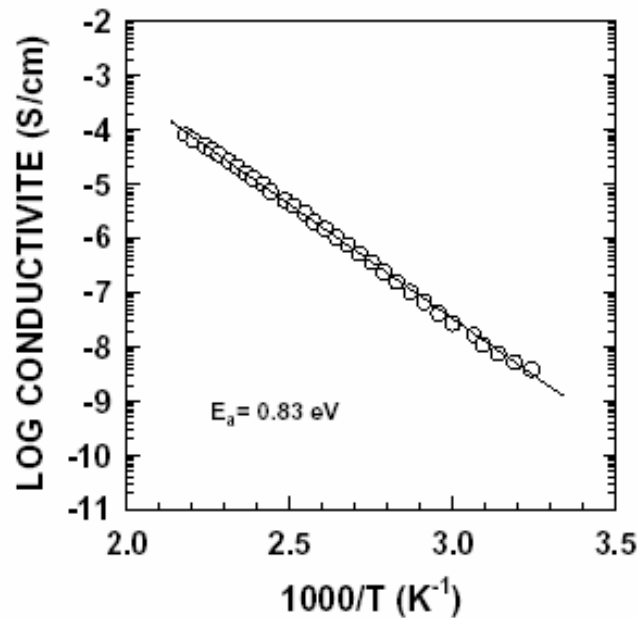


Figure 3.2: Dark conductivity of the a-Si:H in semi-logarithmic scale allowing the measurement of the energy of activation

The conduction model dominating at the low temperatures is conduction by hopping while at the higher temperatures conduction is rather by thermal activation through the extended states, close to the edges of the mobility bands.

Conductivity versus the energy E and the temperature T is given by: [10]

$$\sigma(E, T) = \int q \cdot D(E) \cdot \mu(E) \cdot f(E, T) dE \quad (3.2)$$

where q is the electron charge ;

$D(E)$ denotes the density of states distribution;

$\mu(E)$ indicates the mobility of charge carrier;

$f(E, T)$ designate the occupation function according to Fermi-Dirac statistic.

The integral (3.2) included the contribution of the electrons and holes above and below E_F respectively to the conduction.

So if we considers conduction only in the vicinity of the edges mobility, in other words the mobility of electrons μ_n and the holes μ_p are null within the band gap mobility and constant elsewhere, and if we propose to treat only one type of charge carrier (electron), conductivity is written in the form: [10,11]

$$\sigma_d(T) = \sigma_o \exp\left(-\frac{E_C - E_F}{K_B T}\right) \quad (3.3)$$

with $\sigma_o = \mu_o \cdot q \cdot N_C$

$(E_C - E_F)$ being the activation energy E_a , μ_o being the mobility of free electrons, N_C being the effective density at the level E_C .

The factor σ_o corresponds to conductivity at infinite temperature. It is supposed to be independent of the temperature. However, the quantity $(E_C - E_F)$ depends on the temperature as long as E_C vary with the temperature. To overcome this error of reference displacement, one replaces $(E_C - E_F)$ by $(E_C - E_F) - \gamma T$.

While replacing in the equation (3.3) one obtains:

$$\sigma_d(T) = \sigma_o \exp\left(\frac{\gamma}{K_B}\right) \exp\left(-\frac{E_C - E_F}{K_B T}\right) \quad (3.4)$$

Let us note that this displacement γT can be neglected since measurements of optical absorption [12] gives a value of $2,4 \cdot 10^{-4} \text{ eV} \cdot \text{K}^{-1}$ for the value of the γ .

3.3. Steady state photoconductivity

When, a semiconductor is excited by a continuous monochromatic light, the density of charge carriers changes by thus increasing conductivity. Conductivity under excitation or so-called photoconductivity σ_{ph} is defined by the difference between total conductivity σ_{tot} and dark conductivity σ_d .

$$\sigma_{ph} = \sigma_{tot} - \sigma_d \quad (3.5)$$

Once more and taking into account the definitions [10]:

$$\sigma_{tot} = q(\mu_n n + \mu_p p) \text{ and } \sigma_d = q(\mu_n n_o + \mu_p p_o) \quad (3.6)$$

If we substitute (3.6) in (3.5), it comes:

$$\sigma_{ph} = q(\mu_n (n - n_o) + \mu_p (p - p_o)) \quad (3.7)$$

If one introduces the electrons and holes generation rates G_n and G_p and the electrons and holes lifetime τ_n et τ_p before they recombine, and knowing that when the steady state regime is established the rate of generation is equal to the rate of recombination [13] i.e.:

$$G_n = \frac{n - n_o}{\tau_n} \text{ and } G_p = \frac{p - p_o}{\tau_p}, \text{ the equation (3.7) becomes:}$$

$$\sigma_{ph} = q(\mu_n \tau_n G_n + \mu_p \tau_p G_p) \quad (3.8)$$

where $(n - n_o)$ and $(p - p_o)$ denote the excess of charges due to the optical excitation.

For the amorphous semiconductors, photoconductivity is proportional to the generation rate G^γ , γ being the Rose factor [12, 13] which takes values between 0.5 and 1 depending on the incident photons intensity and the temperature. For the crystalline semiconductors as an example, it takes the value unit for weak excitations and corresponds in this case to the monomolecular recombination mechanism, or it is equal to 0.5 for highly optical excitations and corresponds to the bimolecular recombination mechanism [10, 13].

Like it was mentioned in chapter 1, the localized states present in the band gap mobility of the a-Si:H play a very significant role in the mechanism of recombination. Indeed, the shallow states close to the edges mobility act as traps i.e. the charge carriers captured by these states have more possibility of being re-emitted towards the extended states than to recombine. On the contrary, the charge carriers trapped close to the center of the band gap mobility by the deep states, which act as recombination centers, have more probability to recombine. In order to well understanding this phenomenon, it is crucial to know the different occupation functions of the localized states in non-equilibrium conditions.

At thermal equilibrium (in the dark condition), the occupation functions follow the statistics of Fermi-Dirac. While, when this thermal equilibrium is distributed by continuous illumination till steady state regime is established, the occupation functions follow in this case the statistics of Simmons and Taylor [12, 14] that we propose to present in what follows.

Figure (3.3) illustrates the two mechanisms determining the occupation of the gap states: (1) capture of an electron and a hole by the state E ((a) and (b)) and (2) thermal emission since E

towards the nearest extended band ((c) and (d)). In steady state condition the sum of the rates (a) and (b) must be equal to the sum of the rates (c) and (d).

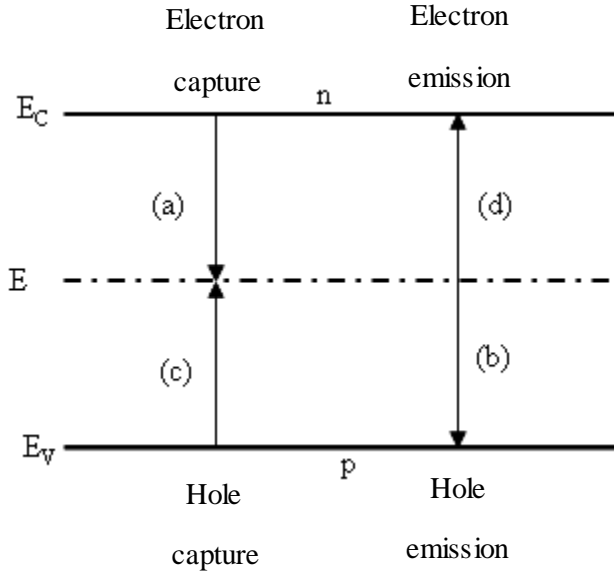


Figure 3.3: Mechanisms of capture and emission

The occupation function is given by [12]:

$$f(E) = \frac{nC_n + pC_p}{nC_n + e_n(E) + pC_p + e_p(E)} \quad (3.9)$$

Firstly, let us consider the case of the localized states behaving rather as centers of recombination where the capture coefficient is much higher than the emission coefficient. We define the relative capture coefficient $r(S)$ at energy E for each type of state S by:

$$r(S) = \frac{C_n(S, E)}{C_p(S, E)} \quad (3.10)$$

That means all the states of the type S having the same ratio $r(S)$ have the same occupation function independently of their absolute values of capture C_n and C_p and their positions E . Hence, the function of occupation f becomes then:

$$f = \frac{r(S)n}{r(S)n + p} \quad (3.11)$$

Hereafter, one takes into account the thermal emission towards the extended states i.e., instead that the electron (hole) captured by the state E recombines with a hole (electron) in the valence band (conduction), it is re-emitted towards the conduction band (valence). The preceding formula of the occupation function f for electrons above E_F is modulated of following manner: [14]

$$f = \frac{r(S)n}{r(S)n+p} \cdot \left[1 + \exp\left(\frac{E - E_F^n}{K_B T}\right) \right]^{-1} \quad (3.12)$$

where E_F^n represent the quasi- Fermi level for the trapped electrons and corresponds to a half-modulation.

By the same procedure for the hole occupation function, it is modulated as follows:

$$1-f = \frac{r(S)n}{r(S)n+p} \cdot \left[1 + \exp\left(\frac{E - E_F^p}{K_B T}\right) \right]^{-1} \quad (3.13)$$

where E_F^p represent the quasi- Fermi level for the trapped holes.

In short, all states between two levels E_F^n and E_F^p act like center of recombination and all the states situated elsewhere react like traps.

Figure (3.4) shows the occupation function f for the case $r(S)=2$ and $n=p=10^{-8}\text{cm}^{-3}$ [14].

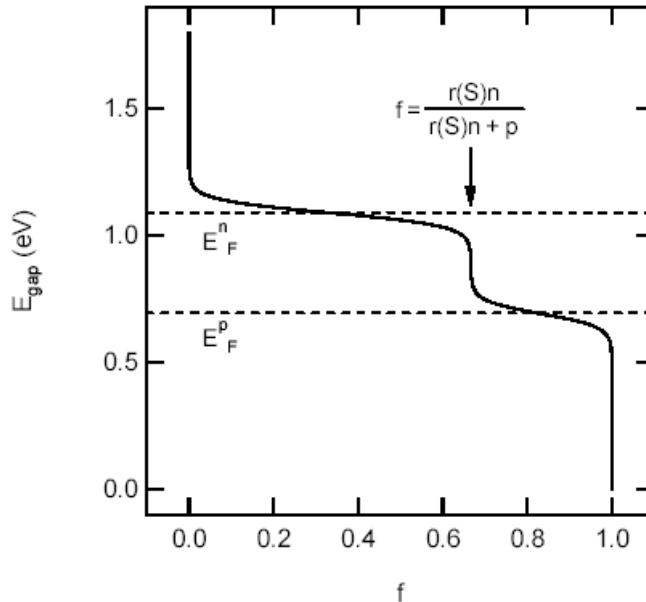


Figure 3.4: Occupation function of electrons calculated according to the statistics of Simmons and Taylor [14] for $r(S) = 2$ and $n=p = 10^{-8} \text{ cm}^{-3}$

If the optical excitation is periodic the response of the amorphous semiconductor, so-called modulated photoconductivity, is also periodic but with a delay of phase compared to the excitation which in turn depends on the frequency of excitation. The phenomenon of recombination in this case occurs after a multi-trapping process of the charge carriers which are held during a time τ_R defined as recombination time. We will review this point in the next chapter.

3.4. Constant photocurrent measurement

We will present in what follows a detail study of the CPM method and in the following chapters we will focus on modeling side of this technique.

The technique of constant photocurrent or CPM was introduced by Vanecek et al. [20]. The basic idea of the constant photocurrent technique is to adjust the photon flux $\phi(h\nu)$ of such manner that photoconductivity remains constant through the sample for all incident photons energy $h\nu$. Under these conditions, one ensures that the occupation of the electronic states is constant as well as the concentration of the photo-generated carriers. Under these circumstances, the $\mu\tau$ product remains constant for all used wavelengths λ . CPM experiment allows us to measure weak absorption corresponding to the deep defects. This makes possible to deduce the nature and the energy distribution of the deep defects in the gap starting from the measurement of the optical absorption coefficient $\alpha(h\nu)$. The exponential region of the absorption in the valence band tail is also referred to as the Urbach regime, as was already indicated in section 2.2. The inverse logarithmic slope of the absorption coefficient in this regime is denoted as the Urbach energy E_0 .

The defect density is calculated from the value of α at the intersection of the weakly increasing contribution of the deep defect states, and the exponentially increasing contribution of the valence band tail states. For this, a proportionality constant of 10^{16} cm^{-2} is usually used [51]. CPM experiment has the advantage compared to technique PDS (see next item) of being insensitive to the surface defects.

Figure 3.9 illustrates an example of set up used for the optical absorption measurement by the constant photocurrent method.

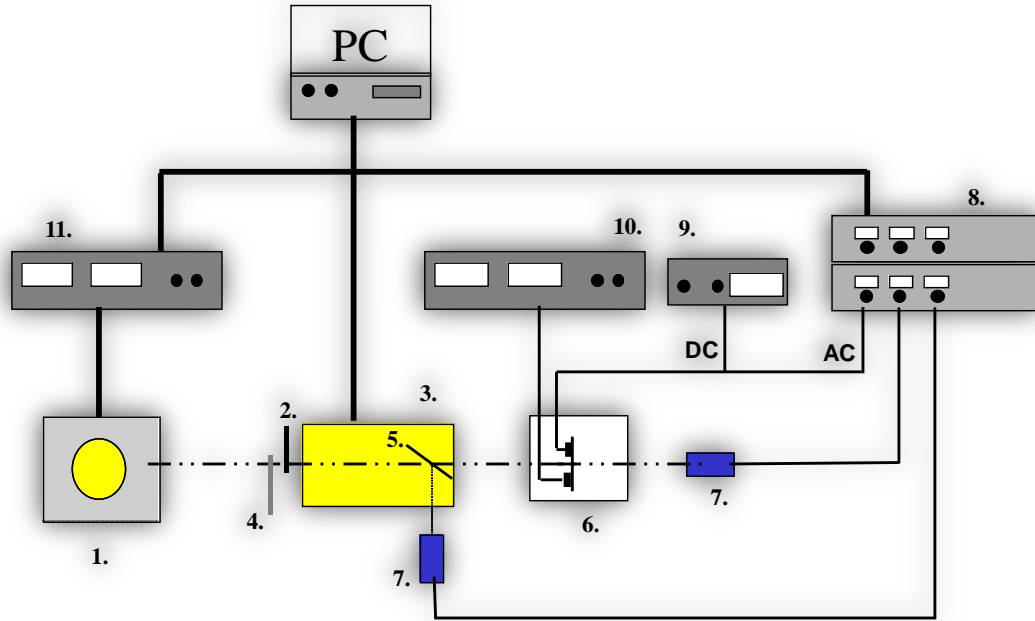


Figure 3.9: Constant photocurrent technique setup

This technique is based on the measurement of the photoconductivity at low photon energies.

Under uniform illumination, the measured photoconductivity can be written as

$$\sigma_{ph}(h\nu) = q \mu(h\nu) \tau(h\nu) G(h\nu) \quad (3.14)$$

where q is the electronic charge unit, μ the mobility of the conducting electrons and τ the carrier lifetime.

The generation rate G represent the density of charge carriers which are generated per second by the illumination. It is proportional to the photon flux $\phi(x)$ via :

$$G(x) = \eta \alpha(h\nu) \phi(x) \quad (3.15)$$

in which $\alpha(h\nu)$ is the absorption coefficient spectrum, and η is the quantum efficiency, or the fraction of absorbed photons that generate free carriers.

$\phi(x)$ is the photon flux at a depth x in the material, when the sample is illuminated with monochromatic light at a photon flux $\phi_{ph}(h\nu)$, and it is given by :

$$\phi(x) = (1 - R) \phi_{ph}(h\nu) e^{-\alpha(h\nu)x} \quad (3.16)$$

in which R is the reflectance of the sample,.

In the energy regime where the absorption coefficient is small ($\alpha d \ll 1$), the average generation rate over the whole thickness d of the layer can be approximated as follow:

$$G(h\nu) = \eta (1 - R) \phi_{ph}(h\nu) \alpha(h\nu) \quad (3.17)$$

Knowing that $\sigma_{ph} = \frac{I_{ph} w}{V l d}$, the photocurrent can be now given by

$$I_{ph}(h\nu) = q \frac{l d}{w} V (1 - R) \eta \mu \tau (h\nu) \phi_{ph}(h\nu) \alpha(h\nu) \quad (3.18)$$

in which l is the width of the electrodes, w the distance between the electrodes, V the applied voltage, and d the thickness of the film.

The lifetime τ of the charge carriers is dependent on the recombination rate of the free carriers. However, when the photocurrent is kept constant for all monochromatic photon energies $h\nu$, the carrier lifetime is, in good approximation, also constant. Furthermore, the mobility μ is assumed to be constant.

Due to the optical thickness of the thin films, interference fringes appear in the experimental absorption spectrum. As the intensity of the transmitted light and reflected light was not measured, the term $(1-R)$ in equation (3.18) is assumed to be constant, and no correction is made for the presence of the interference fringes [50]. These fringes can, in first approximation, be averaged out from the absorption spectrum.

The reflectivity R is usually supposed to be null and quantum efficiency η is considered equal to the unit, the equation (3.18) is reduced then to:

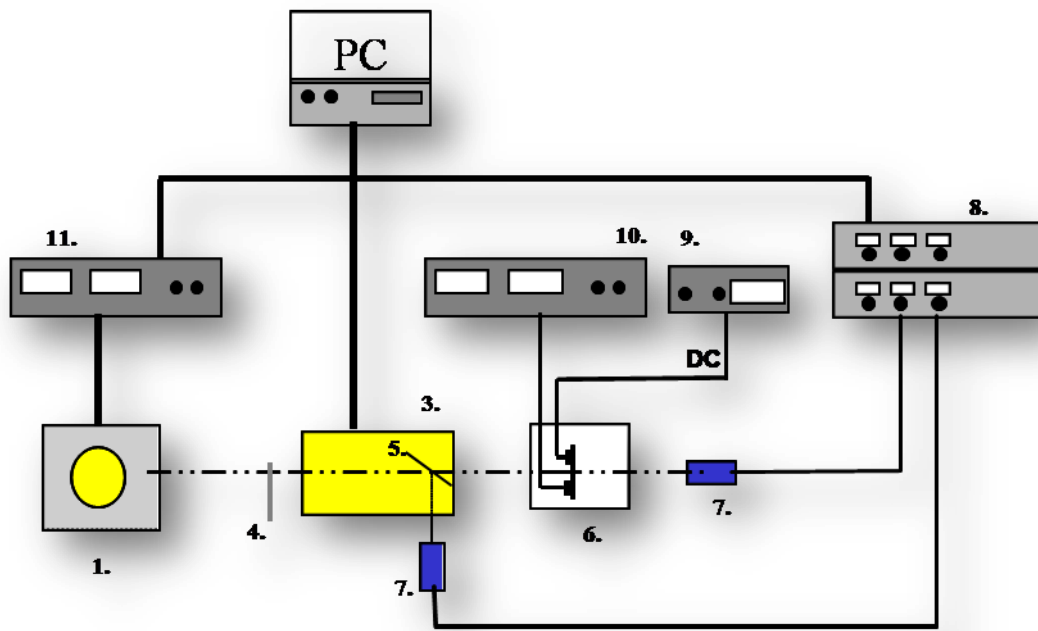
$$G(h\nu) \propto \alpha(h\nu) \cdot \phi(h\nu) \quad (3.19)$$

As $G(h\nu)$ is constant, the resulting absorption coefficient is dependent only on the incident photon flux and given by

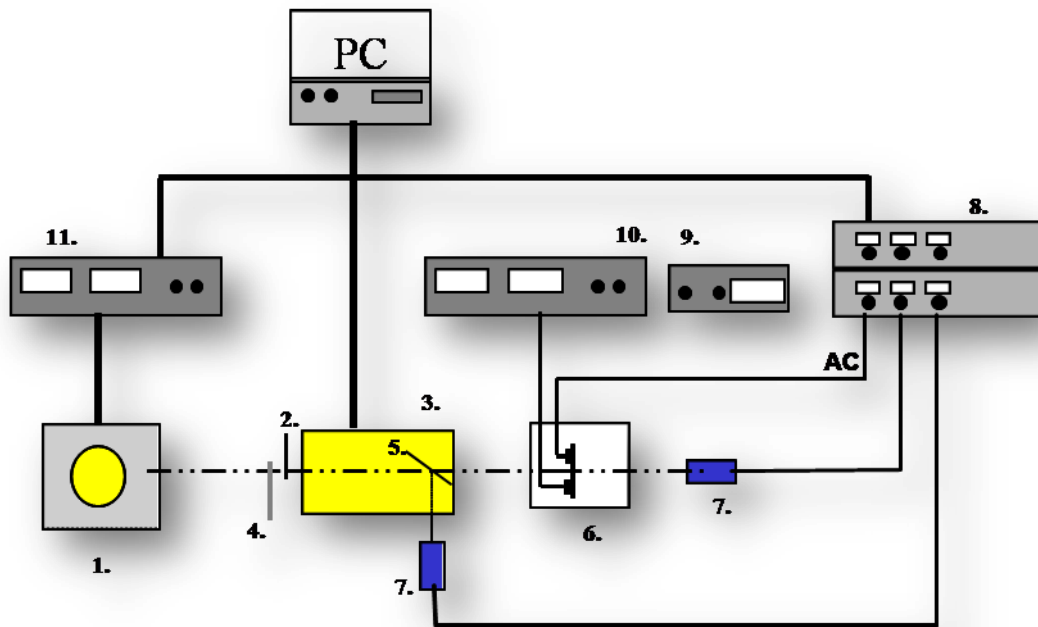
$$\alpha(h\nu) \phi(h\nu) = Cte \Leftrightarrow \alpha(h\nu) \propto \frac{1}{\phi(h\nu)} \quad (3.20)$$

where C is an energy independent constant. This constant, and thus the absorption coefficient $\alpha(h\nu)$, is calibrated with the absolute absorption coefficient obtained from reflection/transmission measurements or from PDS measurements (see next item). Nevertheless, absolute values of $\alpha(h\nu)$ can be obtained directly by using absolute technique CPM experiment. This technique is the combination of the standard CPM and the transmission CPM where a second detector is placed behind the sample [21, 22].

In the end, this technique can be configured in the continuous mode (DC mode) [23], or in the periodic mode (AC mode) [24, 25, 26]; both are largely used. This subject will be covered in chapter 4 and 5.



dc-CPM Mode



ac-CPM Mode

Required instruments:

1. W-halogen lamp
2. Optical chopper
3. Monochromator
4. Filters wheel
5. Beam splitter
6. Cryostat+ Sample
7. Detectors
8. Lock-in amplifier
9. Electrometer
10. Sample power supply
11. Lamp power supply

Figure 3.10 shows a typical example of optical absorption measurement by the absolute and the standard constant photocurrent method [21].

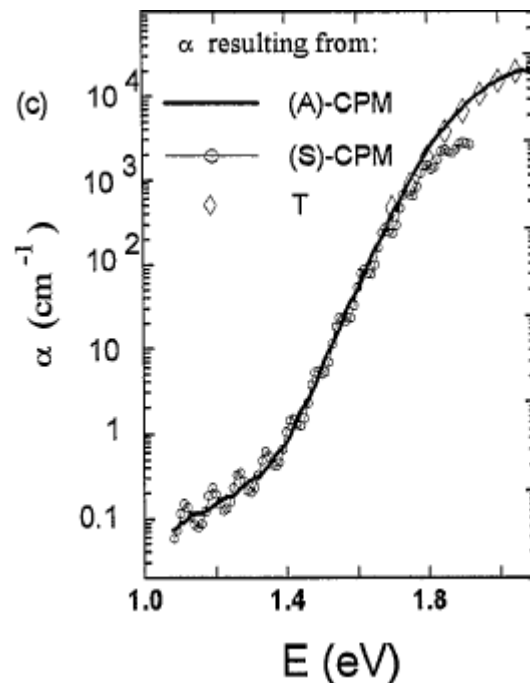


Figure 3.10: Optical absorption spectrum of the a-Si:H measured by CPM [21]

3.5. Photothermal deflection spectroscopy (PDS)

Another method to measure the sub-bandgap absorption is the photothermal deflection spectroscopy (PDS) technique. Boccara et al. [15] developed this optical method since 1980 and Jackson et al. [4] made the first PDS measurements of the optical absorption edge and defect transitions of a-Si:H samples deposited at different RF power. With this technique it is possible to measure small values of absorptance αd in the deposited layers, typically down to 10^{-5} . This allows the determination of the density of mid-gap states in amorphous silicon, as well as the determination of the indirect bandgap of microcrystalline and polycrystalline films, which have a low absorption coefficient.

The experimental setup of PDS is sketched in figure 3.11.

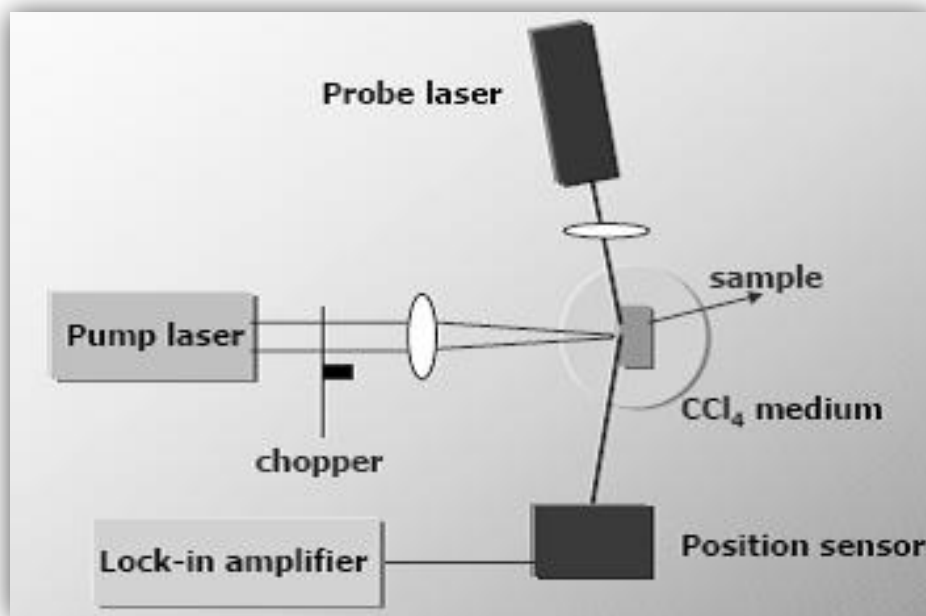


Figure 3.11: Experimental setup of the PDS measurement

The technique is based on the dissipation of absorbed energy into heat.

A monochromatic high intensity light beam issued from a monochromator is modulated by mechanical chopper and focused on the sample. This latter is immersed in a non-absorbing and thermally conductive liquid (e.g. CCl₄) which have a highly temperature dependent index of refraction characteristic. Depending on the wavelength of the incident light, absorption

may occur. The absorbed energy is subsequently dissipated into heat in the surrounding liquid, a gradient change in the refractive index of the liquid close to the sample surface is established. As a result, a laser beam (e.g. He-Ne laser) directed parallel to the sample surface is deflected. The deflection signal is measured by a position sensitive detector, which is connected to a lock-in amplifier.

The angle of deflection $\Delta\theta$ of the probe beam is found to be proportional to the absorption coefficient α [53]. Knowing the film thickness d and the appropriate value of derivative of the refractive index of the liquid with respect to the temperature $\frac{dn}{dT}$, the spectral dependence of the absorption coefficient $\alpha(h\nu)$ can be calculated according to the equation [53]:

$$\Delta\theta \propto L \frac{dn}{dT} I_0 \alpha d \quad (3.21)$$

in which L is the width of the pump beam spot parallel to the direction of the laser beam and I_0 is the pump beam intensity.

Measuring both the deflection of the laser beam and the intensity of the monochromatic pump beam at different wavelengths thus yields a relative absorption spectrum of the material. For short wavelengths, all light is absorbed in the film and the absorption spectrum becomes flat where $\alpha d \geq 1$. To obtain absolute absorption spectra, the data were scaled either to the $\alpha(h\nu)$ data from reflection/transmission measurements, or to the region where $\alpha \cdot d$ equals 1. The indirect optical bandgap of microcrystalline and polycrystalline silicon can be derived from a plot of $\sqrt{\alpha}$ versus $h\nu$.

This measurement is widely used in the field of amorphous silicon, it is used to estimate the density of defects since a proportionality exists between optical absorption coefficient and the density of defects where absorption is controlled by the transitions between these defects and the extended bands. These transitions are excited by photons of energy lower than the mobility band gap width. According to the method suggested by Wyrsh [17], one can deduce the density of defects by multiplying absorption at 1.2eV by a factor of calibration equal to $2.10^{16} \text{ cm}^{-2}$:

$$\alpha(h\nu) = 2.10^{16} N_d \quad (3.22)$$

Although the CPM and PDS techniques are both used to measure the sub-bandgap absorption, the defect absorption measured in the case of PDS is significantly larger than in the case of CPM. The Urbach tail, however, is identical for both techniques. The difference in defect absorption has often been attributed to the contribution of surface defect states or of the

layer/substrate interface. However, it seems more likely that the difference is due to different sensitivities of the techniques to charged and neutral defect states, as the CPM technique is only sensitive to charged defect states, and the PDS technique is sensitive to both charged and neutral states.

Figure 3.12 shows a typical example of optical absorption in a-Si:H measured by PDS where exponential tail (Urbach tail) and deep defects absorption ranges are clear.

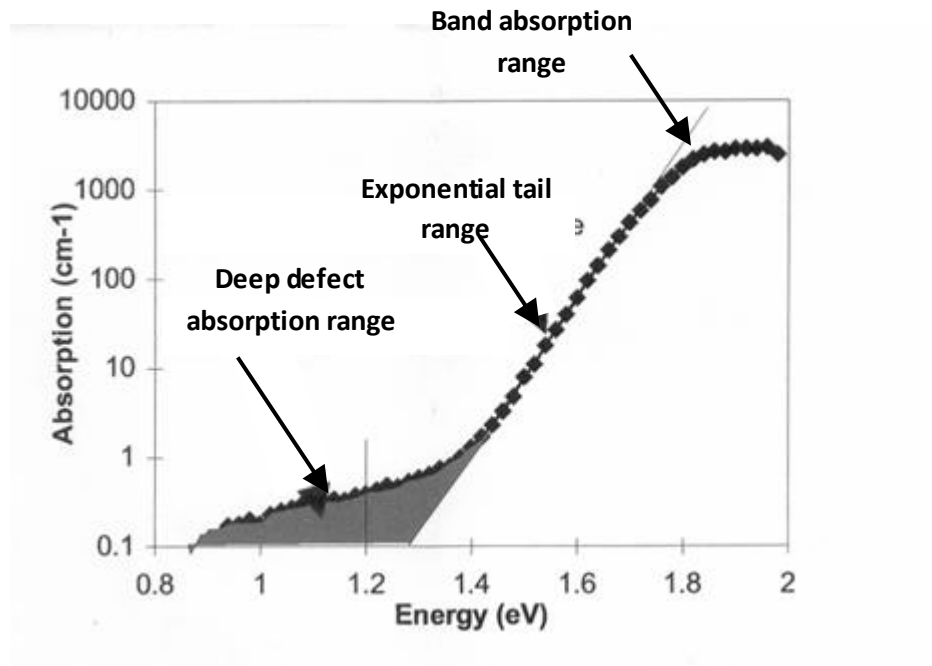


Figure 3.12: Optical absorption spectrum of the a-Si:H measured by PDS [17]

- **Advantages and disadvantages**

Like any measurement, PDS technique has some advantages and certain disadvantages. Among these advantages one can name:

- Measures all possible transitions;
- Highly sensitive technique (α down to 0.1 cm^{-1});
- Easy to use.

Nevertheless, this method suffers from the following principal disadvantages:

- Indirect method ;
- PDS technique is quite sensitive to the mechanical vibration and dust, a residual absorption of substrate can be a problem.

- Measurements must be calibrated to measurements of optical Transmission-Reflection measurements at 1.7eV;
- Sensitive to both surface/interface and bulk states especially for low thicknesses;
- Measurement is influenced by the nature of the substrate; if this latter is more absorbent than the sample (metallic contact for example), the measurement of the optical absorption of the layer is not possible;
- Measurements cannot be taken in situ i.e. during the process of film deposition;
- For accurate measurement, a series of high quality films with thicknesses $> 10 \mu\text{m}$ must be investigated.

3.6. Dual beam photoconductivity (DBP)

Dual beam photoconductivity method is one of the sub-band gap absorption spectroscopy. In this technique, two light beams AC and DC are used. In this method two beams of light AC and DC are used. The monochromatic probe light of intensity ϕ is periodic of fixed frequency usually of 10Hz to 1000Hz [18]. It is used to probe the band gap of the material and the resulting photoconductivity is measured using a lock-in amplifier. The continuous bias light of constant intensity ϕ_o is used to generate free carriers by changing the occupation of the gap states. Consequently maintaining the quasi- Fermi levels E_F^n and E_F^p constants.

Thus, by using a range of constant flux (varied generation rates), more deep states are occupied by the electrons (case of photoconductivity type N) what implies more transitions towards the conduction band. As a result, the coefficient absorption is higher so easier to detect.

The condition $\phi \ll \phi_o$ must be taken into account for this technique. Under this condition, continues excitation $\phi_o(h\nu)$ and periodic photoconductivity $\sigma_{ph}(h\nu)$ resulting from the periodic excitation, are in linear relationship with the optical absorption coefficient $\alpha(h\nu)$ according to the following formula [19]:

$$\alpha(h\nu) = \frac{\sigma_{ph}(h\nu)}{\text{Cte} \cdot \phi_o(h\nu)} \quad (3.23)$$

Cte being the constant of proportionality.

The main advantage of this technique over constant photocurrent method is that the generation rate of bias light can be increased so that quasi Fermi levels are extended and thereby more midgap defect states can be detected.

The following illustration shows an example of experimental setup of DBP technique used by the group composed by Professor Mehmet Güneş of the University of Izmir, Turkey [19].

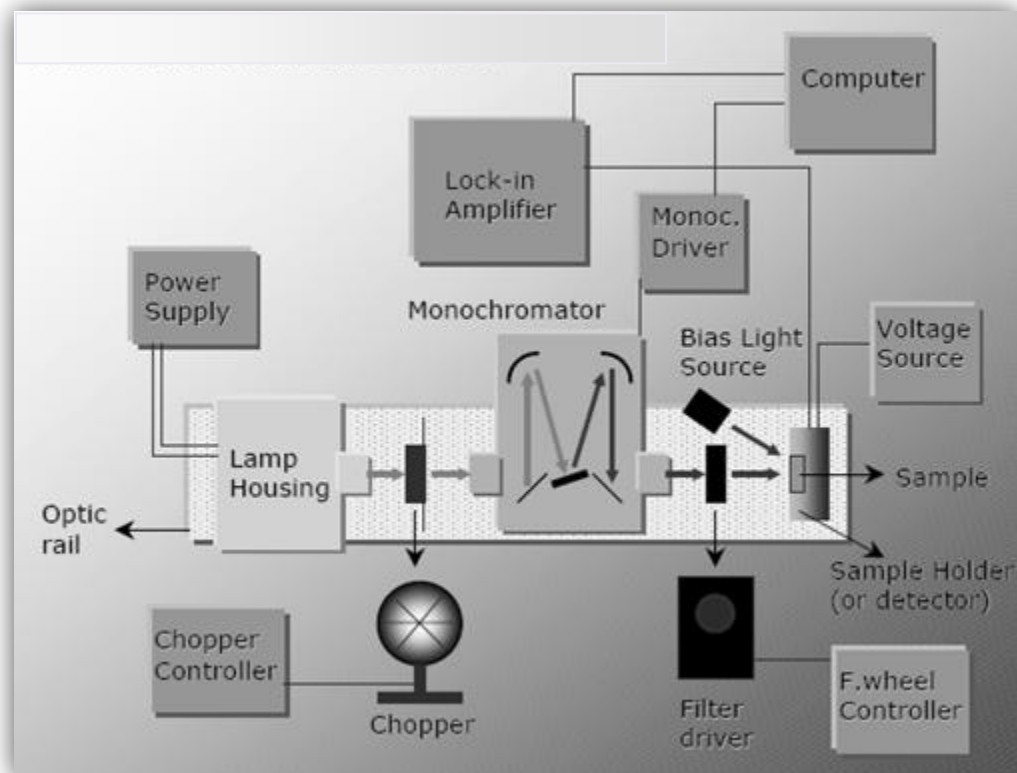


Figure 3.13: Experimental setup of DBP technique after Mehmet's group [19]

Figure 3.14 shows the result obtained by using the preceding DBP setup.

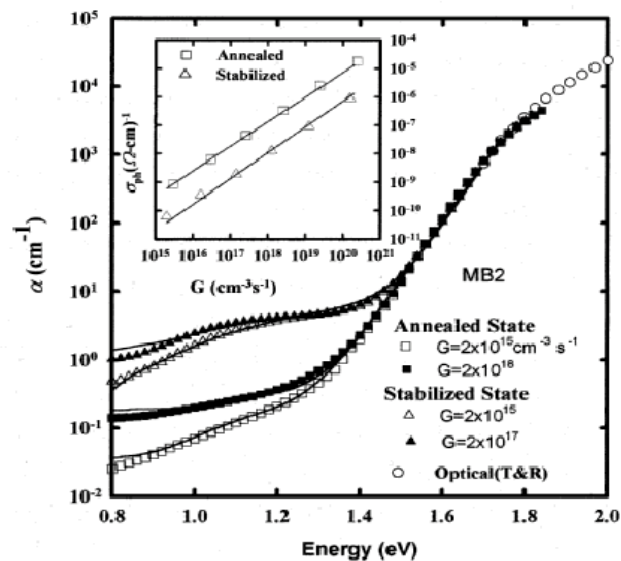


Figure 3.14: Optical absorption spectrum of the a-Si:H measured by DBP [19]

- **Advantages and disadvantages**

DBP technique is among the techniques of characterization which are largely commented and illustrated. It profit of the following advantages:

- Very significant method of measurement, practically one can measure absorptions lower than 0.1 cm^{-1} ;
- It is not sensitive to the defects of surfaces;
- By using different generation rates the midgap states below and above the Fermi level can be also probed ;
- Allows studying the S-W effect;
- Allows to improve the signal-to-noise ratio;

Elsewhere, this technique as others suffers from some problems namely, that is:

- Indirect method to derivate the DOS;
- Measurements must be calibrated to measurements of optical Transmission-Reflection measurements at 1.7eV;
- Measured optical absorption coefficient $\alpha(h\nu)$ is influenced by the phenomenon of interference;
- Measurements cannot be taken in situ i.e. during the process of film deposition;

References

- [1] H. Matsuura, "Electrical properties of amorphous/crystalline semiconductor heterojunctions and determination of gap-state distributions in amorphous semiconductors", Ph.D.thesis, Kyoto University, Japan, 1994.
- [2] A. Treatise, "Semiconductors and Semimetals", Volume 21, Part C, Academic Press Inc., Orlando, Florida, USA, 1984.
- [3] V. Cech and J. Stuchlik, *Phys. Stat. Sol. (a)* 187, No. 2, 487-491 (2001).
- [4] W. B. Jackson, N. M. Amer, A. C. Boccara, and D. Fournier, *Applied Optics* **20**(8) (1981) 1333-1344.
- [5] J. S. Payson, and S. Guha, *Physical Review B*, Vol. 32, No.2, pp. 1326-1329, July 1985.
- [6] I. -S. Chen, L. Jiao, R. W. Collins, C. R. Wronski, *Journal of Non-Crystalline Solids* 198-200 (1996) 391-394.
- [7] M. Günes, C. R. Wronski and T. J. McMahon, *J. Appl. Phys.* 76 (4), 15 August 1994.
- [8] M. Vaněček, J. Kočka, A. Poruba, and A. Fejfar, *J. Appl. Phys.*, 78 (10), 15 November 1995.
- [9] M. Sarr, J. L. Brebner, *Solar Energy Materials and Solar Cells* 70 (2002), 459-467.
- [10] R. A. Street, "Hydrogenated amorphous silicon", Cambridge university press, 1991.
- [11] M. F. Thorpe and L. Tichy, "Properties and Applications of Amorphous Materials", Proceedings of NATO Advanced Study Institute, Czech Republic, 25 June-7 July 2000.
- [12] D. P. Webb, "Optoelectronic properties of amorphous semiconductors", Ph.D.thesis, University of Abertay, Dundee, UK, October 1994.
- [13] A. Merazga, "Steady state and transient photoconductivity in n-type a-Si", Ph.D.thesis, Dundee Institute of Technology, Dundee, UK, 1990.
- [14] S. Heck, "Investigation of light-induced defects in hydrogenated amorphous silicon by low temperature annealing and pulsed degradation", PhD Thesis, der Philipps-Universität Marburg, Marburg/Lahn 2002.
- [15] A. C. Boccara, D. Fournier, J. Badoz, *Appl. Phys. Lett.* 36 (2), 130 (1980).
- [16] T. Searle, "Properties of Amorphous Silicon and its Alloys", Edited by University of Sheffield, UK, 1998.

- [17] Patrick Chabloz, “Les couches épaisses en silicium amorphe, application comme détecteurs de rayon X”, Thèse N 1485, Ecole polytechnique fédérale de Lausanne, France, 1996.
- [18] S. Lee, S. Kumar, C. R. Wronski, N. Maley, *Journal of Non-Crystalline Solids* 114 (1989) 316-318.
- [19] M. Günes, C. R. Wronski, *J. Appl. Phys.* Vol. 81, No. 8, 15 April 1997.
- [20] A. Třiška, I. Shimizu, J. Kočka, L. Tichý and M. Vaněček, *Journal of Non-Crystalline Solids* 59-60 (1983) 493-496.
- [21] A. Fejfar, A. Poruba, M. Vaněček, and J. Kočka, *Journal of Non-Crystalline Solids* 198-200 (1996) 304-308.
- [22] K. Haenen, “Optoelectronic study of phosphorous-doped n-type and hydrogen-doped p-type CVD diamond films”, Ph.D.thesis, Limburgs Universitair Centrum, Belgium, 2002.
- [23] J. A. Schmidt and F. A. Rubinelli, *J. Appl. Phys.*, 83 (1), 339 (1998).
- [24] P. Sladek and M. L. Theye, *Solid State Comms.* Vol.89, No. 3, pp.199, 1994.
- [25] S. Hasegawa, S. Nitta and S. Nonomura, *Journal of Non Crystalline Solids* 198-200 (1996) 544-547.
- [26] C. Main, S. Reynolds, I. Zrinscak and A. Merazga, *Journal of Materials Science- Materials in Electronics*, 2003.

CHAPTER 4

CONSTANT PHOTOCURRENT TECHNIQUE: THEORY AND MODELING

4.1. Introduction

Constant photocurrent method was introduced in the field of a-Si:H by Vanecek et al [1] and since then it has been widely used to investigate the density of dangling bonds defects of many other amorphous and composite thin films as amorphous-nanocrystalline, amorphous-microcrystalline, diamond-like carbon, etc [2]. A diverse numerical model has been developed to simulate CPM spectrum taking into account the position of the Fermi energy level and the full set of optical transition between localized and extended states under sub-band-gap optical excitation, capture, emission and recombination processes [3-6]. Explanation and modeling in the literature assume that CPM gives information about the density of localized gap states in amorphous silicon that is the valence band tail, the integrated defect density, the energy defect distribution and the charge state of the defect states.

Following a review on the most important theoretical points of the CPM method, attention is devoted to the numerical modeling of the DC-CPM and AC-CPM to get more information needed for the determination of the defect densities in the gap energy of semiconductors materials and for the interpretation of the large discrepancy between the DC and AC constant photocurrent method.

4.2. Density of states distribution models

In this section a description of the two existing models of the DOS in a-Si:H, as an example, are introduced, since it will be implemented in our code program. The common part between

these two models are: the conduction and the valence band (CB and VB) which are assumed to be parabolic like for crystalline semiconductors, and the conduction and valence band tail (CBT and VBT) described by an exponential decay towards the midgap. The two models differ from each other by the deep defects known as dangling bonds.

4.2.1 Extended states

We mean by extended states the parabolic CB ($D_{cb}(E)$) and VB ($D_{vb}(E)$) bands which are determined by three parameters. These parameters are the mobility edge level, the corresponding DOS and the bending parameter; $(E_C^{mob}, D_C^{mob}, D_C^o)$ for conduction band and $(E_V^{mob}, D_V^{mob}, D_V^o)$ for valence band as depicted in figure 4.1.

Since the mobility edge of the conduction (valence) band is defined to be relative to the origin of the parabolic conduction (valence) band as $E_C^{mob} = E_C + \varepsilon_C$ ($E_V^{mob} = E_V - \varepsilon_V$), the parameters ε_C and ε_V are threshold energies, we have to distinguish between the mobility and optical band gap (E_{gap}^{mob} and E_{gap}^{opt}). They are defined as follow (see figure 4.1):

$$E_{gap}^{mob} = E_C^{mob} - E_V^{mob} \quad (4.1)$$

$$E_{gap}^{opt} = E_C - E_V \quad (4.2)$$

The states in the conduction (valence) band above (below) the mobility edge E_C^{mob} (E_V^{mob}) are delocalized. They are occupied with electrons (holes) that are defined by the charge carrier density n (p) and the positive extended-state mobility μ_n (μ_p).

The mathematical description of the energy distribution of these states is given by the following formulas:

$$D_{cb}(E) = D_C^o \sqrt{E - E_C} \quad (4.3)$$

$$D_{vb}(E) = D_V^o \sqrt{E_V - E} \quad (4.4)$$

4.2.2. Tail states

We mean by tail states the exponential VBT ($D_{vbt}(E)$) and CBT ($D_{cbt}(E)$) states which are described by the characteristic tail slopes and the connection points where the parabolic bands

are connected to the exponential tails; $(E_C^o, E_C^{tail}, D_C^{tail})$ for CBT states and $(E_V^o, E_V^{tail}, D_V^{tail})$ for VBT states as illustrated in figure 4.1.

These states are localized and because the hopping is neglected within the mobility gap, the mobility of both charge carriers is supposed to be null ($\mu_n = \mu_p = 0$). Their natures behave like ordinary acceptor-like for CBT states and ordinary donor-like for VBT states.

The mathematical description of the energy distribution of these states is given by the following formulas [7]:

$$D_{cbt}(E) = D_C^{tail} \exp\left(-\frac{E_C^{tail} - E}{E_C^o}\right) \quad (4.5)$$

$$D_{vbt}(E) = D_V^{tail} \exp\left(-\frac{E - E_V^{tail}}{E_V^o}\right) \quad (4.6)$$

with:

$$E_C^{tail} = E_C + \frac{E_C^o}{2} \quad D_C^{tail} = D_C^o \sqrt{\frac{E_C^o}{2}} \quad (4.7)$$

$$E_V^{tail} = E_V - \frac{E_V^o}{2} \quad D_V^{tail} = D_V^o \sqrt{\frac{E_V^o}{2}} \quad (4.8)$$

4.2.3. Deep defect states

We mean by deep defect states the dangling bonds. The latter are the most significant characteristic of amorphous semiconductors compared with its crystalline partners. Two models distribution for these deep defects are presented here; standard and defect pool models.

A. Standard model

In this model the DB are described by a Gaussian distribution. Unlike the tail states, these deep defects states are amphoteric [8]. It is assumed that these dangling bonds with a finite correlation energy U have three possible electron states: double-occupied (D), single-occupied (D^o) or non-occupied (D^+). Thus, with these three possible charge states, defect acts like a group of two defects consisting of an acceptor-like state ($D^{o/-}$) and a donor-like state ($D^{+/o}$) and therefore represented by two transition energy levels $E^{o/-}$ and $E^{+/o}$ separated from each other by U . In other words, the dangling bonds are represented by two equal

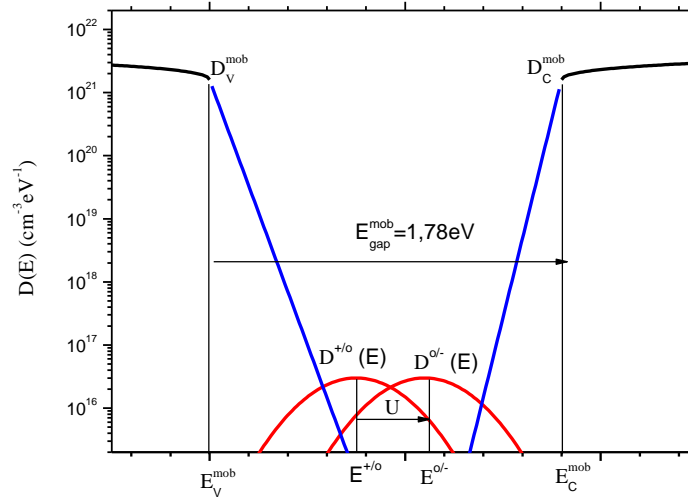
Gaussian distributions in the band diagram separated from each other by constant and positive correlation energy as shown in figure 4.1.

The mathematical description of the energy distribution of these states is given by:

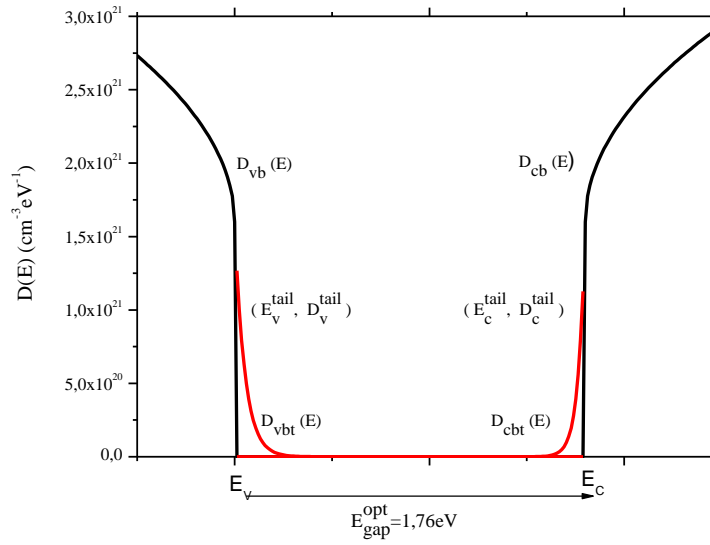
$$D^{o/-}(E) = \frac{D_{DB}^{tot}}{\sigma_{DB} \sqrt{2\pi}} \exp\left(-\frac{(E - E^{o/-})^2}{2\sigma_{DB}^2}\right) \quad (4.9)$$

$$D^{+/o}(E) = \frac{D_{DB}^{tot}}{\sigma_{DB} \sqrt{2\pi}} \exp\left(-\frac{(E - E^{+/o})^2}{2\sigma_{DB}^2}\right) \quad (4.10)$$

where D_{DB}^{tot} is the integrated density of defects and σ_{DB} is the standard deviation of the distribution.



(a) Logarithmic scale



(b) Linear scale

Figure 4.1: DOS distribution according to the standard model

B. Defect pool model

The difference between the two models is that the distribution of DB states in the standard model is based on the idea that the structural disorder leads to a Gaussian distribution and does not take into account the origin of these states. While in the defect pool model the DB distribution is based on the weak bond (Si-Si)-dangling bond conversion model [9] with the involvement of hydrogen diffusion and therefore depends on the position of the Fermi level (see Figure 4.3). This theory introduced by Winer [10] and modified by others including Dean and Powell [11, 12, 13] has attracted a lot of attention since it could successfully applied to both doped and undoped a-Si:H in thermal equilibrium and also the metastable defect formation in non-equilibrium states [14, 15]. The broken dangling bonds can be saturated and separated spatially so as to reduce the free energy of the system to a minimum.

The following expression for the DB states distribution at equilibrium using Dean and Powell's second version [12] are used in our code:

$$D_{db}(E) = \gamma \left(\frac{2}{f_{th}^o(E)} \right)^{K_B T / 2E_v^o} P \left(E + \frac{\sigma^2}{2E_v^o} \right) \quad (4.11)$$

γ is the scaling factor depends on the number of Si-H bonds mediating the weak-bond breaking chemical reaction i_H ($i_H = 0, 1$ or 2), the total hydrogen concentration c_H , the pool width (standard deviation) σ_{dp} and the peak position of the Gaussian distribution (defect pool center) E_p . It is given by:

$$\gamma = \left(\frac{2 D_V^{tail} (E_V^o)^2}{2 E_V^o - K_B T} \right) \left(\frac{c_H}{N_{Si-Si}} \right)^{\frac{K_B T}{4 E_V^o}} \exp \left(-\frac{1}{2 E_V^o} \left(E_p - E_V - \frac{\sigma_{dp}^2}{4 E_V^o} \right) \right) \quad (4.12)$$

$f_{ih}^o(E)$ denote the equilibrium occupation function of neutral dangling bond states and N_{Si-Si} denotes the total number of electrons in the silicon bonding states.

$P(E)$ is the defect pool function which is described by a Gaussian distribution:

$$P(E) = \left(\frac{1}{\sqrt{2\pi} \sigma_{dp}} \right) \exp \left(-\frac{(E - E_p)^2}{2 \sigma_{dp}^2} \right) \quad (4.13)$$

Figure 4.3 illustrates the DB states distribution according to the position of the Fermi level which determine the peak position and the total number of dangling bonds

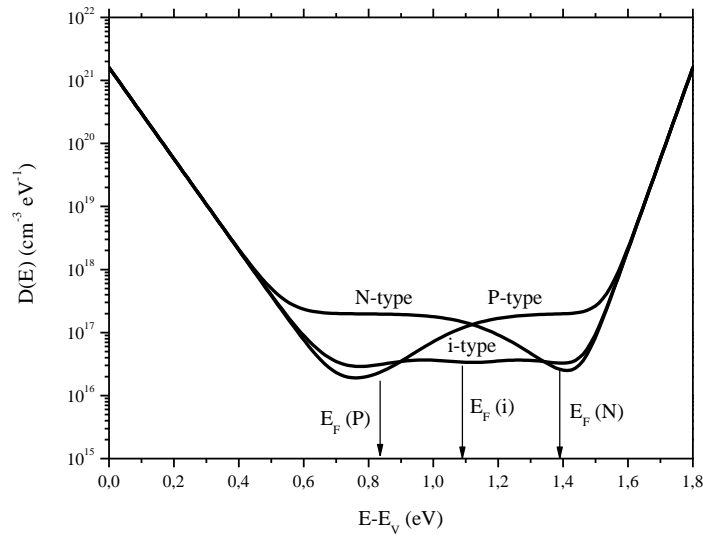


Figure 4.3: DOS distribution according to the defect pool model for intrinsic, n and p-type a-Si:H

4.3. Trapping and recombination

The DOS under consideration is divided into N discrete levels using energy scale indices j . It consists of two parabolic extended bands, two exponential tails and deep defects according to DPM second version [12]. Doping by donors or acceptors merely involves additional fixed charge states (totally ionized).

Figure 4.4 illustrates the thermal carrier transitions for the CPM in a-Si:H-like material for a uniform sub-gap illumination. While single level representation appears in the illustration, the DOS components CBT , VBT , D^0 , D^- and D^+ are energy-distributed. At room temperature, photoconduction is carried out by free carriers, and so the only transitions taken into account are those between localised states in the gap and extended states in the bands. It is worth to noting that neither the band-to-band transitions nor the transitions between localized states will be considered because of their smaller transition probabilities and their smaller densities of states [3, 4]

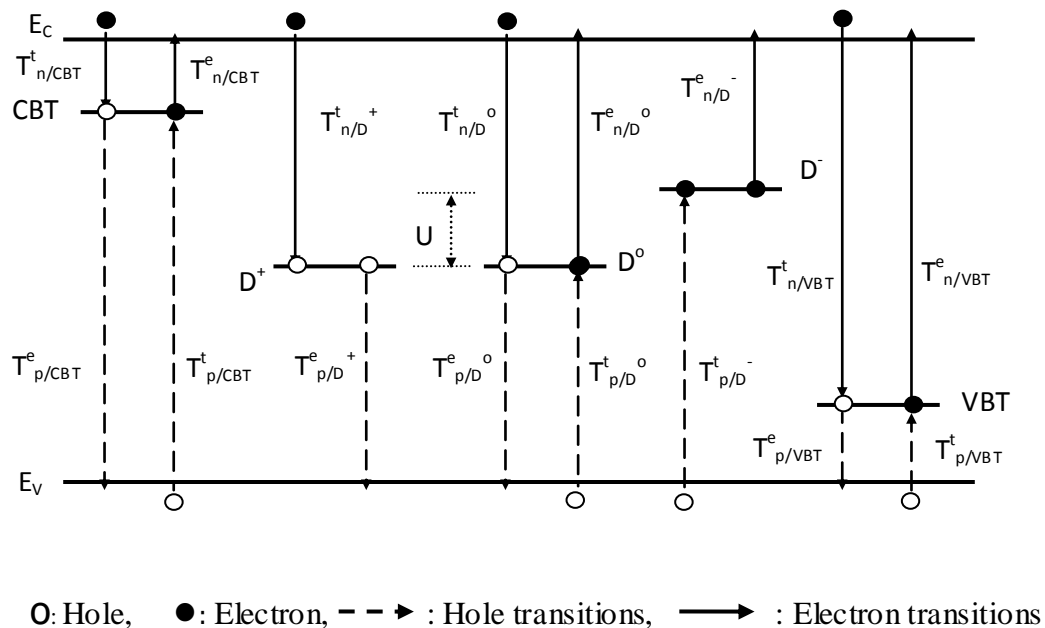


Figure 4.4: Carrier transitions involved in the CPM simulation: Thermal transitions with the rates $T_{n(p)/T(D)}^{(e)}$ signifying rate of trapping (emission) of electron (hole) into (from) Tail (Defect) states.

The thermal transition rates T have the following significance:

- $T_{n(p)/CBT(VBT)}^{(e)}(E)$: Rates of trapping (emission) of electron (hole) into (from) a level E at the conduction band tail (valence band tail).
- $T_{n/D^0(D^+)}^t(E)$: Rates of electron trapping into a D^0 (D^+) level E at the defect states distribution.
- $T_{n/D^0(D^-)}^e(E)$: Rates of electron emission from a D^0 (D^-) level E at the defect states distribution.
- $T_{p/D^0(D^-)}^t(E)$: Rates of hole trapping into a D^0 (D^-) level E at the defect states distribution.
- $T_{p/D^0(D^+)}^e(E)$: Rates of hole emission from a D^0 (D^+) level E at the defect states distribution.

The trapping rate is a function of free n (p) and trapped n_t (p_t) carrier densities following the relation

$$T_{n(p)}^t(E) = C_{n(p)} n(p) [D_t(E) - n_t(p_t)] \quad (4.14)$$

where $D_t(E)$ is the total DOS at level E and $C_{n(p)}$ is the capture coefficient of the trapping state. For trapping into D^0 , D^- and D^+ states, their respective density must replace $D_t(E) - n_t(p_t)$ in equation (4.14). Similarly, the emission rate is a function of trapped n_t (p_t) carrier densities following the relation

$$T_{n(p)}^e(E) = C_{n(p)} D_{CB(VB)} n_t(p_t) \exp\left(-\frac{|E - E_{CB(VB)}|}{k_B T}\right), \quad (4.15)$$

where $D_{CB(VB)}$ is the effective DOS at the conduction (valence) mobility edge $E_{CB(VB)}$ (k_B is Boltzmann constant and T the temperature). For emission from D^0 , D^- and D^+ states, their respective density must replace $n_t(p_t)$ in equation (4.15). For thermal transition expressions detail, see appendices A and D.

In the non-equilibrium steady state, the recombination rate at any state with energy E is equal to the difference between the total capture rate and the total re-emission rate of the electron (or holes) via different paths. The net recombination rate via tail states is given by the same formulae as for conventional photoconductivity simulation (Hall-Shockley-Read) with the exception that the modified occupation functions are used. In a similar way to the band tail situation, the recombination via dangling bond states can still be expressed as the difference between the total trapping rate and the total emission rate from the dangling bond states,

except we are now dealing with two sets of transitions at different energy levels, E and $E+U$ for each state, $D^{o/-}$ and $D^{+/o}$ [16, 17].

4.4. Absorption and generation

Figure 4.5 shows a typical optical absorption spectrum $\alpha(h\nu)$ for hydrogenated amorphous silicon a-Si:H and for comparison the absorption spectra of crystalline silicon c-Si and hydrogen-free amorphous silicon a-Si [18]. Generally, such absorption spectra can be divided into three parts [7, 18]: (i) the weak absorption region ($\alpha(h\nu) < 10 \text{ cm}^{-1}$) or so-called midgap absorption, (ii) the exponential tail, or the Urbach region ($10 \text{ cm}^{-1} < \alpha(h\nu) < 10^3 \text{ cm}^{-1}$), and (iii) the high absorption region ($10^3 \text{ cm}^{-1} < \alpha(h\nu) < 10^4 \text{ cm}^{-1}$). The high absorption region corresponds to the fundamental absorption associated with optical transitions from the valence band to the conduction band as for their crystalline counterparts. The Urbach region (as it was originally observed by Urbach [7] in AgBr) reflects the structural disorder of all amorphous semiconductors and is characterized by its slope E_u . The Urbach edge arises essentially from the exponentially falling of density of states that extend from the valence band edge towards midgap. However, this region is ideally absent in crystalline semiconductors as sketched in figure 4.5. The width or slope of this region E_u depend on the preparation conditions and vary between 40 meV and more than 100 meV in annealed state and increases under light soaking. The experimental evidence of the Urbach region has been provided by Cody [18] for a-Si:H. In the other hand, it can be calculated with the logarithmic slope as indicated by the dashed line in figure 4.5:

$$E_u \equiv \left(\frac{\partial \ln \alpha(h\nu)}{\partial h\nu} \right)^{-1} \quad (4.16)$$

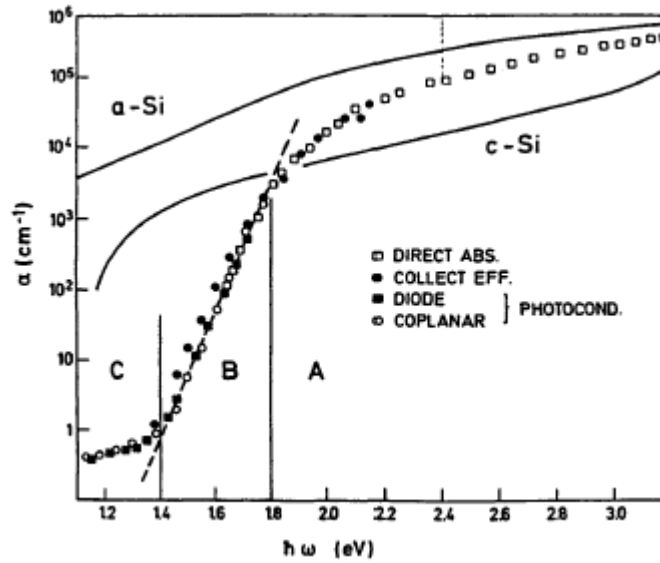


Figure 4.5: Absorption spectra of crystalline silicon (c-Si), amorphous unhydrogenated silicon (a-Si) and hydrogenated amorphous silicon (a-Si:H, data points) [18]

The weak absorption region is related to deep gap-states and originates from Si dangling bonds. The midgap absorption corresponds to the deep defect absorption associated with optical transitions from localized deep states within the bandgap to extended states. These deep defects are of prime interest for characterization of amorphous semiconductor either in initial state (annealed state) or after bandgap illumination (degraded state) since they act as recombination centres and their increase leads to a decrease of both dark and photoconductivity [7, 19, 20]. Although in this region the measurements are made difficult by the limitation on sample thickness, d , to a few microns there are several techniques which are able to overcome this difficulty, especially the constant photocurrent method which is capable of measuring the absorbance A down to values of about 10^{-5} . It is worth noting that there is a direct relation between the deep defect density in a-Si:H and E_u [18].

In its most general form, the optical absorption coefficient $\alpha(\omega)$ where $\omega = 2\pi\nu$ is given by a convolution of occupied $D_{occ}(E)$ and empty $D_{unocc}(E)$ densities of states according to [7, 8]:

$$\alpha(\omega) = \frac{4\pi q^2}{n(\omega) c m_o^2 \epsilon_o} \frac{a^3 P^2(\omega)}{3 \omega} \int_E D_{occ}(E - \hbar\omega) D_{unocc}(E) dE \quad (4.17a)$$

where m_0 and q are the mass and charge of the electron, $c = 2.999 \times 10^8$ m/s, is the velocity of light, $n(\omega)$ is the frequency dependent refractive index, $\epsilon_0 = 8.85 \times 10^{-12}$ A.s/V.m, is the dielectric constant of free space, and a^3 the atomic volume. The factor $P^2(\omega)$ denote the average momentum matrix element squared.

An equivalent expression for $\alpha(\omega)$ is obtained using the average dipole matrix element squared $R^2(\omega)$:

$$\alpha(\omega) = \frac{4\pi q^2}{n(\omega)c\epsilon_0} \frac{a^3}{3} \omega R^2(\omega) \int_E D_{occ}(E - \hbar\omega) D_{unocc}(E) dE \quad (4.17b)$$

There have been theoretical arguments that $P^2(\omega)$ either or $R^2(\omega)$ are approximately constant at least below about 3 eV photon energy if delocalized states are involved [4, 18]. Neglecting the frequency dependence of the refractive index this yields tractable relationships between the absorption coefficient and the densities of states of valence and conduction bands. Replacing by $h\nu$ as is usually done, one obtain in the momentum representation of the transition matrix element:

$$\alpha(h\nu) = \frac{8\pi^2 q^2}{3hc\epsilon_0} \frac{\hbar^2 a^3}{m_0^2 n} \frac{P^2(\omega)}{h\nu} J(h\nu) \quad (4.18a)$$

and in the dipole representation of the transition matrix element:

$$\alpha(h\nu) = \frac{8\pi^2 q^2}{3hc\epsilon_0} \frac{a^3}{n} h\nu R^2(h\nu) J(h\nu) \quad (4.18b)$$

We have abbreviated the convolution of occupied and empty densities of states with $J(h\nu)$.

Note, that the material independent prefactor $\frac{8\pi^2 q^2}{3hc\epsilon_0}$ in equations (4.18a) and (4.18b) is

equal to 0.384. Taking for a^3 the atomic volume of Si in a-Si:H ($a^3 \cong 21.5 \times 10^{-24} \text{ cm}^3$) and an average refractive index $n \approx 4.2$ in the region of the absorption edge we obtain:

$$\alpha(h\nu) \approx C_R h\nu R^2(h\nu) J(h\nu) \quad (4.19a)$$

where C_R has the value $2.0 \times 10^{-24} \text{ cm}^3$. A value of $6.2 \times 10^{-25} \text{ cm}^3$ has been also adopted in. The corresponding expression involving P^2 is:

$$\alpha(h\nu) \approx C_P \frac{P^2(h\nu)}{h\nu} J(h\nu) \quad (4.19b)$$

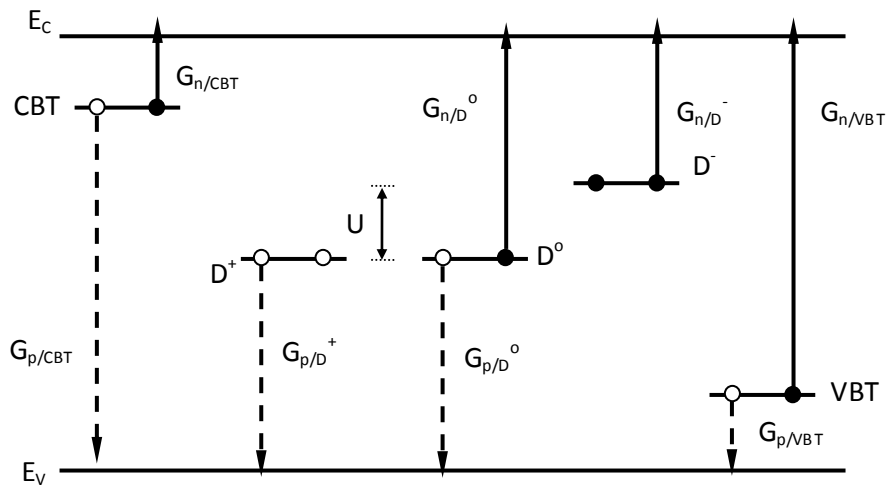
with $C_P = \frac{\hbar^2}{m_o^2} C_R = 1.34 C_R \text{ cm}^4 \text{ s}^{-2}$

The majority of papers dealing with the interpretation of absorption edge data are performed by using equation (4.19b) under the assumption of a constant momentum matrix element [21-24]. In this case:

$$\alpha(h\nu) = \frac{K}{h\nu} J(h\nu) \tag{4.20}$$

Where $K = C_p P_{ave}^2$ and the value of $1.8 \times 10^{-38} \text{ cm}^5 \text{ eV}^2$ is adopted. The value usually taken is, however, $4 \times 10^{-38} \text{ cm}^5 \text{ eV}^2$.

Figure 4.6 shows a schematic representation of the optical transitions under uniform sub-band-gap illumination involved in the CPM simulation.



O: Hole, ●: Electron, - - ➔: Hole transitions, —➔: Electron transitions

Figure 4.6: Carrier transitions involved in the CPM simulation: Optical transitions with the rates $G_{n(p)/T(D)}$ signifying rate of Generation of free electron (hole) from Tail (Defect) states.

The optical generation rates G have the following significance:

- $G_{n(p)/VBT(CBT)}(E)$: Rates of electron (hole) generation from a level E at the valence band tail (conduction band tail).
- $G_{n/D^0(D^-)}(E)$: Rates of electron generation from a $D^0(D^-)$ level E at the defect states distribution.
- $G_{p/D^0(D^+)}(E)$: Rates of hole generation from a $D^0(D^+)$ level E at the defect states distribution.

The optical generation rate is function of the free and trapped carrier densities following the equation:

$$G_{n(p)}(E, h\nu) = \phi \times \left(\frac{K}{h\nu} \right) \times (D_{CB(VB)} - n(p)) \times n_t(D_t)(E) \quad (4.21)$$

where Φ is the incident photon flux and $K=4.34 \times 10^{-38} \text{ cm}^5 \text{ eV}^2$ is a constant proportional to the momentum matrix element. For generation from (into) D^0 , D^- and D^+ states, their respective density must replace $n_t(D_t)$ in equation (4.21). For detail optical generation expressions see appendices B and E.

In our simulation computer program of CPM spectrum all thermal and optical transitions shown on figures 4.4 and 4.6 are included but no transitions between localized levels are taken into account. In addition, we have considered in our analysis two optical transition categories according to Main ac-CPM analysis [25]. Indeed, the electron transitions fall into two categories, the direct optical transitions from occupied states below the Fermi-level to the conduction band, creating free electrons (Fig. 4.7 (a)), and the indirect double transitions where electrons are optically excited from the valence band to unoccupied states above the Fermi-level and from there are thermally emitted to the conduction band (Fig. 4.7 (b)).

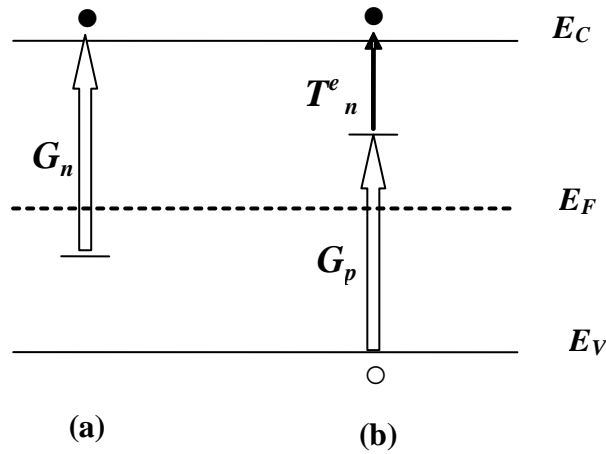


Figure 4.7: Two optical transition categories according to Main ac-CPM analysis [25]:

- (a) Direct transitions creating free electrons (●) with rate $G_n(E, h\nu, \omega)$.
- (b) Indirect double transitions creating free holes (○): an optical transition from the valence band to an empty state at E above E_F , with rate $G_p(E, h\nu, \omega)$, followed by a thermal transition from E to the conduction band with rate $T_n^e(E)$.

4.5. Function occupancy

The occupation function for each level can be derived by setting the time derivative of the rate equations for the discrete localized levels to zero. These occupation functions for the levels have terms from sub-band-gap generation (see below) which is an evident distinction to the occupation functions in the case of band-to-band generation. Actually three step functions U, V and W representing the energy over which sub-band-gap generation affects localized levels have to be used as mentioned in appendix B (cf equations (B.1)-(B.3)). For instance, if $h\nu$ is the energy of the incoming photons only conduction tail states between $E_C - h\nu$ and E_C are considered. As result occupation functions are dependent on photon energy.

4.5.1. Thermal equilibrium

At thermal equilibrium, the occupation functions of tail states (for holes in VBT and for electrons in CBT) are given according to the Fermi-Dirac distribution function:

$$f_{ih}^{cbl}(E) = \frac{1}{1 + \exp\left(\frac{E - E_F}{K_B T}\right)} \quad (4.22)$$

$$f_{th}^{vbt}(E) = 1 - f_{th}^{cbt}(E)$$

The occupation functions for dangling bond states (D^+ , D^o and D^-) with two transition energy levels $E^{o/-}$ and $E^{+/o}$ for transitions $D^{+/o}$ and $D^{o/-}$ respectively are given for each charge state as [16, 17]:

$$f_{th}^+(E) = \frac{1}{1 + 2 \exp\left(\frac{E_F - E}{K_B T}\right) + \exp\left(\frac{2E_F - 2E - U}{K_B T}\right)}$$

$$f_{th}^-(E) = \frac{\exp\left(\frac{2E_F - 2E - U}{K_B T}\right)}{1 + 2 \exp\left(\frac{E_F - E}{K_B T}\right) + \exp\left(\frac{2E_F - 2E - U}{K_B T}\right)} \quad (4.23)$$

$$f_{th}^o(E) = \frac{2 \exp\left(\frac{E_F - E}{K_B T}\right)}{1 + 2 \exp\left(\frac{E_F - E}{K_B T}\right) + \exp\left(\frac{2E_F - 2E - U}{K_B T}\right)} \quad (4.24)$$

As indicate in the above relations, the occupation functions of the tail and the dangling bonds states depend on the position of Fermi level E_F . It can be determined starting from the neutrality equation:

$$n_{th} + \int_{E_V}^{E_C} f_{th}^-(E) D_{db}(E) + \int_{E_V}^{E_C} f_{th}^{cbt}(E) D_{cbt}(E) \quad (4.25)$$

$$- p_{th} - \int_{E_V}^{E_C} f_{th}^+(E) D_{db}(E) - \int_{E_V}^{E_C} f_{th}^{vbt}(E) D_{vbt}(E) + Dop = 0$$

with Dop denote the ionized doping charge density.

4.5.2. Steady state equilibrium

The tail states occupations are described following Hattori et al. [4]. These occupation functions can be deduced from the solution of the rate equations under steady state conditions for a localized tail level “j” which represents an energy E including the individual rate generation. The resulting steady state occupation functions of a tail state are given by:

- Rate equations for trapped carriers n_t et p_t :

$$\frac{dn_t^{dc}(E,t)}{dt} = 0 \Rightarrow$$

$$T_{n/CBT}^t - T_{n/CBT}^e + T_{p/CBT}^e - T_{p/CBT}^t + G_{p/CBT}^{dc} - G_{n/CBT}^{dc} = 0 \quad (4.26a)$$

$$\Rightarrow f_{cbt}^{dc}(E) = \frac{tt_5}{tt_6}$$

$$\frac{dp_i^{dc}(E,t)}{dt} = 0$$

$$T_{p/VBT}^t - T_{p/VBT}^e + T_{n/VBT}^e - T_{n/VBT}^t + G_{n/VBT}^{dc} - G_{p/VBT}^{dc} = 0 \quad (4.26b)$$

$$\Rightarrow f_{vbt}^{dc}(E) = \frac{tt_7}{tt_8}$$

The expressions of the occupation functions $f_{dc}^-(E)$, $f_{dc}^o(E)$ and $f_{dc}^+(E)$ of amphoteric dangling bond states in each charge state D^- , D^o and D^+ can be determined from the solution of the rate equations for the transitions between the defect state and extended states. The resulting steady state occupation functions of a defect state are given by:

- Rate equations for positively and negatively dangling bonds states D^+ and D^- :

$$\frac{dD_{dc}^+(E,t)}{dt} = 0$$

$$T_{n/D^0}^e - T_{n/D^+}^t + T_{p/D^0}^t - T_{p/D^+}^e + G_{n/D^0}^{dc} - G_{p/D^+}^{dc} = 0 \quad (4.27a)$$

$$\Rightarrow f_{dc}^+(E) = \frac{tt_2 \cdot tt_3}{tt_1 \cdot tt_3 + tt_2 \cdot tt_3 + tt_1 \cdot tt_4}$$

$$\frac{dD_{dc}^-(E,t)}{dt} = 0$$

$$T_{n/D^0}^t - T_{n/D^-}^e + T_{p/D^0}^e - T_{p/D^-}^t + G_{p/D^0}^{dc} - G_{n/D^-}^{dc} = 0 \quad (4.27b)$$

$$\Rightarrow f_{dc}^-(E) = \frac{tt_1 \cdot tt_4}{tt_1 \cdot tt_3 + tt_2 \cdot tt_3 + tt_1 \cdot tt_4}$$

and the equation expressing excess dangling bond charge density:

$$D_{dc}^-(E,t) + D_{dc}^o(E,t) + D_{dc}^+(E,t) = 1 \quad (4.28)$$

$$\Rightarrow f_{dc}^o(E) = \frac{tt_1 \cdot tt_3}{tt_1 \cdot tt_3 + tt_2 \cdot tt_3 + tt_1 \cdot tt_4}$$

The thermal transitions $T^{dc}(E)$ and the optical transitions $G^{dc}(h\nu, E)$ for tail and dangling bonds states in dc mode are presented in appendices A and B respectively. The occupation functions are derived by the procedure described above and the expressions of each one are given in appendix C.

4.5.3. Dynamic equilibrium

The diverse occupation functions for single state at energy E for a given energy $h\nu$ at frequency ω are deduced as functions of n_{ac} and p_{ac} using a numerical resolution of the following rate equations after transferring the time variable t to the frequency variable $\omega = 1/t$.

- Rate equations for trapped carriers

$$j\omega\hat{n}_t(E, \omega) = \hat{T}_{n/CBT}^t - \hat{T}_{n/CBT}^e + \hat{T}_{p/CBT}^e - \hat{T}_{p/CBT}^t + \hat{G}_{p/CBT} - \hat{G}_{n/CBT} \quad (4.29a)$$

$$\Rightarrow f_{cvt}^{ac}(E, \omega) = A_{cvt} n_{ac}(\omega) + B_{cvt} p_{ac}(\omega) + C_{cvt}$$

$$j\omega\hat{p}_t(E, \omega) = \hat{T}_{p/VBT}^t - \hat{T}_{p/VBT}^e + \hat{T}_{n/VBT}^e - \hat{T}_{n/VBT}^t + \hat{G}_{n/VBT} - \hat{G}_{p/VBT} \quad (4.29b)$$

$$\Rightarrow f_{vbt}^{ac}(E, \omega) = A_{vbt} n_{ac}(\omega) + B_{vbt} p_{ac}(\omega) + C_{vbt}$$

- Rate equations for positively and negatively dangling bonds states

$$j\omega\hat{D}^+(E, \omega) = \hat{T}_{n/D^0}^e - \hat{T}_{n/D^+}^t + \hat{T}_{p/D^0}^t - \hat{T}_{p/D^+}^e + \hat{G}_{n/D^0} - \hat{G}_{p/D^+} \quad (4.30a)$$

$$\Rightarrow f_{ac}^+(E, \omega) = A_{db}^+ f_{ac}^o(\omega) + B_{db}^+ p_{ac}(\omega) + C_{db}^+ n_{ac}(\omega) + D_{db}^+$$

$$j\omega\hat{D}^-(E, \omega) = \hat{T}_{n/D^0}^t - \hat{T}_{n/D^-}^e + \hat{T}_{p/D^0}^e - \hat{T}_{p/D^-}^t + \hat{G}_{p/D^0} - \hat{G}_{n/D^-} \quad (4.30b)$$

$$\Rightarrow f_{ac}^-(E, \omega) = A_{db}^- f_{ac}^o(\omega) + B_{db}^- p_{ac}(\omega) + C_{db}^- n_{ac}(\omega) + D_{db}^-$$

and the equation expressing zero excess dangling bond charge density:

$$\hat{D}^-(E, \omega) + \hat{D}^0(E, \omega) + \hat{D}^+(E, \omega) = 0 \quad (4.31)$$

$$\Rightarrow f_{ac}^o(E, \omega) = A_{db}^o n_{ac}(\omega) + B_{db}^o p_{ac}(\omega) + C_{db}^o$$

where the hat symbol $\hat{}$ distinguishes the complex notation.

The thermal transitions $\hat{T}(E, \omega)$ and the optical transitions $\hat{G}(h\nu, E, \omega)$ for tail and dangling bonds states in ac mode are given in appendices D and E respectively. The occupation functions are derived by the procedure described above and the expressions of the energy dependent parameters for each one are presented in appendix F.

4.6. Implementation of numerical model

The numerical modeling of CPM spectra applied to the amorphous semiconductors is based on the numerical resolution of the fundamental equations which govern the mechanisms of generation, the processes of transport and the phenomena of recombination of the charge carriers created by monochromatic illumination of energy $h\nu$ lower than the width of the mobility gap. With reference to figure 4.4, 4.6 and 4.7, the rate equations which control the photo-transport under any static (dc) or dynamic (ac) photo-excitation regimes are shown below.

4.6.1 Steady state equilibrium: DC contribution

A sufficient number of energy levels must be taken in order to avoid any distortion in the calculation of the thermal transitions, optical transitions and absorption coefficient. For the steady-state contribution, we obtain the following equations:

- Neutrality equation:

$$n_{dc} + \int_{E_V}^{E_C} D_{dc}^-(E) + \int_{E_V}^{E_C} n_i^{dc}(E) - p - \int_{E_V}^{E_C} D_{dc}^+(E) - \int_{E_V}^{E_C} p_i^{dc}(E) + Dop = 0 \quad (4.32)$$

- Continuity equations for free charges n_{dc} and p_{dc} :

$$\begin{aligned} \frac{dn_{dc}(t)}{dt} = 0 \\ \int_{E_V}^{E_C} (T_{n/CBT}^e + T_{n/VBT}^e - T_{n/CBT}^t - T_{n/VBT}^t) dE + \int_{E_V}^{E_C} (T_{n/D^0}^e + T_{n/D^-}^e - T_{n/D^0}^t - T_{n/D^+}^t) dE \\ + \int_{E_V}^{E_C} G_{n/VBT}^{dc} dE + \int_{E_V}^{E_C} G_{n/CBT}^{dc} dE + \int_{E_V}^{E_C} (G_{n/D^0}^{dc} + G_{n/D^-}^{dc}) dE = 0 \end{aligned} \quad (4.33a)$$

$$\begin{aligned} \frac{dp_{dc}(t)}{dt} = 0 \\ \int_{E_V}^{E_C} (T_{p/CBT}^e + T_{p/VBT}^e - T_{p/CBT}^t - T_{p/VBT}^t) dE + \int_{E_V}^{E_C} (T_{p/D^0}^e + T_{p/D^+}^e - T_{p/D^0}^t - T_{p/D^-}^t) dE \\ + \int_{E_V}^{E_C} G_{p/CBT}^{dc} dE + \int_{E_V}^{E_C} G_{p/VBT}^{dc} dE + \int_{E_V}^{E_C} (G_{p/D^0}^{dc} + G_{p/D^+}^{dc}) dE = 0 \end{aligned} \quad (4.33b)$$

To solve the dc-CPM equations (4.26) to (4.28) and (4.32) to (4.33), we divide the energy gap into N closely spaced energy levels E_i , including the band edges $E_V=E_1$ and $E_C=E_N$, so that the total number of equations to solve for the same number of variable densities (n_{dc} , p_{dc} , n_{ti} , p_{ti} , D_{dc}^+ , D_{dc}^o and D_{dc}^-) is $4N-2$.

In modeling coplanar samples, it is a common practice to assume uniform electric field, perfect ohmic contacts, and to neglect any transport driven by free-carrier diffusion. Under these assumptions, the continuity equation for holes is automatically satisfied when the continuity equation for electrons and the charge neutrality condition are fulfilled. We have developed a computer code to solve the system of equations (4.26) to (4.28) and (4.32) to (4.33) using appropriate numerical techniques. Our simulation of CPM spectra is based on the starting density of states which, for a-Si:H as an example, consists of parabolic bands, exponentially band tails and dangling bond states chosen according to the improved defect pool model [12]. It can be separated into two principal steps. The first step and under dark conditions, determine the position of the Fermi level from the chosen density of states and the charge neutrality requirement, thus defining n_{th} and p_{th} . In the second step and under steady state conditions, the iteration is done in two loops, an inner loop for charge neutrality and the net recombination rate to be equal to the generation rate and an outer loop for adjusting the photon flux of the monochromatic illumination ϕ_{CPM} required to keep the photocurrent on a constant level. The absorption coefficient can be then evaluated according two expressions. The first one which is exactly the relative quantity measured in the CPM experiment, is given by $\alpha_{CPM}^{dc}(h\nu) \propto 1/\phi_{dc}$, while the second expression which represent the absolute total absorption coefficient, is given by $\alpha_{tot}^{dc}(h\nu) = \alpha_n^{dc}(h\nu) + \alpha_p^{dc}(h\nu)$, where $\alpha_n^{dc}(h\nu)$ and $\alpha_p^{dc}(h\nu)$ corresponding to optical transitions associated, respectively, with free electron and free hole creation, and must be taken both into account as both contribute to the absorption processes. They are also related to the total generation rate for electrons $G_n^{dc}(h\nu)$ and for holes $G_p^{dc}(h\nu)$ by $G_n^{dc}(h\nu) = \alpha_n^{dc}(h\nu)\phi_{dc}$ and $G_p^{dc}(h\nu) = \alpha_p^{dc}(h\nu)\phi_{dc}$ respectively. All the thermal and optical transition rates $T^{dc}(E)$ and $G^{dc}(E, h\nu)$ can be deduced from equations (4.14), (4.15) and (4.21) as follow:

$$T_{n(p)}^t(E) = C_{n(p)} n_{dc}(p_{dc}) [D_t(E) - n_t^{dc}(p_t^{dc})] \quad (4.34)$$

$$T_{n(p)}^e(E) = C_{n(p)} D_{CB(VB)} n_t^{dc}(p_t^{dc}) \exp\left(-|E - E_{CB(VB)}| / (k_B T)\right), \quad (4.35)$$

$$G_{n(p)}^{dc}(E, h\nu) = \phi_{dc} \times \left(\frac{K}{h\nu}\right) \times (D_{CB(VB)} - n_{dc}(p_{dc})) \times n_t^{dc}(D_t)(E) \quad (4.36)$$

Their mathematical formulations are given in appendices A and B.

From the simulation we can also evaluate the lifetime as functions of the photon energy by

using the following relations $G_n^{dc}(h\nu) = (n_{dc} - n_{th}) / \tau_n^{dc}(h\nu)$ for electron lifetime and

$G_p^{dc}(h\nu) = (p_{dc} - p_{th}) / \tau_p^{dc}(h\nu)$ for hole lifetime.

4.6.2 Dynamic equilibrium: AC contribution

In the ac-CPM experiment the excitation photon flux $\phi(t)$ is a periodic function of the time having this expression [26, 27]:

$$\phi(t) = \phi_{dc} + \phi_{ac} \exp(j\omega t) \quad (4.37)$$

with ϕ_{dc} being the constant photon flux component and ϕ_{ac} the amplitude of an oscillatory term having the angular frequency ω . In response to the photo-excitation represented by the above equation, two types of contributions has to be considered: the first one represent the continuous part of the excitation giving a dc photocurrent and the second one represent the alternative part of the excitation giving an ac photocurrent. So, basically every time-dependent physical quantities $x(t)$, except the emission rates and the distributions of states, are expected to have the form:

$$x(t) = x_{dc} + x_{ac} \exp(j\omega t) \quad (4.38)$$

In this section, we will focus on special solutions under a sinusoidal excitation light. This is actually the case when the photocurrent measurements are made with chopped excitation light. We treat the case of a small ac signal and contributions from the higher order harmonics are neglected. So, in the case of ac-CPM, the ac-photo-response requires transferring the continuity equations (4.33a) and (4.33b) to the frequency domain using the Fourier integral. The new equations in the frequency domain, after transferring the time variable t to the frequency variable $\omega=1/t$, are:

- Continuity equations for free charges n_{ac} et p_{ac} :

$$j\omega\hat{n}(\omega) = \int_{E_V}^{E_C} \left(\hat{T}_{n/CBT}^e + \hat{T}_{n/VBT}^e - \hat{T}_{n/CBT}^t - \hat{T}_{n/VBT}^t \right) dE + \int_{E_V}^{E_C} \left(\hat{T}_{n/D^0}^e + \hat{T}_{n/D^-}^e - \hat{T}_{n/D^0}^t - \hat{T}_{n/D^+}^t \right) dE \quad (4.39a)$$

$$+ \int_{E_V}^{E_C} \hat{G}_{n/VBT} dE + \int_{E_V}^{E_C} \hat{G}_{n/CBT} dE + \int_{E_V}^{E_C} \left(\hat{G}_{n/D^0} + \hat{G}_{n/D^-} \right) dE$$

$$j\omega\hat{p}(\omega) = \int_{E_V}^{E_C} \left(\hat{T}_{p/CBT}^e + \hat{T}_{p/VBT}^e - \hat{T}_{p/CBT}^t - \hat{T}_{p/VBT}^t \right) dE + \int_{E_V}^{E_C} \left(\hat{T}_{p/D^0}^e + \hat{T}_{p/D^+}^e - \hat{T}_{p/D^0}^t - \hat{T}_{p/D^-}^t \right) dE \quad (4.39b)$$

$$+ \int_{E_V}^{E_C} \hat{G}_{p/CBT} dE + \int_{E_V}^{E_C} \hat{G}_{p/VBT} dE + \int_{E_V}^{E_C} \left(\hat{G}_{p/D^0} + \hat{G}_{p/D^+} \right) dE$$

Since the approximation that the total DOS at any level E is much greater than the occupied DOS at E , particularly in the case of a small ac-signal, the rates T and G in equations (4.14), (4.15) and (4.21) of the thermal and optical transitions are expressed in the frequency domain as:

$$\hat{T}_{n(p)}^t(E, \omega) = C_{n(p)} D_t(E) \hat{n}(\omega) [\hat{p}(\omega)] \quad (4.40)$$

$$\hat{T}_{n(p)}^e(E) = C_{n(p)} D_{CB(VB)} \exp\left(-\left|E - E_{CB(VB)}\right|/(k_B T)\right) \hat{n}_t(E, \omega) [\hat{p}_t(E, \omega)] \quad (4.41)$$

$$\hat{G}_{n(p)}(E, h\nu, \omega) = \phi_{ac} \times \left(\frac{K}{h\nu} \right) D_{CB(VB)} \hat{n}_t(E, \omega) [D_t(E)] \quad (4.42)$$

where the hat symbol ^ distinguishes the complex notation and Φ is the magnitude of the ac photon flux. For more details see appendices D and E.

To solve the ac-CPM equations (4.29) to (4.31) and (4.39), we divide the energy gap into N closely spaced energy levels E_i , including the band edges $E_V=E_1$ and $E_C=E_N$, so that the total number of equations to solve for the same number of variable densities ($\hat{n}, \hat{p}, \hat{n}_{ii}, \hat{p}_{ii}, \hat{D}^0, \hat{D}^+$ and \hat{D}^-) is $4N-2$. By a similar procedure as in steady state, we can calculate all the necessary quantities by solving the ac equations (4.29) to (4.31) and (4.39) except an extra loop concerning frequency change is added to the procedure of simulation. So, the same kind of relations holds for ac absorption spectra just replacing all dc quantities in by the corresponding ac quantities.

As required by the CPM experiment, the photon energy $h\nu$ is varied and the ac photon flux magnitude Φ_{ac} is adjusted to keep the magnitude of the ac-photoconductivity $|q(\mu_n \hat{n} + \mu_p \hat{p})|$

constant over the whole $h\nu$ range. The single transition ac absorption coefficient is then deduced from equation (4.42) as:

$$\alpha_{n(p)}^{ac}(E_i, h\nu, \omega) = \frac{|\hat{G}_{n(p)}(E_i, h\nu, \omega)|}{\phi_{ac}} = \left(\frac{K}{h\nu} \right) D_{CB(VB)} |\hat{n}_i(E_i, \omega)| [D_t(E_i)] \quad (4.43)$$

with \hat{n}_{ii} replaced by $\hat{D}^0, \hat{D}^+, \hat{D}^-$ for transitions from (into) dangling bond defect states, and the total absorption coefficient as:

$$\alpha_{n(p)}^{ac}(h\nu, \omega) = \sum_i \alpha_{n(p)}^{ac}(E_i, h\nu, \omega) \quad (4.44)$$

4.6.3. Deconvolution procedure

Three methods were used until now to get the DOS from a CPM experiment:

1. Pierz et al. [28] take $D(E)$ nevertheless a constant above E_c and $(1 - f(E)) = 1$, then evaluated the density of filled states $D(E-h\nu) f(E-h\nu)$ in a simple way by differentiation of the $\alpha(h\nu)$ spectrum. This is the derivative method;
2. Kocka et al. [29] fit the experimental spectra with a chosen DOS and adjust it to get a good agreement;
3. Jensen [30], however, introduced a correction to the derivate method assuming parabolic energy dependence for $D(E)$ which allows the accurate determination of the DOS.

In this thesis and assuming that the density of unoccupied states (occupied states) at conduction band (valence band) is constant and given by D_c^o (D_v^o). the DOS distribution is calculated from the dc or ac-absorption coefficient, after Pierz at al [28], using the derivative:

$$D(E) = \frac{1}{K D_v^o} \left[\frac{d(h\nu \alpha_{n(p)}^{dc}(h\nu))}{d(h\nu)} \right]_{h\nu=E_c-E} \quad (4.45a)$$

$$D(E) = \frac{1}{K D_v^o} \left[\frac{d(h\nu \alpha_{n(p)}^{ac}(h\nu, \omega))}{d(h\nu)} \right]_{h\nu=E_c-E} \quad (4.45b)$$

References

- [1] M. Vanecek, J. Kocka, A. Poruba, and A. Fejfar, *J. Appl. Phys.*, 78, 6203, 1995.
- [2] Zdenek Remes, Ph.D. thesis, "Study of defects and microstructure of amorphous and microcrystalline silicon thin films and polycrystalline diamond using optical methods", faculty of mathematics and physics, Charles university, Prague, Czech Republic, 1999.
- [3] J. A. Schmidt and F. A. Rubinelli, *J. Appl. Phys.*, 83 (1), 339 (1998).
- [4] F. Siebke, H. Stiebig, A. Abo-Arais and H. Wagner, *Solar Energy Materials and Solar Cells* **41/42** (1996), 529-536.
- [5] R. Platz, R. Brüggemann, G. Bauer and F. R. Germany, *Journal of Non-Crystalline Solids* 164-166 (1993) 355-358.
- [6] K. Hattori, S. Fukuda, K. Nishimura, H. Okamoto, and Y. Hamakawa, *Journal of Non-Crystalline Solids* 164-166 (1993) 351-354.
- [7] A. Mettler, "Determination of the deep defect density in amorphous hydrogenated silicon by the constant photocurrent method: A critical verification", Ph.D. thesis, faculty of sciences, university of Neuchatel, Switzerland (1994).
- [8] R. A. Street, "Hydrogenated amorphous silicon", Cambridge university press, 1991.
- [9] M. Stutzmann, W. B. Jackson and C. C. Tsai, *Physical Review B*, Vol. 32, No.1, pp. 23-47, July 1985.
- [10] K. Winer, *Physical Review Letters*, Vol. 63, No.14, October 1989.
- [11] M. J. Powell and S. C. Deane, *Phys. Rev. B* 48, 10815 (1993).
- [12] M. J. Powell and S. C. Deane, *Phys. Rev. B* 53, 10121 (1996).
- [13] J. Schmal, *Journal of Non-Crystalline Solids* 198-200 (1996) 387-390.
- [14] F. Siebke, H. Stiebig, *Journal of Non-Crystalline Solids* 198-200 (1996) 351-354.
- [15] F. Siebke, H. Stiebig, and R. Carius, *Solar Energy Materials and Solar Cells* **49** (1997) 7-12.
- [16] W. Gao, "Computer modelling and experimental characterisation of amorphous semiconductor thin films and devices", PhD thesis, University of Abertay Dundee, UK, 1995.
- [17] A. Merazga, "Steady state and transient photoconductivity in n-type a-Si", Ph.D.thesis, University of Abertay Dundee, Institute of Technology, Dundee, UK, 1990.
- [18] T. Searle, "Properties of Amorphous Silicon and its Alloys", Edited by University of Sheffield, UK, 1998.

- [19] M. F. Thorpe and L. Tichy, "Properties and Applications of Amorphous Materials", Proceedings of NATO Advanced Study Institute, Czech Republic, 25 June-7 July 2000.
- [20] A. Treatise, "Semiconductors and Semimetals", Volume 21, Part C, Academic Press Inc., Orlando, Florida, USA, 1984.
- [21] I. Sakata, M. Yamanaka, S. Numase, and Y. Hayashi, J. Appl. Phys. 71 (9), 4344-4353 (1992).
- [22] A. Poruba and F. Schauer, Proceeding of the 8-th Inter. School on Con. Matter Phys., Varna, Bulgaria, 19-23 September 1994.
- [23] R. Maudre, M. Maudre, S. Vignoli, P. Roca I Cabarrocas, Y. Bouizem and M. L. Theye, Philos. Mag. B, **67**(4) (1993)497-511.
- [24] A. O. Kodolbaş, and Ö. Öktü, Optical Materials 20 (2002) 147-151.
- [25] C. Main, S. Reynolds, I. Zrinscak and A. Merazga, Journal of Materials Science- Materials in Electronics, 2003.
- [26] H. Okamoto, H. Kida, T. Kamada, and Y. Hamakawa, Philosophical Magazine B, Vol. 52, No.6, pp. 1115-1133, 1985.
- [27] C. Longeaud and J. P. Kleider, Physical Review B, Vol. 48, No.12, pp. 8715-8741, September 1993-II.
- [28] K. Pierz, B. Hilgenberg, H. Mell and G. Weiser, Journal of Non-Crystalline Solids 97-98 (1987) 63-66.
- [29] J. Kocka, M. Vanecek and F. Schauer, Journal of Non-Crystalline Solids 97-98, 715 (1987).
- [30] P. Jensen, Solid State Communications. Vol. 76, No. 11, pp. 1301-1303, 1990.

CHAPTER 5

CONSTANT PHOTOCURRENT TECHNIQUE: RESULTS AND DISCUSSION

5.1. Introduction

Sub-band gap absorption coefficient of amorphous semiconductors can provide useful information on their electronic transport and optical properties. It can be used to infer the spectral distribution of the density of gap states *DOS* of these materials. Many methods have been applied in order to determine *DOS* but the sensitivity of each technique is not the same in the different regions of the band gap. The most extensive are the photo deflection spectroscopy (*PDS*) [1] and constant photocurrent method (*CPM*) [2,3] which evaluate the density of states distribution in the lower half of the band gap and the modulated photocurrent (*MPC*) [4] and time of flight in space charge limited current mode (*TOF-SCLC*) [5] which evaluate it above the Fermi level.

The constant photocurrent method was originally developed for crystalline semiconductors [6] and then applied to amorphous materials [7, 8]. This technique is based on a number of assumptions so its applicability and its validity have often been questioned [9, 10]. Bube et al. [11] noted that to determine the midgap defect densities the *dc-CPM* have to be corrected. Mettler et al. [12] concluded that there is a “working point” at which the basic *CPM* conditions are fulfilled. Zhang et al. [13] found that an inhomogeneous spatial distribution of defects have a strong influence on the *CPM* determined defect density. Schmidt et al. [14] reported that the absorption coefficient measured with *dc-CPM* is dependent on the constant photocurrent chosen to perform the measurement. The constant photocurrent method can be

also performed in the *ac* mode where the sub-band-gap excitation light is chopped at different frequencies. Nevertheless, discrepancies between the *dc* and *ac* modes have been observed and studied by several authors. Conte et al. [15] reported the discrepancy between measurements by *dc* and *ac-CPM* and also observed experimentally the dependence of the *dc-CPM* spectra on the magnitude of the adopted constant photocurrent. Sládek and Thèye [16] found that the difference between *dc* and *ac* measurements results by the fact that the response time of the photocurrent is too slow and decreases with photon energy at room temperature since the difference disappear at low temperatures. Hasegawa et al. [17] found this difference and concluded that the response time increase for low value of $h\nu$. Main et al. [18] in recent work explained this discrepancies in terms of the relative contribution of phonon assisted transitions in the generation process. Following these different interpretations, one can conclude that the subject is still open to discussion and needs more explanations.

Our goal in this chapter is to obtain the curves of absorption coefficient by means of *dc-CPM* and *ac-CPM* of a series of samples including hydrogenated amorphous silicon, micro crystalline silicon and gallium arsenide. Then calculate the density of states distribution within the gap mobility starting from these curves. This is essentials and very significant because the distribution, the density and the nature of these states were not elucidated exactly, there are still contradictions in their interpretations. This thesis can thus more or less help to understand the nature of these states and to predict the properties of these materials.

5.2. Experimental procedure

All measurements in this thesis were carried out at the University Of Abertay Dundee UK. All the experimental investigations described in this work were performed using a coplanar gap cell configuration as illustrated in figure 5.1. The coplanar structure was obtained using a copper mask with two adjacent windows separated by a wire defining the gap.

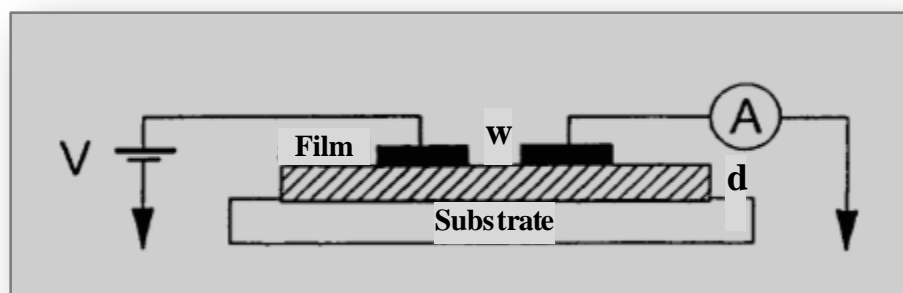


Figure 5.1: Coplanar gap cell configuration for all films used in this work

The undoped sample “Intersolar *ISB4*” of thickness 1.7 μm was prepared at Intersolar UK by *PECVD* technique in an industrial reactor (95% Silane gas SiH_4 / 5% Hydrogen dilution: H_2 , chamber pressure 0.5 Torr, temperature of the substrate 200°C) with Chromium T-shape contacts to form a gap cell 5 mm in length with a separation of 1 mm.

The “*P272*” sample was prepared at the University of Dundee by *PECVD* technique and doped by adding 3vppm of phosphine (PH_3) gas into the deposition gas SiH_4 . Coplanar Chromium electrodes of 0.4mm gap width and 10 mm length were deposited on top of the film of 1 μm thickness.

Microcrystalline silicon film 00c354 of thickness $d=0.42 \mu\text{m}$ was prepared at Forschungszentrum Jülich Germany. 00c354 film was deposited on Corning glass in a *VHF PECVD* system operating at 95 MHz, with a substrate temperature of 185 °C, chamber pressure of 0.3 Torr, *RF* power of 5 W and gas flow ratio r equal to 3% (r represent the silane concentration: silane to hydrogen gas flow ratio $[\text{SiH}_4] / [\text{SiH}_4 + \text{H}_2]$). Electrical contacts of length 1 cm and separation 0.05 cm were deposited to form a gap cell.

For these three samples, the substrate was a Dow-Corning 7059 glass slide and the electrodes are fabricated to be ohmic, i.e., their effect in the circuit can be represented by a negligibly small series resistance. The ohmic nature of the contacts to the samples studied in this work was checked by making current/voltage measurements [19].

The *GaAs:Cr* 1713 sample was prepared at Ruđer Bošković Institute Division of Materials Physics, Zagreb, Croatia. The 1713 sample was part of a semi-insulating *GaAs* chromium doped wafer (*GaAs:Cr*) of 400 μm thickness. It was cut from the ingots grown in the $\langle 100 \rangle$ direction by the liquid encapsulated Czochralski (*LEC*) method under B_2O_3 encapsulation. The chromium concentration was $1.5 \times 10^{16} \text{cm}^{-3}$. Arrays of coplanar ohmic electrodes were deposited on the polished surface of the wafers with a gap of 0.8 mm between electrodes. Single chips of $4 \times 9 \text{mm}^2$ in area were cut from the wafers and mounted in the sample holders of cryostats.

A silver “dag” conductive paint and a fine aluminium wire served to connect the sample to the external circuit. The density of excess carriers is made approximately uniform throughout the depth of the sample so that the current is controlled by bulk rather than surface states. Absolute spectra *CPM* were obtained according to the procedures described by Vanecek et al [2] and were calibrated with reference to measurements of the optical transmission by using

the formula of Ritter-Weiser [20]. The density of states was obtained by applying the derivative method of Pierz et al. for each curve of absorption [21].

The details of the samples are summarized in Table 5.1, together with some of their characteristic parameters. These parameters are given as a rough guide and are known to vary as the history of the material unfolds. The deposition temperature was only available for certain samples although the deposition temperatures were known to be 300°C for all the samples.

Sample	Inte rsolar ISB4 (a-Si :H)	P272 (a-Si :H)	00c354 (μ c-Si :H)	GaAs :Cr 1713
Length l (mm)	5	10	10	4
Gap width w (mm)	1	0.4	0.5	0.8
Thickness d (μ m)	1.7	1.0	0.42	400
Doping level		PH ₃ concentration 3vppm		chromium concentration $1.5 \times 10^{16} \text{cm}^{-3}$
Dark Fermi level position $E_C - E_F$ (eV)	0.67	0.45	0.58	0.71
Room temperature currents (A)	0.46×10^{-9}	26.5×10^{-6}	0.3×10^{-6}	45×10^{-6}
Deposition te mperature ($^{\circ}$ C)	200	295	185	
Plasma pressure (Torr)	0.5	0.1	0.3	
RF power		8 W (40MHz)	5 W (95MHz)	
Deposition technique	PECVD	PECVD	VHF- PECVD	Liquid Encapsulated Czochralski (LEC)

Table 5.1: Sample characteristics that are used for this investigation

5.3. Dark conductivity and activation energy measurements

Two coplanar Chromium electrodes were deposited on the layers on Corning glass for all electrical measurements. The dark current $I_d (T)$ for electric conduction was measured in vacuum, after annealing at 200°C for at least two hours to make sure that all moisture had evaporated from the films. A voltage V of 400V is applied during the measurement. The dark conductivity σ_d is calculated from:

$$\sigma_d (T) = \frac{w \cdot I_d (T)}{V \cdot l \cdot d} \quad (5.1)$$

in which V is the applied voltage, l the width of the electrodes, w the distance between the electrodes, and d the thickness of the film.

The energy differences between the dark Fermi energy and the conduction band ($E_C - E_F$) so-called the activation energy E_a (or demarcation level) is calculated from the dark conductivity $\sigma_d (T)$ using:

$$\sigma_d (T) = \sigma_o \exp\left(\frac{-E_a}{K_B T}\right) \quad (5.2)$$

Usually value of 150 -200 $\Omega^{-1}\text{cm}^{-1}$ [22] is given to the factor σ_o and this is valid only for hydrogenated amorphous silicon.

Graphically, the activation energy E_a is determined from the slope of the Arrhenius plot of the dark conductivity versus the reciprocal temperature T ($\ln(\sigma_d) = f(1000/T)$).

Figure 5.2 shows the dark conductivity measurements set-up used in this work.

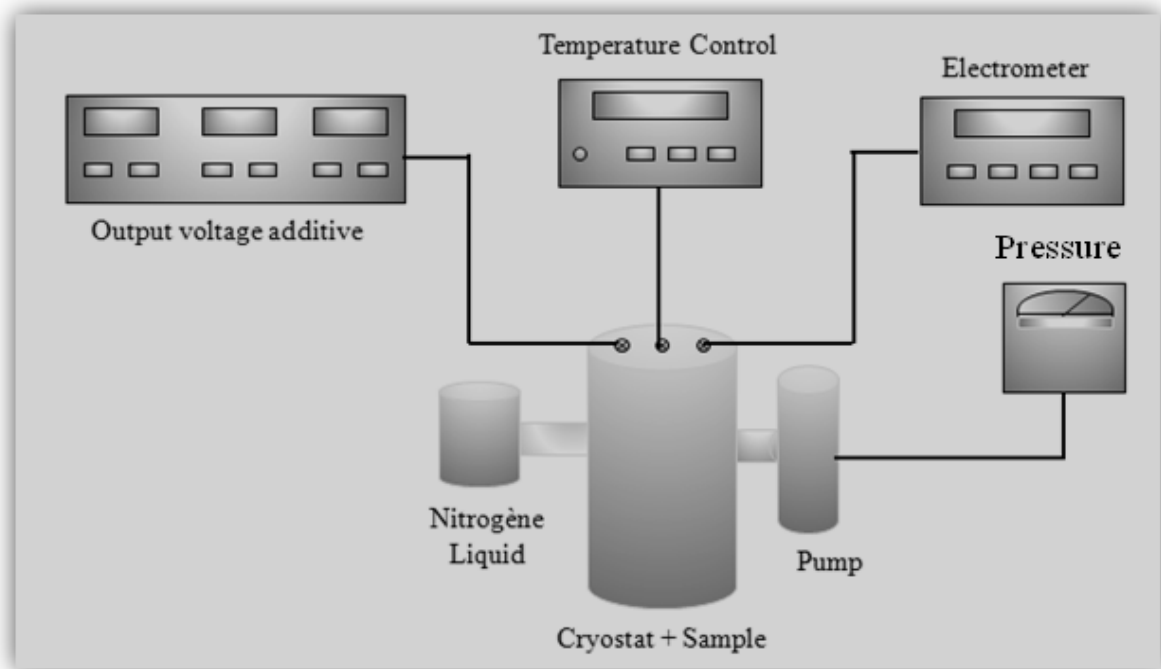


Figure 5.2: Set-up for conductivity measurement versus temperature

Required instruments for this measurement:

- + Cryostat
- + Electrometer (a Keithley 617 electrometer- 1fA sensitivity -)
- + Power supply (an instrument permits the polarization of the sample: range 0-400 V).
- + Temperature control unit (A heater is able to perform electrical measures up to 425 K).
- + Pressure control unit under vacuum conditions (pressure down to $\sim 10^{-3}$ mbar).
- + Nitrogen gas for low temperature

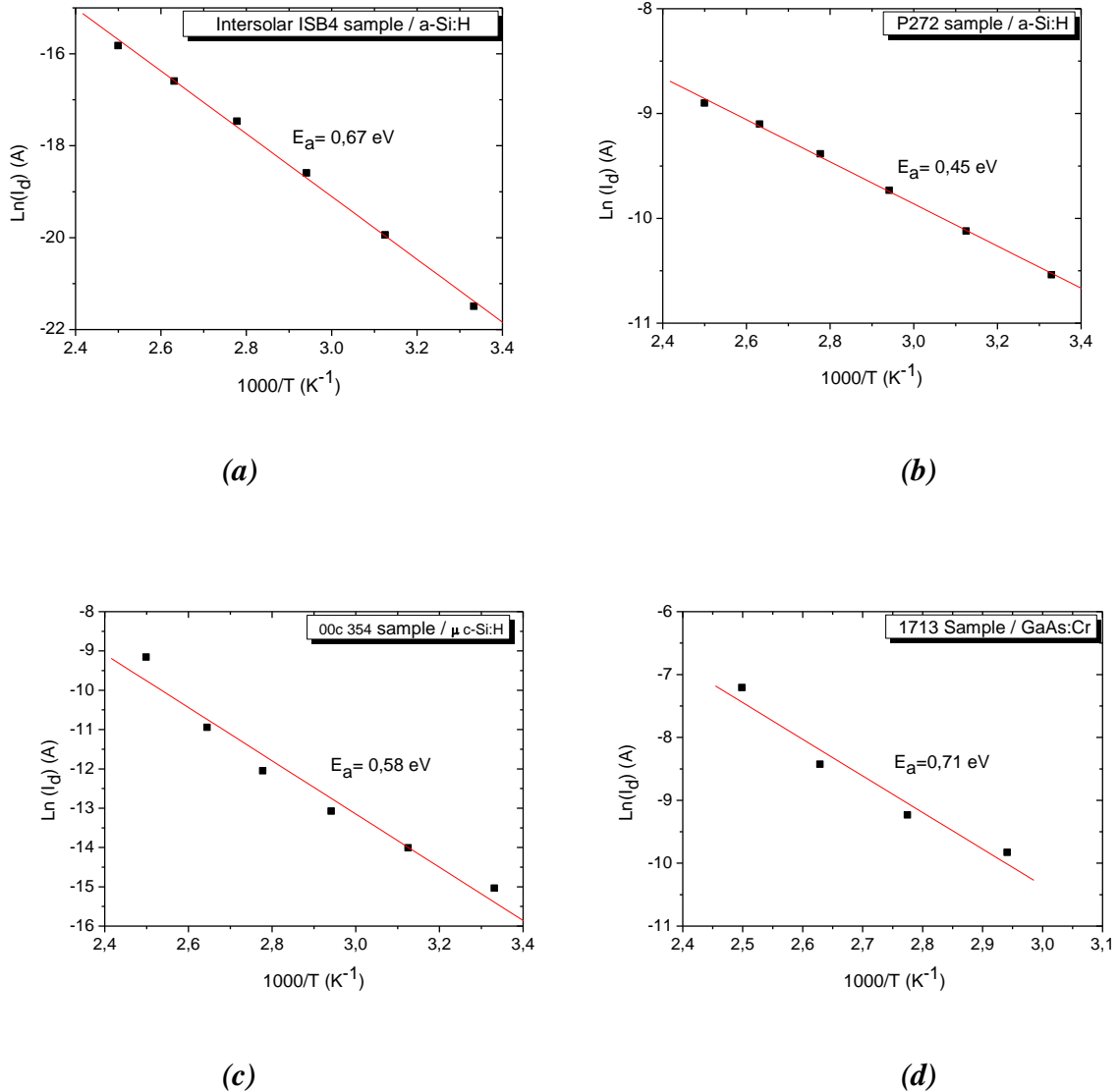
Results

Figure 5.3: Temperature dependence of the dark conductivity for the following samples:

- (a) Intersolar ISB4 (b) P 272
(c) 00c 354 (d) 1713 GaAs:Cr

Figure 5.3 shows the measured dark conductivity as function of inverse temperature for the number of samples studied in this work. As we can see the linear behaviour of the all curves is obtained according to equation (5.2). The activation energies $E_C - E_F$ and thus the Fermi level E_F can be extracted for all samples from an analysis of these $\sigma_d(T)$ data curves using equation (5.2).

We have obtained the following results:

Sample	Activation energy E_a (eV)
<i>Intersolar ISB4</i> (Undoped a-Si:H)	0.67
<i>P 272</i> (n-type a-Si:H)	0.45
<i>00c 354</i> (μ c-Si:H)	0.58
<i>1713</i> (GaAs:Cr)	0.71

5.4. Reflectance -Transmittance measurements

The analysis of the spectral reflectance and transmittance in the wavelength range 1, 2- 3 eV (1035-420 nm) determines the optical parameters and the thickness of the film. The light beam enters the film side of the film / glass structure. The solution of the Fresnel equations for the reflectance and the transmittance of the light beam in this structure as a function of the photon energy, $h\nu$, define the refractive index, $n(h\nu)$, and the extinction coefficient, $k(h\nu)$. The absorption coefficient, α , is determined from k as $4\pi h\nu k/hc$, where h is the Planck constant and c is the speed of light.

The optical absorption coefficient spectrum $\alpha(h\nu)$ can be determined in the absolute scale (cm^{-1}) from:

- The transmittance measurement by a precise matching of the relative CPM spectra in the high absorption region to the $\alpha(h\nu)$ calculated from the absolute transmittance spectra $T(h\nu)$ by using the following formula [2]:

$$\alpha(h\nu).d = \ln \left\{ \frac{R_{123} + \sqrt{R_{123}^2 + 4T^2(1-R_2R_3)^2} \left[R_1R_2 + R_1R_2(1-R_2)^2 \right]}{2T(1-R_2R_3)} \right\} \quad (5.3)$$

Where:

$$R_{123} = (1-R_1)(1-R_2)(1-R_3)$$

R_1 , R_2 and R_3 are the reflectance coefficients of the air-film, film-substrate and substrate-air interfaces respectively.

- The absolute absorbance to transmittance ratio A/T spectra using the Ritter-Weiser formula [20]:

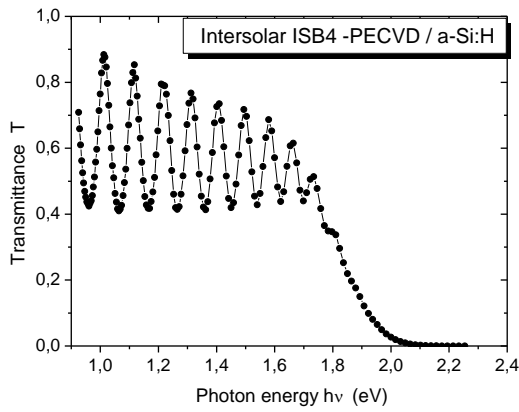
$$\alpha(h\nu).d = \ln \left\{ \frac{1}{2} \left[(1-R_2) \left(1 + \frac{A}{T} \right) + \sqrt{(1-R_2)^2 \left(1 + \frac{A}{T} \right)^2 + 4R_2} \right] \right\} \quad (5.4)$$

The optical band gap, E_g , can be found from the dependence of α on $h\nu$ for the photon energy region where the density of states distribution is significant. The following equation holds in this region.

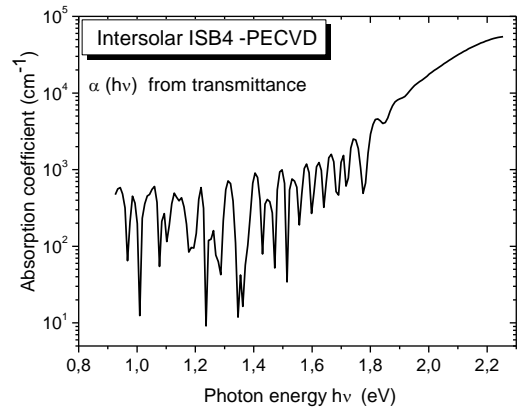
$$\alpha n h \nu = A (h \nu - E_g)^{p+q+1} \quad (5.5)$$

In this equation A is a constant and the parameters p and q are related with the shape of the band edges. Since Tauc [23] reported a linear relation between $\sqrt{\alpha n h \nu}$ and the photon energy $h\nu$, the most usual value for p and q is $1/2$, corresponding to a parabolic shape of the band edges. The band gap obtained solving equation (5.5) with these values is called the Tauc's band gap, E_{Tauc} . Several authors [24, 25] have reported that a linear shape of the band edges has better linearity than a parabolic shape of the band edges. The value for p and q would be then equal to 1 and in this case the band gap obtained solving equation (5.5) is called the cubic band gap. An alternative method to define the optical band gap is the energy (E_x) at which $\alpha(E_x)$ reaches a certain value, 10^x . The band gap $E_{3:5}$ and E_{04} are normally given for $\alpha = 10^{3.5} \text{ cm}^{-1}$ and $\alpha = 10^4 \text{ cm}^{-1}$, respectively. The band gap E_{04} shows values $\sim 0,2$ eV higher than the Tauc band gap. This last convention has the advantage of being independent of the shape of the band edges.

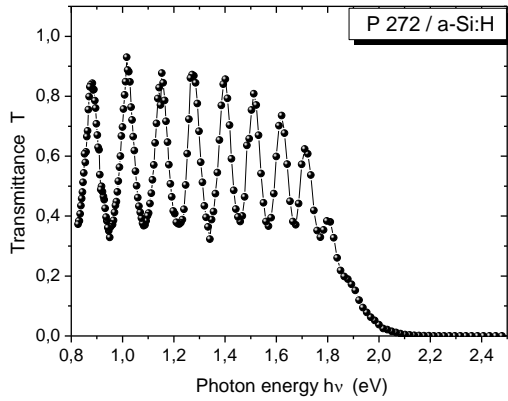
The optical absorption coefficient calculated from transmittance for all samples studied in this thesis are shown below.



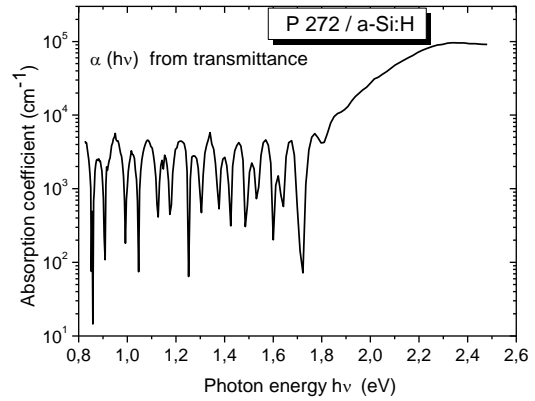
(a)



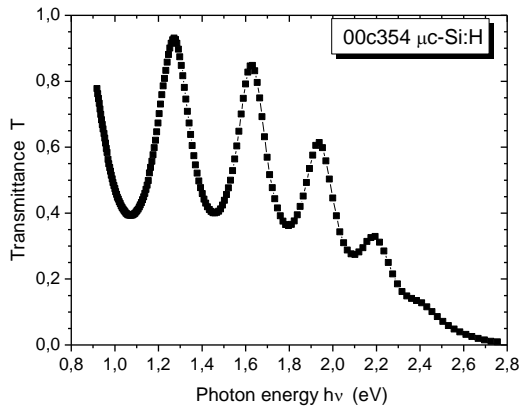
(b)



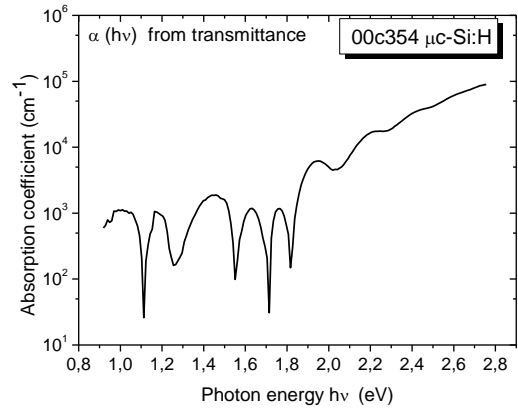
(c)



(d)



(e)



(f)

Figure 5.4: Transmittance and optical absorption coefficient for all samples studied in this thesis

The left graphs of the figure 5.4 show measured transmittance spectrums already set to the absolute scale for all films. Interference fringes are observed in the region of the transparency where the absorptance A is low.

The right graphs of the figure 5.4 show calculated optical absorption coefficient from the absolute transmittance spectrum for all films using equation (5.3). All curves show clearly that, in the range of low energy below the optical gap, the absorption spectrum exhibit interference fringes which roughly coincide with transmittance extremes. A chosen reference energy belongs to the high energy range at which the absorptance is high enough is used to suppress the effect of the interferences. Hence and using the Ritter-Weiser formula, one can get an absolute absorption spectra without influence of interference fringes.

5.5. Optical absorption spectrum measurement: Constant Photocurrent Method

Sub-bandgap absorption was measured with the constant photocurrent method (*CPM*) in order to determine the density of states distribution of *a-Si: H*, $\mu\text{c-Si: H}$ and *GaAs* layers.

The schematic of the *CPM* experiment which have been used in this work is shown in figure 5.5. In the present work, all measurements of the *CPM* spectrum were performed in vacuum at room temperature without changing the position of the sample within the cryostat.

A xenon lamp was used as a light source. A monochromator which had a grating of 600 grooves/mm and a filter wheel were used to obtain monochromatic light with photon energies in the range of 0.8-3.2 eV, to allow absorption measurements deeply into the band-gap. For the lowest photon energy, where the absorption is lowest, the light intensity was chosen such that the photocurrent was equal to a few times the dark current.

For *ac-CPM*, optical chopper was used for measurement at several frequencies (0 – 60 Hz) and lock-in amplifiers to measure ac-photocurrent.

For *dc-CPM*, current was measured by a picoammeter instead of a lock-in amplifier but the light intensity was monitored by the same lock-in method as in the case of *ac-CPM*.

Furthermore and to cause the light induced degradation of our slightly doped *a-Si:H* sample (*P272*), another strong and prolonged illumination has been used (approximately 100mW.cm^{-2} - *AM 1.5*). The following illumination times were selected: 0, 400, 1000 and

4000 sec in order to cover a wide range and reach the saturation point. We took CPM spectrum after each time separately.

In the CPM, absorption coefficients, $\alpha(h\nu)$, are obtained as the inverse of the incident photon number, $1/\phi_{ph}$, under a constant photocurrent, I_{ph} , by using conventional CPM assumptions. The photocurrent at all energies was kept constant by controlling the intensity of the incident light ϕ_{ph} with a computer program. A calibrated photodiode was used to measure the photon flux.

Absolute CPM spectra were obtained by monitoring the transmitted photon flux following the procedures described by Vanecek et al [2]. Data were then calibrated by reference to optical transmission measurements, through the use of the Ritter-Weiser formula [20]. The DOS was obtained by differentiation of the absorption curve method described by Pierz et al [21].

Required instruments for this measurement:

- + Cryostat
- + HT Sample power supply
- + W-halogen lamp
- + Lamp power supply (DC power supply-PSU 35V-10A)
- + Optical chopper
- + Monochromator
- + Filters wheel
- + Beam splitter
- + Detectors (BPX 65)
- + Picoammeter (Keithley 485)
- + Lock-in amplifier

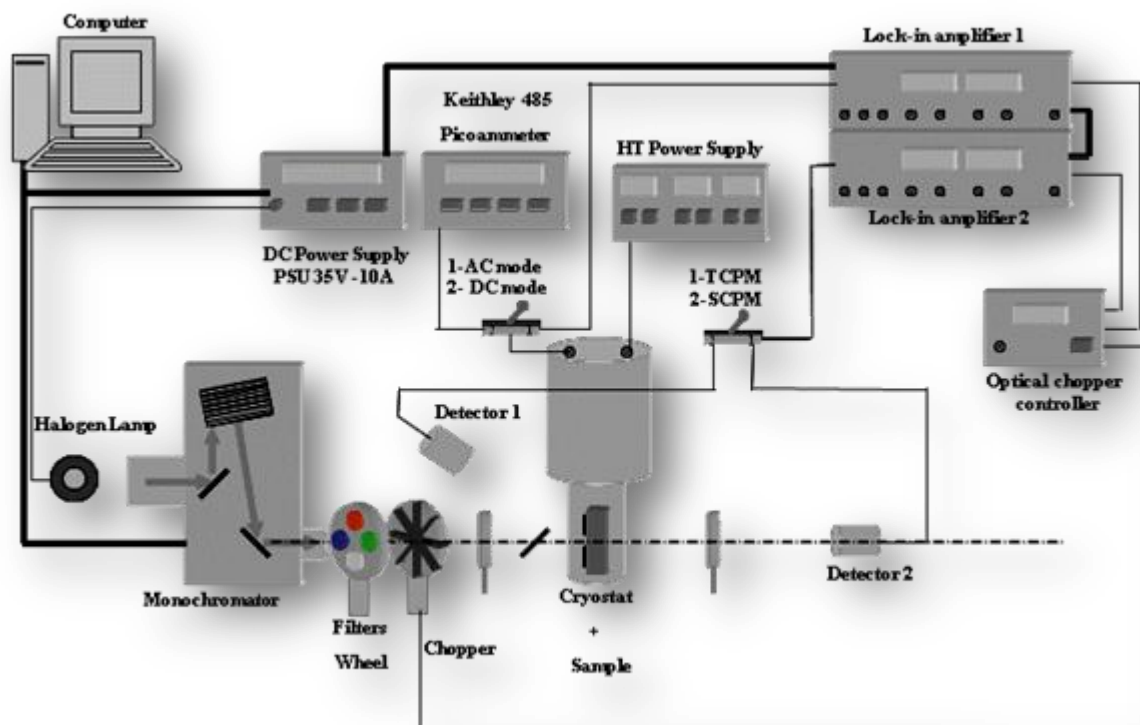
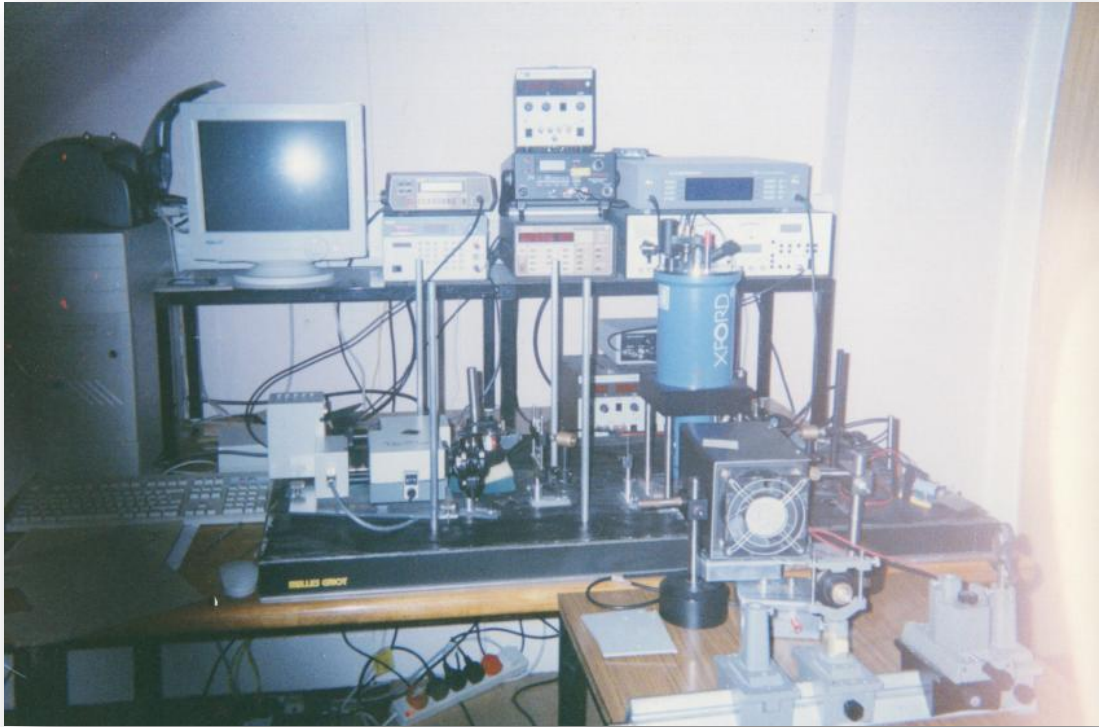


Figure 5.5: Scheme of the DC and AC-CPM setup.



*CPM Experiment at EPICenter laboratory
University of Abertay Dundee, UK.*

5.6. Density of states

Constant photocurrent method spectra can be used to obtain information about the density of localized gap states in a-Si:H, μ c-Si:H and GaAs. In fact, the absorption spectrum reflects all the optical transitions between the electronic gap states. Consequently, this spectrum can be converted into energy distribution of the occupied and empty localized states within the gap by using the equation (4.45) presented in the previous chapter. Hence, four important parameters can be deduced from the analysis of the optical absorption spectrum $\alpha(h\nu)$:

- The Urbach energy, E_U , which characterized the disorder and can be related to the number of weak Si-Si bonds [26];
- The midgap defect density, N_D . There are mainly two methods that are used to get a rapid evaluation of the defect density from CPM measurement. The first one uses the integrated defect absorption, $(\alpha - \alpha_{\text{Urbach}}) dE$, where α_{Urbach} is the contribution from the Urbach tail; the second one uses the value of the absorption coefficient at a single energy, typically at 1.2 eV [27]. It is thus obvious that the defect density can only be correctly determined from a deconvolution procedure;
- The energetic defect distribution within the gap states;
- The charge state of the defect states.

5.7. Results and discussion

In this section we will evaluate simulated and measured CPM spectra of undoped and doped hydrogenated amorphous silicon (a-Si:H), undoped hydrogenated micro-crystalline silicon (μ c-Si:H) and semi-insulating Cr doped gallium arsenide (SI-GaAs: Cr) results.

5.7.1. Hydrogenated amorphous silicon a-Si :H: Undoped sample: Intersolar ISB4

1. Parameters choice

The choice of parameters used in the CPM modelling is taken from literature. The most important parameters used in the case of undoped a-Si:H. are summarized in the following table.

Table 5.2: Density of states parameters used in simulation.

Electron mobility	$\mu_n = 10 \text{ cm}^2 \text{ V}^{-1} \text{ s}^{-1}$
Hole mobility	$\mu_p = 1 \text{ cm}^2 \text{ V}^{-1} \text{ s}^{-1}$
Density of states at the mobility edges E_c, E_v	$G_c = G_v = 1.6 \times 10^{21} \text{ cm}^{-3}$
Mobility gap	$E_g = 1.8 \text{ eV}$
Fermi level position ¹	$E_F = 1.1 \text{ eV}$
Temperature	$T = 300 \text{ K}$
Inverse logarithmic slope for the CBT	$KT_c = 0.025 \text{ eV}$
Inverse logarithmic slope for the VBT	$KT_v = 0.045 \text{ eV}$
Equilibration temperature	$T_{eq} = 500 \text{ K}$
Energy position of the defect pool	$E_{pool} = 1.25 \text{ eV}$
Width of the pool distribution	$\sigma_{pool} = 0.16 \text{ eV}$
Correlation energy	$U = 0.2 \text{ eV}$
Total hydrogen content	$[H] = 5.10^{21} \text{ cm}^{-3}$
Number of hydrogen atoms involved in the breaking of each bond	$i_H = 2$

¹ E_F is calculated from the charge neutrality condition.

Figure 5.6 shows the calculated DOS using these parameters. Defect pool model (DPM) is incorporated in the calculation of the defect states distribution.

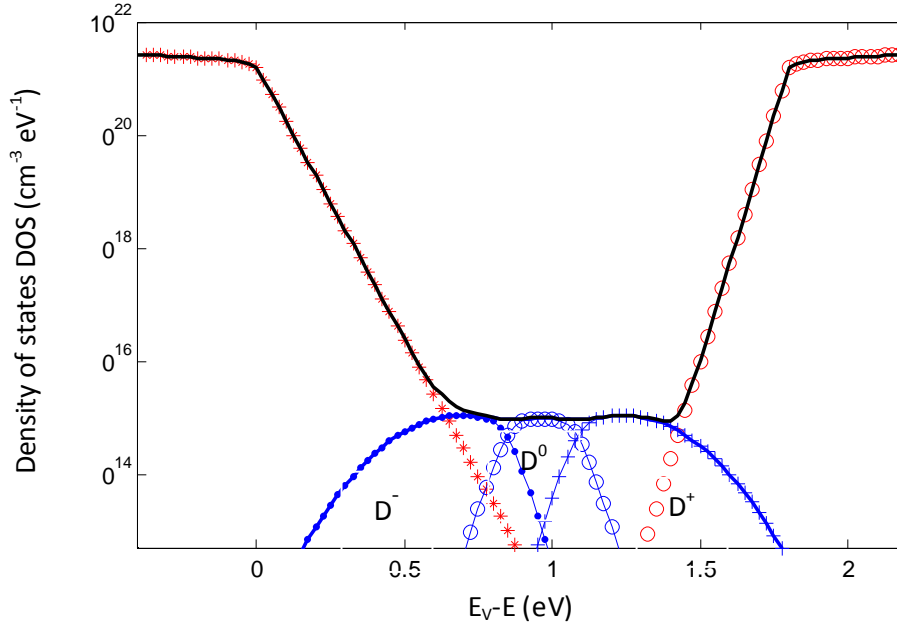


Figure 5.6: Starting density of states distribution for CPM simulation, including parabolic extended bands, exponential band tails and defect states according to DPM.

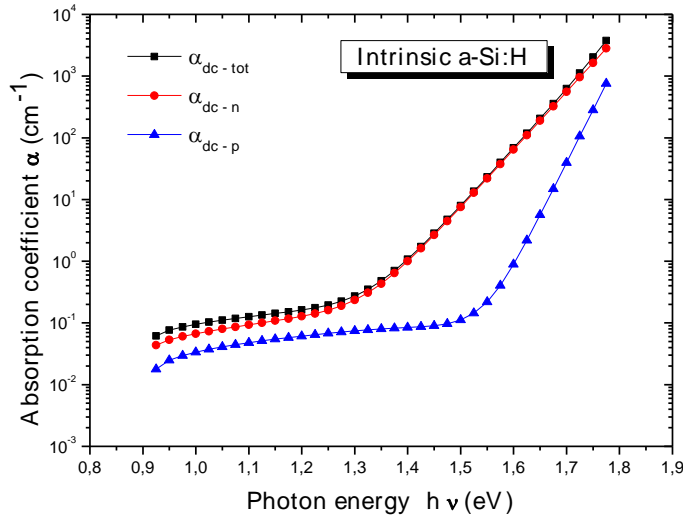
In our computer modelling code, the photocurrent was chosen to be higher than the dark current. In addition, the dark conductivity and photoconductivity as well as the experimental activation energy were reproduced in our simulation.

2. DC and AC comparison

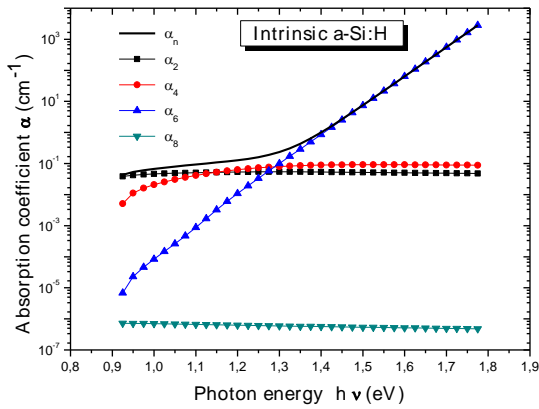
a) Absorption spectra

In figure 5.7.a, we plot the computed absorption spectra α_{dc-tot} and its components, α_{dc-n} and α_{dc-p} corresponding to sub-band gap transitions exciting electrons to the CB and sub-band gap transitions exciting holes to the VB respectively. Our results obviously indicate that there is non-negligible contribution of α_{dc-p} to the total absorption coefficient α_{dc-tot} for photon energies less than 1.3 eV. In order to understand the origin of our results, we plot in figure 5.7.b and figure 5.7.c the coefficients α_{dc-n} and α_{dc-p} , but showing all the individual components corresponding to every possible optical transition taking place between localized

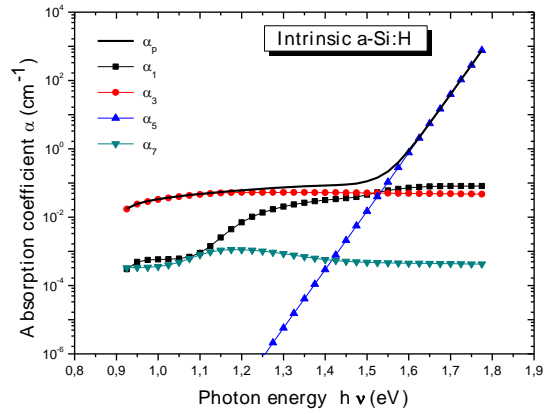
and extended states. Figure 5.7 (a) and figure 5.7(c) show that in undoped a-Si:H, the difference existing between electron and hole mobility value does not prevent the large contribution of the optical process $D^0 \rightarrow VB (\alpha_3)$ to α_{dc-tot} .



(a)



(b)

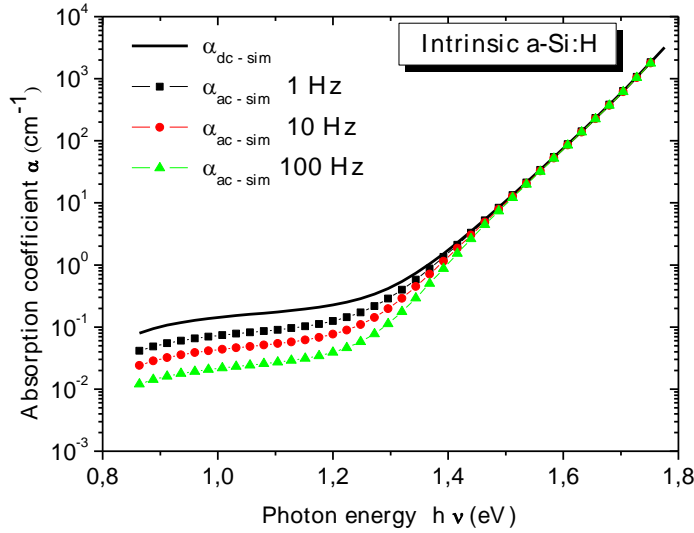


(c)

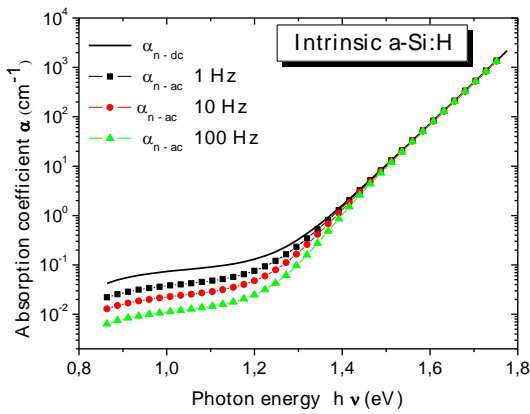
Figure 5.7: (a) Simulated dc-CPM absorption spectrum α_{dc-tot} (\blacktriangle) and its components, α_{dc-n} (\blacksquare) and α_{dc-p} (\bullet)
 (b) Simulated absorption spectrum α_{dc-n} and its individual components.
 (c) Simulated absorption spectrum α_{dc-p} and its individual components.

In fact, for the coefficient α_{dc-n} , we have four possible transitions which can promote electrons to the conduction band (CB). They correspond to electrons leaving from D^0 (α_2), D^- (α_4), VBT (α_6), and CBT (α_8) states. In the same way, for the coefficient α_{dc-p} , there are also four possible transitions which can bring holes to the valence band (VB). They correspond to holes leaving from D^+ (α_1), D^0 (α_3), CBT (α_5), and VBT (α_7) states. For photon energies less than 1.3eV for electron and 1.5eV for holes, a number of processes compete to shape the total absorption coefficient α_{dc-tot} . These processes are $D^0 \rightarrow CB$ (α_2) and $D^- \rightarrow CB$ (α_4) for electrons and $D^+ \rightarrow VB$ (α_1) and $D^0 \rightarrow VB$ (α_3) for holes. For photon energies $h\nu$ greater than 1.3eV for electron and 1.5eV for holes, the wider slope of the valence band tail makes the electron transition VBT \rightarrow CB (α_6) to prevail over the hole transition CBT \rightarrow VB (α_5), and over all the others.

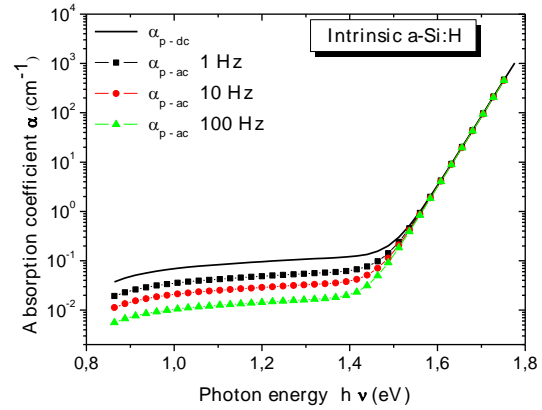
The computed dc and ac absorption coefficient at room temperature and its electron and hole components are plotted in figure 5.8 at various chopping frequencies. All spectra exhibit the well known characteristic shape, i. e. an exponential edge representing the Urbach region from ~ 1.8 eV to ~ 1.4 eV, a plateau from ~ 1.4 eV to ~ 1.1 eV, and a decreasing region which represent the deep defect region at lower energies.



(a)



(b)



(c)

Figure 5.8: Simulated dc-CPM (—) and ac-CPM (■, ● and ▲) absorption spectra at several frequencies (1 Hz, 10 Hz and 100 Hz):

(a) Total absorption coefficient $\alpha_{tot}(h\nu)$ showing a discrepancy in defect region below about 1.35eV and no difference in the Urbach edge region as the frequency increases.

(b) Electron absorption coefficient $\alpha_n(h\nu)$ showing a discrepancy in defect region below about 1.35eV and no difference in the Urbach edge region as the frequency increases.

(c) Hole absorption coefficient $\alpha_p(h\nu)$ showing a discrepancy in defect region below about 1.35eV and no difference in the Urbach edge region as the frequency increases.

For frequencies less than 100Hz, the difference between the dc and ac spectra is clear and observed only below the Urbach edge ($h\nu < 1.35$ eV) as reported by many authors [15,16,

18,28]. This discrepancy can be explained by the fact that the dc-CPM regime includes the direct and indirect transitions, i.e., the transitions from the occupied gap states below E_F to empty conduction band states or unoccupied gap states above E_F followed by a slow thermal emission. The latter are neglected by ac-CPM regime which includes only the transitions from occupied defects below E_F into conduction band states or shallow tail states. The difference is also observed between the different frequencies but only below Urbach edge ($h\nu < 1.35\text{eV}$) and above the entire absorption curve coalesces. It is worth noting that this discrepancy between frequencies is more pronounced between $\alpha_p^{dc}(h\nu)$ and $\alpha_p^{ac}(h\nu)$ spectra for the reason that the holes mobility is chosen less than electrons as listed in table 5.2.

The following figure illustrates the dc-CPM and ac-CPM measured optical coefficient absorption of the intrinsic sample (Intersolar ISB4) performed at two chopper frequencies 5 Hz and 30 Hz. A large discrepancy is detectable in the absorption spectrum of a-Si:H at low photon energies between dc and ac measurements. While dc measurement gives a consistently higher value for the absorption coefficient than ac measurement at defect region no difference exist in the Urbach edge region as the frequency increases. We can conclude from this figure that there is practically a good agreement between the modelling and the experimental results.

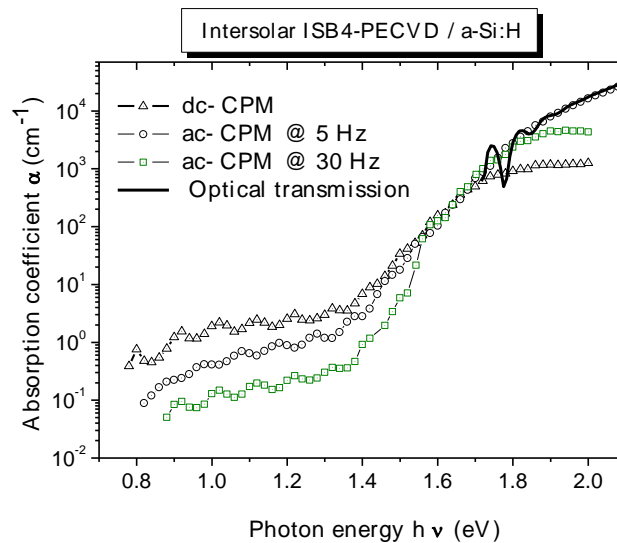


Figure 5.9: Measured dc-CPM (Δ) and ac-CPM (O and \square) absorption spectrum of Intersolar ISB4 sample at two frequencies (5 Hz and 30 Hz), showing a discrepancy in defect region and no difference in the Urbach edge region as the frequency increases. $\alpha(h\nu)$ determined from the transmittance is shown only in the high energy (solid line \blacksquare).

b) Density of states distribution

In the following subsections, the derivative method of Pierz et al. is used to get the density of states distribution from simulated and measured absorption spectra in order to check how well the original DOS is approximated.

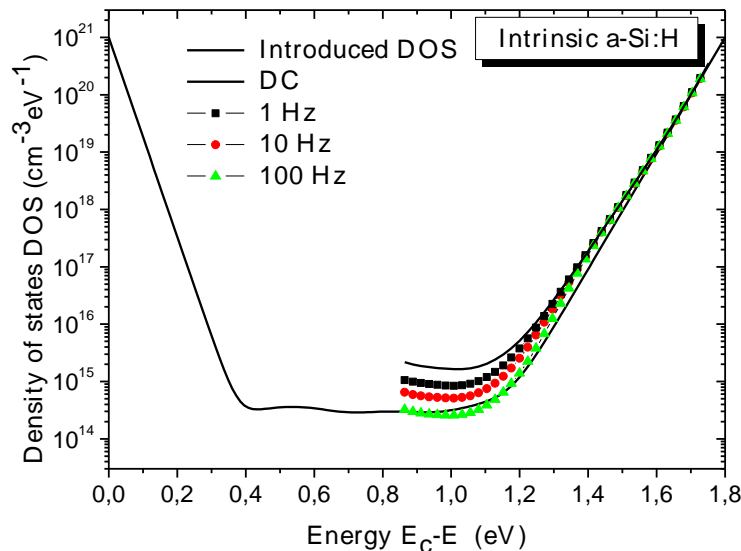


Figure 5.10: Reconstructed DOS from $\alpha_{dc}(h\nu)$ (—) and $\alpha_{ac}(h\nu)$ spectra (■, ● and ▲) with dc-CPM and ac-CPM at three frequencies 1, 10 and 100 Hz respectively, showing a most reliable recovery in the case of the 100 Hz ac-CPM.

Figure 5.10 shows the reconstruction of the starting DOS from the dc and ac total absorption coefficients by using the derivative method. The computed DOS demonstrate that the ac-CPM spectra give a DOS much closer to the introduced DOS than the dc-CPM spectrum. On the other hand, by using higher frequencies the extracted DOS is much and much closer to the starting DOS than by using lower frequencies. Indeed, with $\alpha_{ac}(h\nu)$ at high frequency, we can extract the density of states in the lower half of the gap states below E_F near the valence band edge because this is related to the assumption which is often made in computing the DOS in which only transitions from occupied gap states to extended states in the conduction band contribute to measured photoconductivity. Therefore, the dc-CPM can not be used to derive the true DOS but it can give us the true optical absorption coefficient spectrum since this

regime includes the transition into unoccupied defect states, whereas the ac- CPM at high frequency can be used to derive the true DOS since in this regime some optical transitions are not detected.

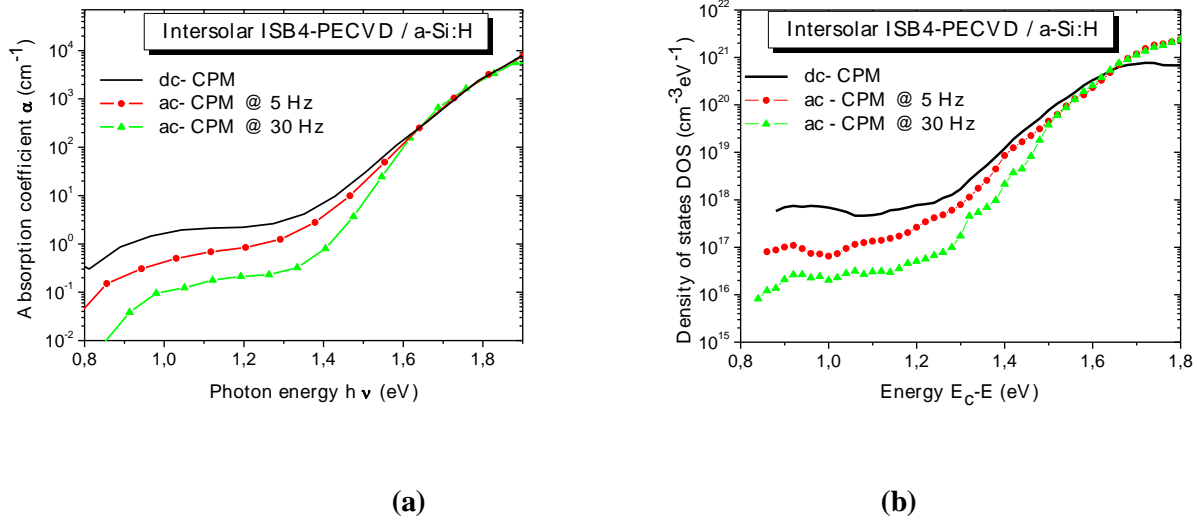


Figure 5.11: (a) Measured dc-CPM (—) and ac-CPM $\alpha(h\nu)$ spectrum at two frequencies, 5Hz and 30Hz (● and ▲) for the Intersolar sample after a suitable fitting operation. (b) Density of states of “Intersolar ISB4 sample” derived from measured $\alpha(h\nu)$ spectra by dc-CPM (—) and ac-CPM at two frequencies 5 and 30 Hz (● and ▲)

Figure 5.11.a shows the measured absorption spectrum of the Intersolar ISB4 – PECVD sample at room temperature free from interference fringes after a suitable fitting operation. This data is used to determine the experimental density of states using the Pierz et al. method (see figure 5.11.b). The CPM-determined density of gap-states distribution within the gap shows a large difference between the two modes. This difference is observed only in the defect region and increases while frequency increases. Each mode and each frequency leads to an appropriate density of state for the same sample.

5.7.2. Hydrogenated amorphous silicon a-Si :H: Doped sample : P272 (n type) :

1. Parameters choice

Table 5.3 summarizes the parameters used in the dc- ac-CPM program code for the case of n-type a-Si:H.

Electron mobility	$\mu_n = 10 \text{ cm}^2 \text{ V}^{-1} \text{ s}^{-1}$
Hole mobility	$\mu_p = 1 \text{ cm}^2 \text{ V}^{-1} \text{ s}^{-1}$
Density of states at the mobility edges E_c, E_v	$G_c = G_v = 1.6 \times 10^{21} \text{ cm}^{-3}$
Mobility gap	$E_g = 1.8 \text{ eV}$
Fermi level position ²	$E_F = 1.25 \text{ eV}$
Temperature	$T = 300^\circ \text{K}$
Inverse logarithmic slope for the CBT	$KT_c = 0.03 \text{ eV}$
Inverse logarithmic slope for the VBT	$KT_v = 0.05 \text{ eV}$
Equilibration temperature	$T_{eq} = 500 \text{ K}$
Energy position of the defect pool	$E_{pool} = 1.27 \text{ eV}$
Width of the pool distribution	$\sigma_{pool} = 0.19 \text{ eV}$
Correlation energy	$U = 0.2 \text{ eV}$
Total hydrogen content	$[H] = 7.10^{21} \text{ cm}^{-3}$
Number of hydrogen atoms involved in the breaking of each bond	$i_H = 2$

Table 5.3: Density of states parameters used in the simulation.

Figure 5.12 shows the calculated DOS using these parameters. Defect pool model is included in the calculation of the defect states distribution.

² E_F is calculated from the charge neutrality condition.

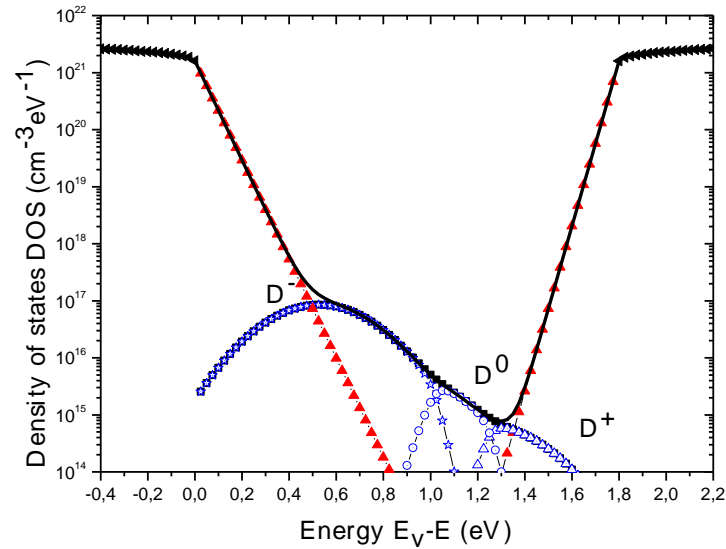


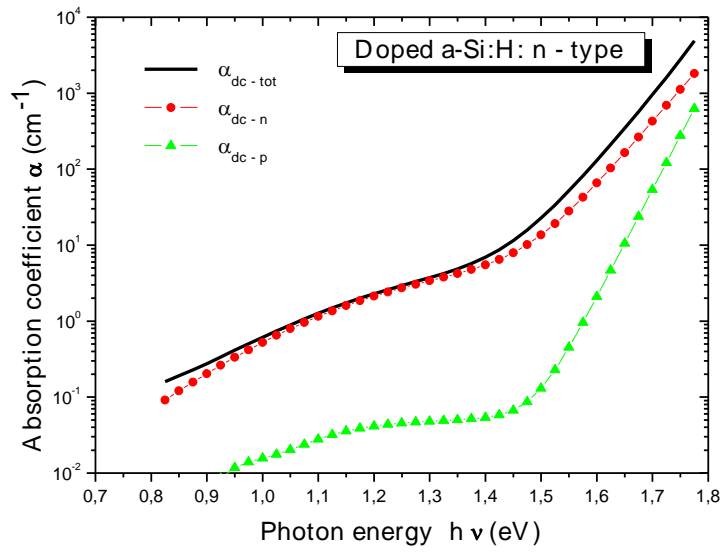
Figure 5.12: Introduced density of states distribution for CPM simulation, including parabolic extended bands, exponential band tails and defect states according to DPM.

2. DC and AC comparison

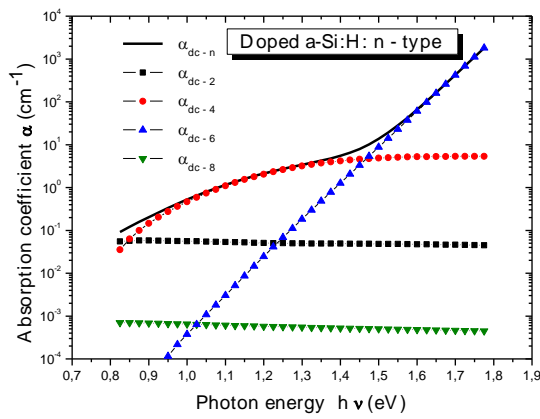
a) Absorption spectra

Our computer code is used also to simulate the absorption coefficient of n-type sample. The result is shown in figure 5.13. As for the undoped sample case, the measured dark conductivity and photoconductivity as well as the activation energy were also reproduced in the simulation. The simulation was carried out with a constant photocurrent larger than the dark current.

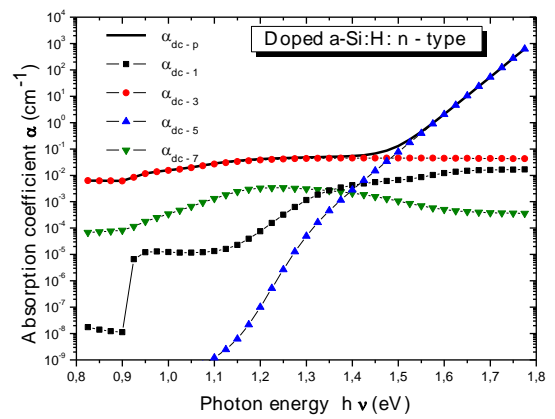
Figure 5.13.a shows the total absorption coefficient α_{dc-tot} with its components α_{dc-n} and α_{dc-p} versus photon energy in dc mode. The first important feature to be observed is that in n-type sample the total coefficient α_{dc-tot} coincides with α_{dc-n} . In fact, the dc total absorption coefficient α_{dc-tot} is entirely shaped by the component α_{dc-n} , and the electrical transport is dedicated by photo generated electrons.



(a)



(b)



(c)

Figure 5.13: (a) Simulated dc-CPM absorption spectrum α_{dc-tot} (\blacktriangle) and its components, α_{dc-n} (\blacksquare) and α_{dc-p} (\bullet)

(b) Simulated absorption spectrum α_{dc-n} and its individual components.

(c) Simulated absorption spectrum α_{dc-p} and its individual components.

Figure 5.13.b and 5.13.c show the contributions of the most important optical processes to the simulated total coefficient. We can see that in doped sample, the Urbach region of α_{dc-tot} is also shaped by the transitions $VBT \rightarrow CB$ (α_6), however in the region associated with midgap states, α_{dc-tot} is governed in the n-type sample by the transitions $D^- \rightarrow CB$ (α_4). The reason that the absorption spectra is governed by the process $D^- \rightarrow CB$ (α_4) at low photon energies can be understood by looking to the profile of the DOS resulting from the defect pool model as depicted by figure 5.10. This latter, shows that the density of D^- states grows by several orders of magnitude with regard to their equivalent in undoped a-Si:H.

Figure 5.14 shows the optical absorption coefficient of the slightly P-doped amorphous silicon coplanar sample as measured with the CPM technique in the dc and ac mode at chopper frequency 30 Hz together with the absorption coefficient calculated from the transmittance. As we can see in this figure no significant difference between the dc and ac optical excitation conditions. These experimental results confirm the simulated results found before.

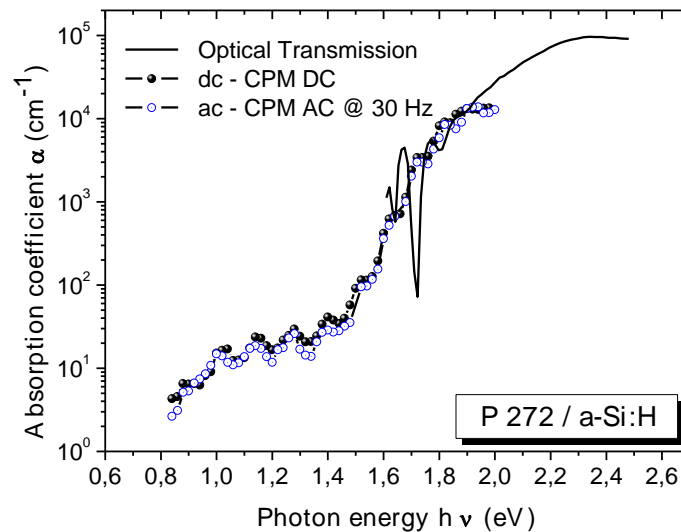


Figure 5.14: Measured dc-CPM and ac-CPM $\alpha(h\nu)$ spectrum at 30Hz frequency for the P272 sample. $\alpha(h\nu)$ determined from the transmittance is shown only in the high energy (solid line).

b) Density of states distribution

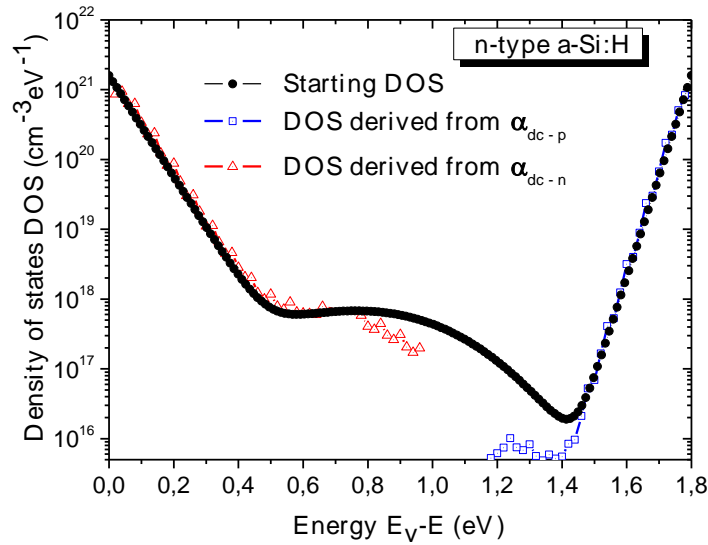
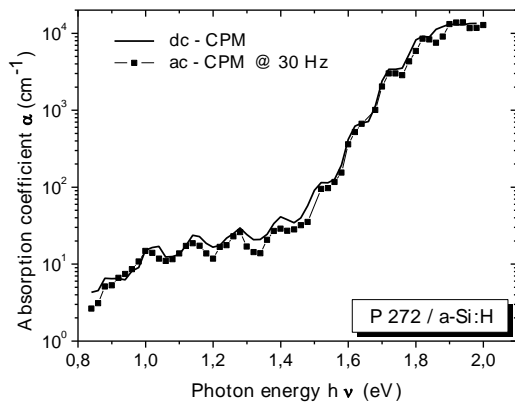
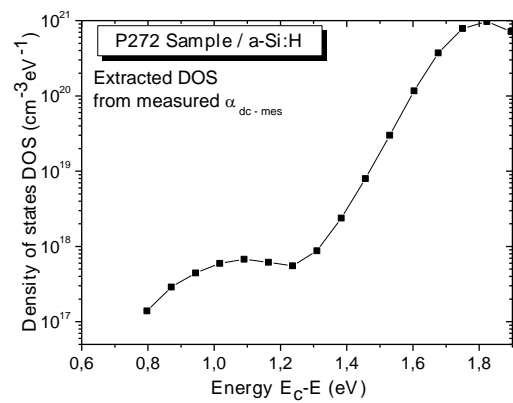


Figure 5.15: Density of states extracted from the simulated $\alpha_n(h\nu)$ and $\alpha_p(h\nu)$ absorption coefficients of figure 5.13.a

Figure 5.15 shows the densities of states distribution derived from simulation of the dc -CPM spectra of figure 5.13.a.



(a)



(b)

Figure 5.16: (a) Measured dc-CPM and ac-CPM $\alpha(h\nu)$ spectrum at 30Hz frequency for the P272 sample.

(b) Reconstructed DOS from $\alpha_{dc}(h\nu)$ spectrum of figure 5.16.a

Figure 5.16.a shows the measured dc absorption coefficient and the ac absorption coefficient at chopper frequency 30 Hz. Figure 5.16.b illustrates the densities of occupied states close to valence band edge derived from the measured dc - CPM spectrum of figure 5.16.a.

5.7.3. Hydrogenated micro-crystalline silicon $\mu\text{c-Si:H}$: 00c354 sample

1. Parameters choice

In Chapter 2, a brief review of electronic states located in the band gap of $\mu\text{c-Si:H}$ determined by different experimental techniques methods was presented. However, all these experiments have some restrictions and consequently provide information only in a limited range. The aim of this section is to combine these information with ones derived from the dc and ac CPM experiment to draw a schematic picture of the density of states of highly crystalline $\mu\text{c-Si:H}$ in energetic sense and also to compare the two modes.

We use the ac-CPM to measure the ac- $\alpha(\text{h}\nu)$ in VHF-PECVD-prepared $\mu\text{c-Si:H}$ and apply the derivative method of Pierz et al [21] to convert the measured data into a DOS distribution in the lower part of the energy-gap. We complete the $\mu\text{c-Si:H}$ DOS model, in the upper part of the energy-gap, by previous DOS data based on transient photocurrent (TPC) spectroscopy (Figure 2) [29] and, around the mid-gap, by a-Si:H-like dangling bond defect DOS with appropriate parameters from literature. On the basis of the complete DOS model, we have developed numerical simulations of the ac-CPM by including both carrier types in the absorption and transport processes. We compute the components ac- $\alpha_n(\text{h}\nu)$ and ac- $\alpha_p(\text{h}\nu)$, of the total ac- $\alpha(\text{h}\nu)$, corresponding to electron transitions, respectively from filled states in the lower energy range to the conduction band (free electron creation) and from the valence band to empty states in the upper energy range (free hole creation). We then use the derivative method of Pierz et al to reconstruct from each component the corresponding DOS distribution. The most important parameters of the $\mu\text{c-Si:H}$ DOS model are shown in table 5.4 below.

Table 5.4: Density of states parameters used in modelling of the optical absorption spectrum for undoped $\mu\text{-Si:H}$.

Electron mobility	$\mu_n = 1 \text{ cm}^2 \text{ V}^{-1} \text{ s}^{-1}$
Hole mobility	$\mu_p = 0.1 \text{ cm}^2 \text{ V}^{-1} \text{ s}^{-1}$
Density of states at the mobility edges E_c, E_v	$G_c = G_v = 1.5 \times 10^{20} \text{ cm}^{-3} \text{ eV}^{-1}$
Mobility gap	$E_g = 1.2 \text{ eV}$
Temperature	$T = 300^\circ\text{K}$
Inverse logarithmic slope for the CBT	$KT_c = 0.03 \text{ eV}$
Inverse logarithmic slope for the VBT	$KT_v = 0.063 \text{ eV}$
Total defect density	$N_{DB} = 1.5 \times 10^{14} \text{ cm}^{-3}$
Width of the dangling bonds distribution	$\sigma = 0.15 \text{ eV}$
Correlation energy	$U = 0.2 \text{ eV}$

The following figure show the computed density of states distribution by means of CPM computer code using the parameters listed in table 5.4.

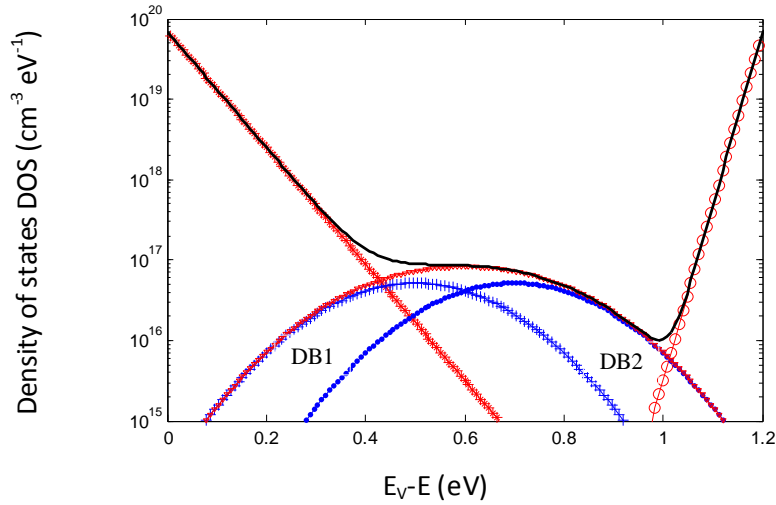


Figure 5.17: $\mu\text{-Si:H}$ DOS model used in dc- and ac-CPM simulation.

2. DC versus AC mode

c) Absorption spectra

Figure 5.18.a shows the computed absorption coefficient in dc mode $dc-\alpha_{tot}(h\nu)$ and its dc components $dc-\alpha_n(h\nu)$ and $dc-\alpha_p(h\nu)$ using the DOS which is depicted in the figure 5.17.

Since undoped $\mu\text{c-Si:H}$ shows n-type behaviour and $\mu_n > \mu_p$, electrons absorption coefficient is greater than holes absorption coefficient except in the lower photon energy.

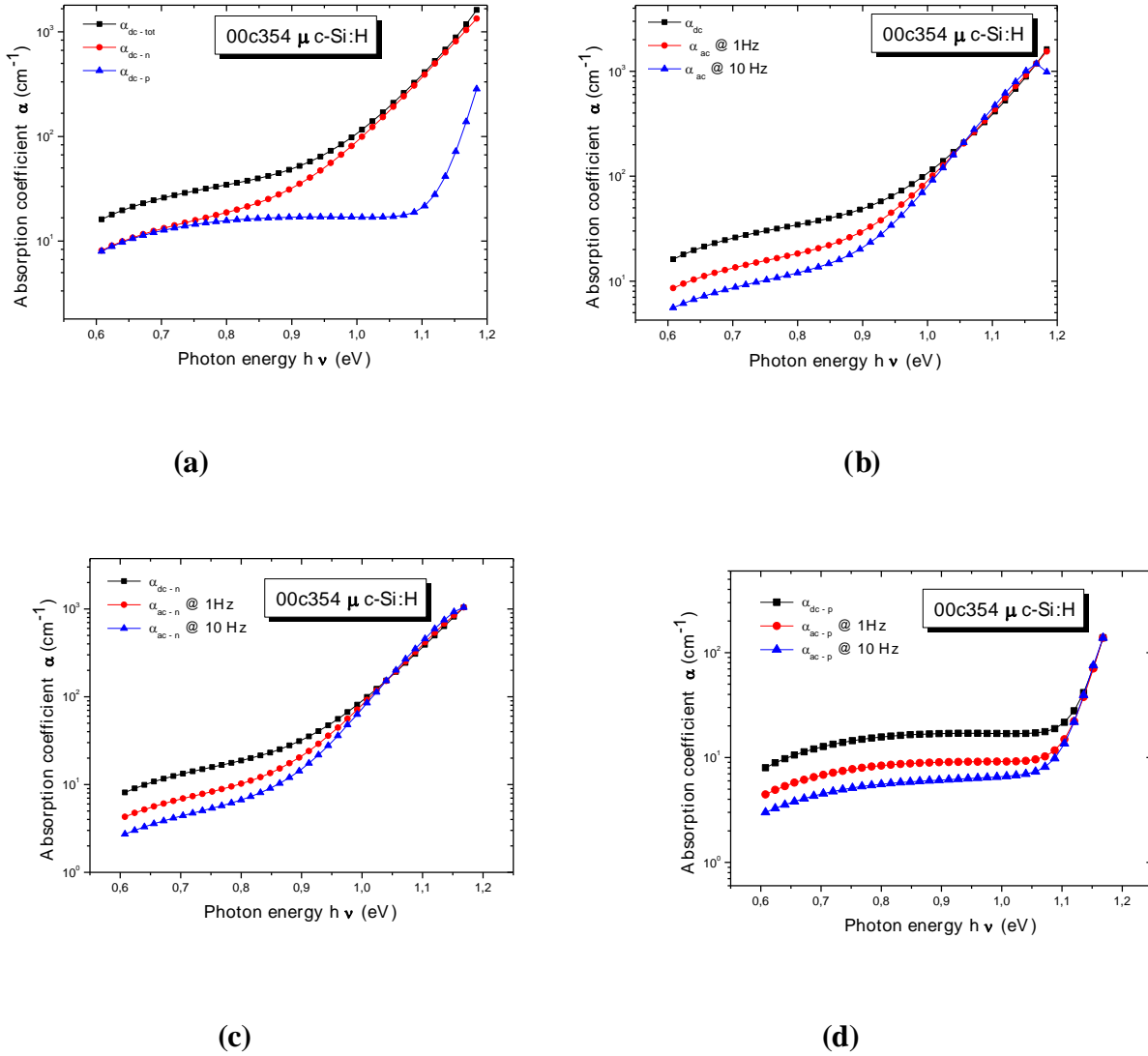


Figure 5.18: Simulated dc-CPM and ac-CPM $\alpha(h\nu)$ spectrum at several frequencies using the $\mu\text{c-Si:H}$ DOS model.

(a) dc- $\alpha_{tot}(h\nu)$, dc- $\alpha_n(h\nu)$ and dc- $\alpha_p(h\nu)$

(b) dc- $\alpha_{tot}(h\nu)$, ac- $\alpha_{tot}(h\nu)$ at 1 Hz and 10 Hz

(c) dc- $\alpha_n(h\nu)$, ac- $\alpha_n(h\nu)$ at 1 Hz and 10 Hz

(d) dc- $\alpha_p(h\nu)$, ac- $\alpha_p(h\nu)$ at 1 Hz and 10 Hz

The figures 5.18.b, 5.18. c and 5.18.d illustrate the difference between the simulated dc-CPM and ac-CPM for microcrystalline material at several frequencies. It is clear from this figure that this discrepancy is only observed in defect energy while in tail region the two curves coalesce. This discrepancy is the same often observed between sub-gap absorption spectra in hydrogenated amorphous silicon.

In figure 5.19, we have presented the measured ac absorption coefficient of microcrystalline silicon thin films prepared by VHF PECVD (00c354) at 5 Hz using the ac-CPM set up depicted in figure 5.5. Optical absorption coefficient $\alpha(h\nu)$ determined from the transmittance and for crystalline silicon are both shown for comparison.

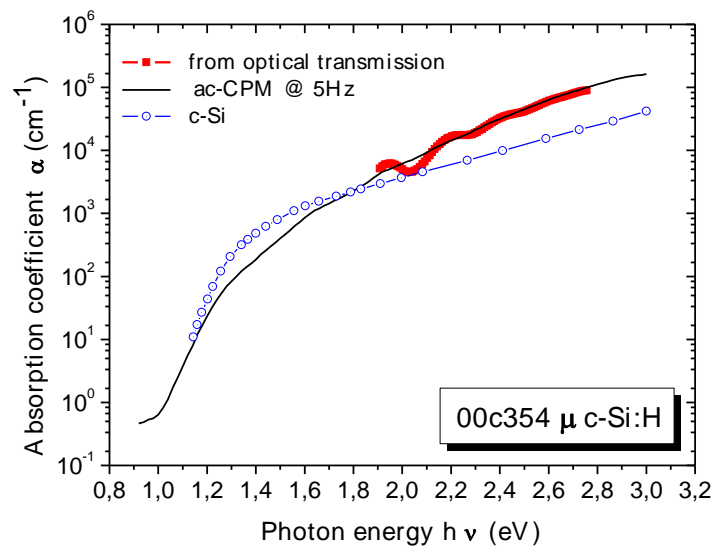


Figure 5.19: Absolute ac-CPM $\alpha(h\nu)$ spectrum measured at 5 Hz frequency for the 00c354 sample. $\alpha(h\nu)$ determined from the transmittance and $\alpha(h\nu)$ for crystalline silicon are both shown for comparison.

For $h\nu < 1.8$ eV the absorption spectrum is close to the crystalline silicon spectrum because of high crystalline fraction of the material while for $h\nu < 1$ eV, the curve is showing similarities to a defect tail because of the contribution of the amorphous phase.

The following figure illustrate the difference between the measured dc-CPM and ac-CPM at 5 Hz for $\mu\text{c-Si:H}$ 00c354 sample especially in deep defect region.

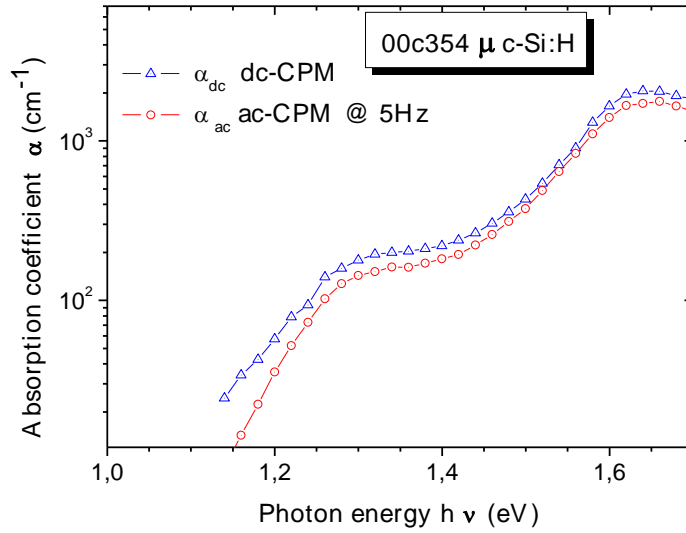


Figure 5.20: Measured dc-CPM and ac-CPM $\alpha(h\nu)$ spectrum at 5 Hz frequency for $\mu\text{c-Si:H}$ 00c354 sample.

b) Density of states distribution

In figure 5.21, we have plotted the measured ac absorption coefficient of microcrystalline silicon 00c 354 sample at 60 Hz and the corresponding density of states distribution extracted using the derivative method of Pierz et al [21].

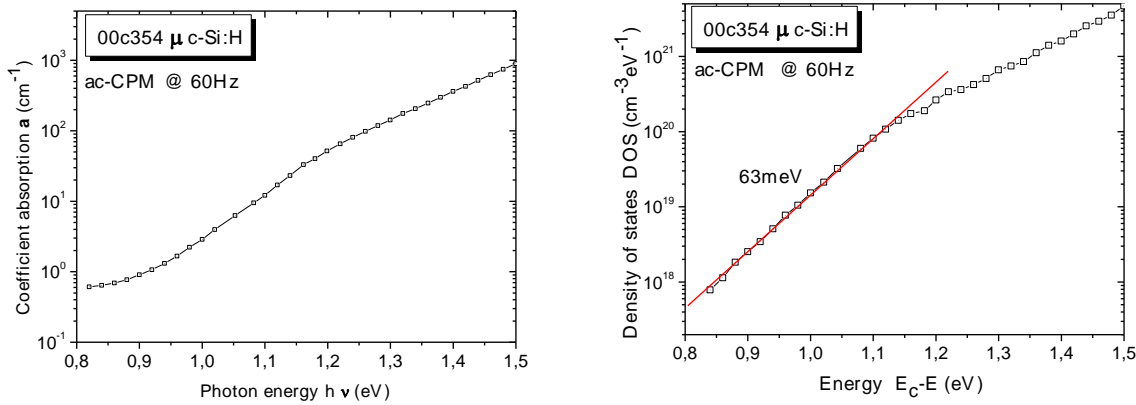


Figure 5.21: (a) Measured ac absorption coefficient at 60Hz
 (b) Extracted DOS distribution using the measured ac absorption spectrum

Figure 5.21.b shows that the density of localized tail states is found to be exponentially distributed in the VB region (63meV), though at deeper energetic positions the DOS decays very slowly.

Figure 5.22 shows a sketch of the density of states profile: below the conduction band edge as found by Main's group using TPC technique [29], and upper the valence band edge as found by us using the measured $ac-\alpha(h\nu)$ of figure 5.21.

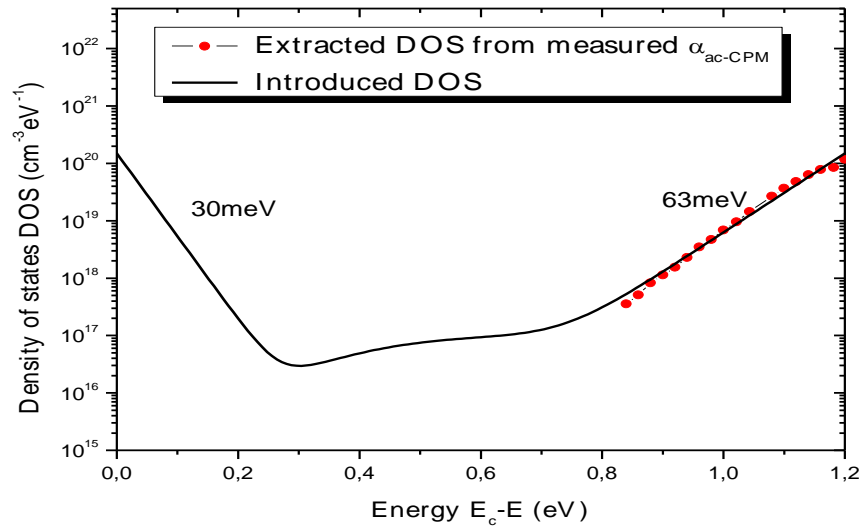


Figure 5.22: Introduced DOS according to CPM and TPC

The DOS is found to have slowly decaying states for the valence band tail (63meV) and a steeper tail for the conduction band tail (30meV).

In figure 5.23, the measured and the simulated absorption coefficient at frequency 60 Hz are presented. The two curves are in excellent agreement.

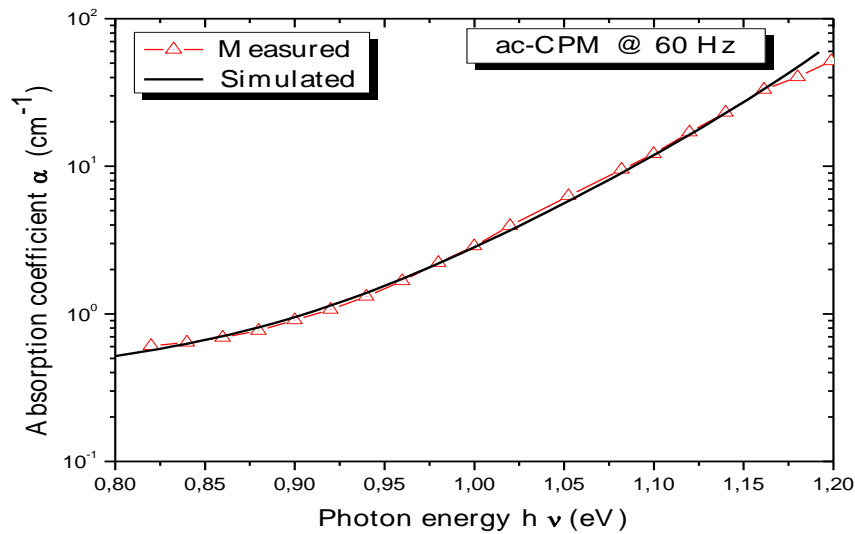


Figure 5.23: Measured and simulated absorption coefficients

By means of the derivative method of Pierz et al [21], the computed $ac\text{-}\alpha_n(h\nu)$, $ac\text{-}\alpha_p(h\nu)$ and total $ac\text{-}\alpha(h\nu)$ at 60 Hz are used to reconstruct from each component the corresponding DOS distribution. Figure 5.24 shows the actual and the extracted DOS.

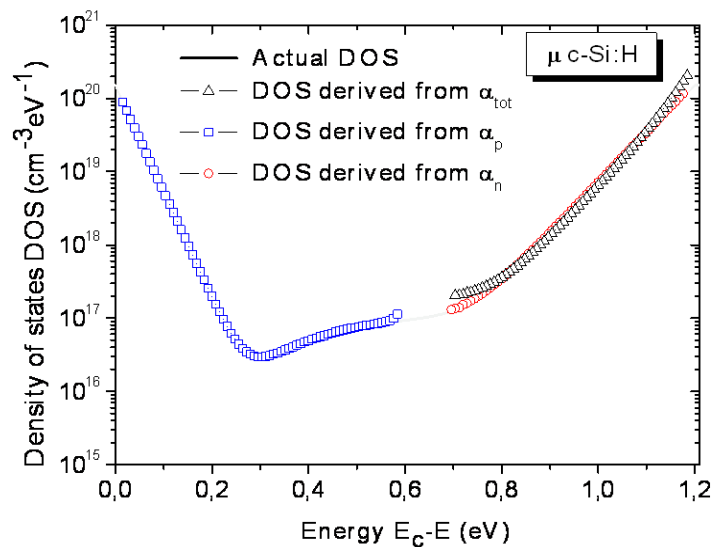


Figure 5.24: Reconstructed DOS from $\alpha_{tot}(h\nu)$, $\alpha_n(h\nu)$ and $\alpha_p(h\nu)$ spectra with ac-CPM at frequency 60Hz, showing a total recovery of the most band gap.

It turns out that the reconstructed DOS is a good fit to the DOS model partially suggested by the DOS portions determined from the measured total α ($h\nu$) and total TPC. So, we have been able to reconstruct complete DOS distributions over a wide range energy of our $\mu\text{-Si:H}$ sample.

In conclusion, one can sketch a schematic band diagram for microcrystalline silicon by combining the measurement and simulation results. According to found results it could be shown that the energetic distribution of the DOS consist of two Gaussian distributions DB1 and DB2 states within the band gap and conduction and valence band-tail states which falls exponentially towards the gap with a band width of 30 meV and 63meV respectively. However, the results obtained in this work are confirmed by a recent investigations using photoluminescence suggest that an exponential distribution applies for the conduction band-tail and by the ESR signal of intrinsic microcrystalline silicon shows an asymmetric line shape which can be described by two Gaussian distributions DB1 and DB2. [30].

5.7.4. Semi-insulating Cr doped Gallium arsenide SI-GaAs : SI- GaAs :Cr sample #1713

1. Parameters choice

Gallium arsenide GaAs material is widely used in the semiconductor industry due to its wider direct band gap energy and higher electron mobility ($E_g=1.42$ eV and $\mu_n=8500$ $\text{cm}^2\text{V}^{-1}\text{s}^{-1}$) compared to crystalline silicon ($E_g=1.12$ eV and $\mu_n=1350$ $\text{cm}^2\text{V}^{-1}\text{s}^{-1}$). These properties make this material very useful for infrared light emitting and laser diodes manufacturing. GaAs can be doped with Chromium (Cr) in order to obtain a semi-insulating gallium arsenide (SI-GaAs:Cr) substrate as silicon dioxide. Chromium behaves as an acceptor with an impurity level close to the centre of the energy gap. GaAs can be also doped with silicon to give either n-type or p-type GaAs depending on temperature.

Figure 5.25.a show the measured Cr doped GaAs CPM spectrum. A rapid decrease in the absorption coefficient is observed at about 1.4eV which is the band edge for this material. Figure 5.25.b shows the density of states distribution of occupied states close to valence band edge derived from figure 5.25.a using the derivative method of Pierz et al [21].

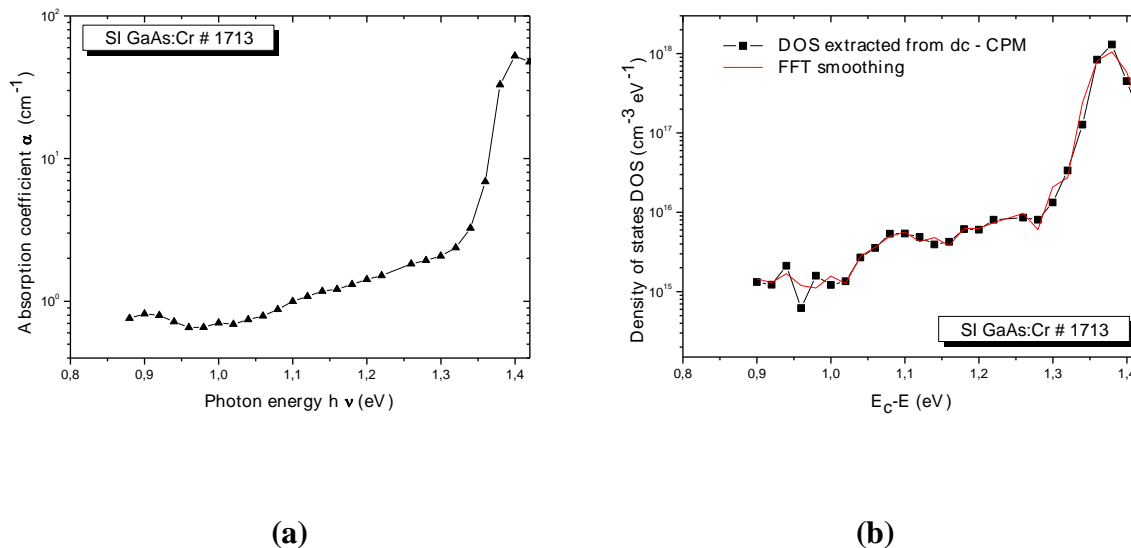


Figure 5.25: (a) dc-CPM spectrum

(b) Corresponding density of states distribution for SI GaAs:Cr # 1713 sample

So, a density of states distribution model for the semi-insulating Cr-doped GaAs is introduced and shown in figure 5.26. The introduced density of states consist of two parts: (i) The lower part close to conduction band edge is derived from transient photocurrent measurement TPC [31], high resolution photoinduced transient spectroscopy HRPITS and modulated photocurrent measurements MPC [32], (ii) while the upper part near the valence band edge is derived from CPM measurement as shown in figure 5.25.b. The most important parameters used for this density of states distribution are summarized in table 5.5.

Table 5.5: Density of states parameters used in optical absorption spectrum modelling of SI GaAs:Cr.

Electron mobility	$\mu_n = 4400 \text{ cm}^2 \text{ V}^{-1} \text{ s}^{-1}$
Hole mobility	$\mu_p = 100 \text{ cm}^2 \text{ V}^{-1} \text{ s}^{-1}$
Density of states at the mobility edges E_c	$N_c = 4.7 \times 10^{17} \text{ cm}^{-3}$
Density of states at the mobility edges E_v	$N_v = 7 \times 10^{18} \text{ cm}^{-3}$
Mobility Gap	$E_g = 1.42 \text{ eV}$
Temperature	$T = 300^\circ \text{K}$
Fermi level position E_F^3	0.75 eV

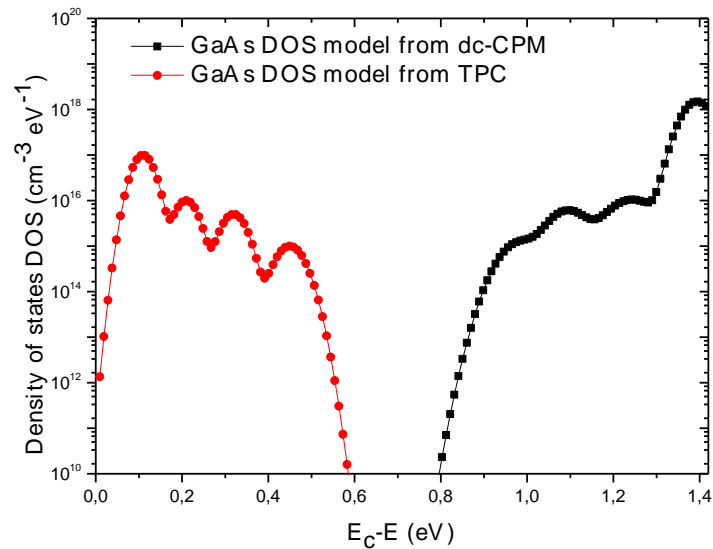


Figure 5.26: Semi-insulating Cr-doped GaAs density of states distribution model used for CPM numerical modelling

³ E_F is calculated from the charge neutrality condition.

Using the SI GaAs:Cr DOS model, we have computed by our CPM program code the total absorption coefficient α_{dc-tot} and its components α_{dc-n} and α_{dc-p} . These absorption spectra are used to infer the density of states over the energy gap near band edge and close to mid-gap. Figures 5.27 and 5.28 show the obtained results. As we can see the actual DOS is well fitted over a large region of the band gap of the semi-insulating Cr-doped GaAs.

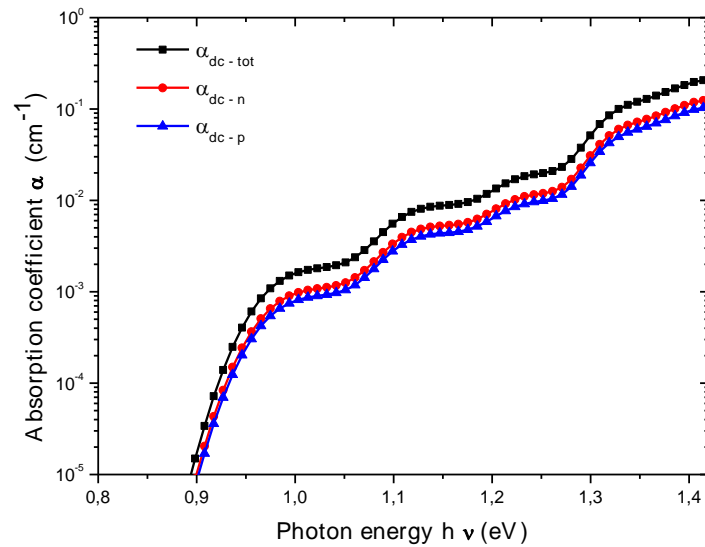


Figure 5.27: Simulated dc-CPM spectra for Cr doped GaAs using the DOS of figure 5.26:

- (■) total absorption spectrum $\alpha_{dc-tot}(h\nu)$.
- (●) Simulated dc-CPM electron absorption spectrum $\alpha_{dc-n}(h\nu)$.
- (▲) Simulated dc-CPM hole absorption spectrum $\alpha_{dc-p}(h\nu)$.

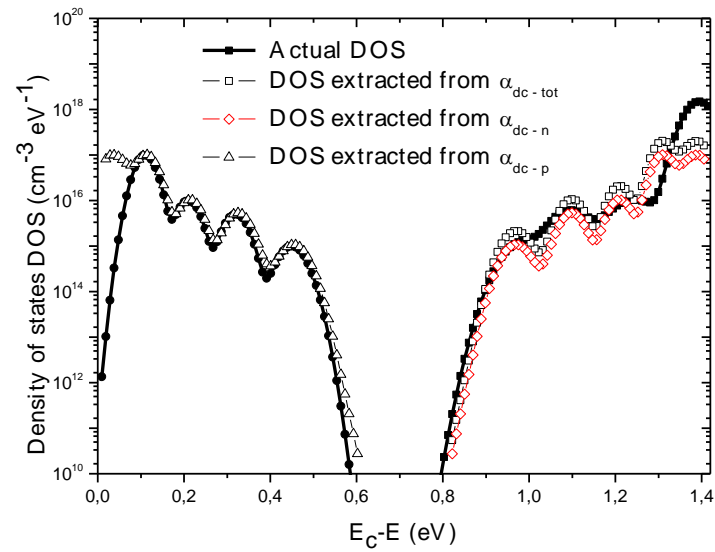


Figure 5.28: Reconstructed density of states from absorption spectra of figure 5.27

In conclusion, the measurement results have shown that the absolute CPM technique is applicable to non-silicon materials such as Gallium Arsenide and to any photoconductive materials. While, and on the other hand, the simulation results have allowed us the determination of the distribution of defects below and above the Fermi level from $\alpha_{dc-n}(h\nu)$ and $\alpha_{dc-p}(h\nu)$ absorption coefficients. It is also found that by combining of the two well known measurement methods CPM and TPC, and the two experimentally inaccessible optical absorption coefficients components $\alpha_n(h\nu)$ and $\alpha_p(h\nu)$, we are able to have a full reconstruction of the occupied and unoccupied density of states distribution for such materials.

5.7.5 Ultra high frequency effect

Using our computer modeling of the dc- and ac-CPM spectra we will study, in this subsection, the ultra high frequency effect on the characterization of undoped hydrogenated amorphous silicon in terms of absorption spectra and defect density of state distribution.

a) Absorption spectrum

As it can be seen in figure 5.29, for high frequencies greater than 100Hz; the difference between absorption spectrum is observed also in the Urbach edge region. This discrepancy moves to the Urbach tail as frequency increases until reaching a total difference between the dc and ultra high frequency (10^{12} Hz) spectra over all energy range. This interesting feature is very important especially in the DOS reconstruction as we will see below.

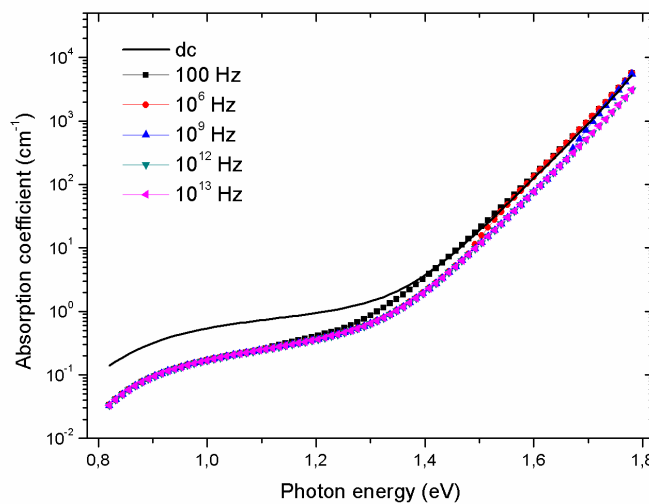


Figure 5.29: Simulated dc-CPM and ac-CPM $\alpha(h\nu)$ spectrum at several frequencies (from 100Hz to 10^{13} Hz), showing considerable differences in the Urbach edge region as the frequency increases and saturation of the ac $\alpha(h\nu)$ above 100 Hz in the defect region below about 1.35 eV.

The discrepancy between the low and ultra high frequency ac-CPM can be explained by the difference between the indirect transitions rates involved at each frequency. These latter are more ignored as the frequency increases until saturation at 10^{12} Hz at which the shallow tail states transitions are completely not detected. This case is often assumed in computing the DOS from dc-CPM.

To further illustrate this feature we present in figure 5.30.a and figure 5.30.b the optical absorption coefficients due to electron and hole transitions in dc and ac modes.

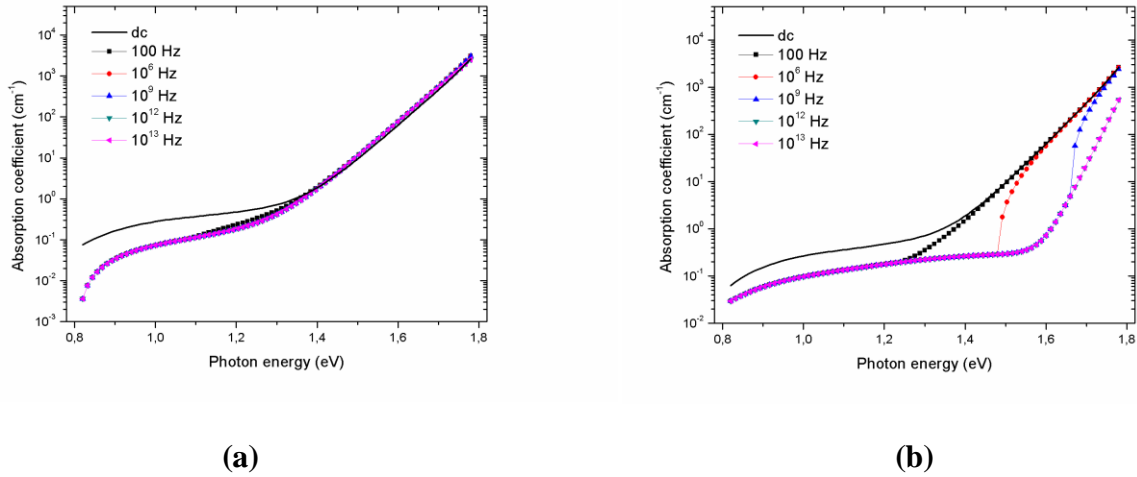


Figure 5.30: (a) Simulated dc-CPM and ac-CPM $\alpha_n(h\nu)$ spectrum at several frequencies (from 100Hz to 10^{13} Hz), showing no difference in the Urbach edge region as the frequency increases and saturation of the ac $\alpha_n(h\nu)$ above 100 Hz in the defect region below about 1.35eV.

(b) Simulated dc-CPM and ac-CPM $\alpha_p(h\nu)$ spectrum at several frequencies (from 100Hz to 10^{13} Hz), showing significant differences in the Urbach edge region as the frequency increases and saturation of the ac $\alpha_p(h\nu)$ above 100 Hz in the defect region below about 1.35eV.

It is worth noting that this discrepancy between frequencies is more announced in $\alpha_p^{ac}(h\nu)$ spectra for the reason that the holes mobility is chosen less than electrons.

b) Density of states

Figure 5.31.a and figure 5.31.b show the reconstruction of the starting DOS from the ac and dc absorption coefficients and its components. We have obtained satisfactory results using ultra high frequency ac-CPM regime compared to those obtained using dc or low frequency ac-CPM regimes. Indeed, with $\alpha_n^{ac}(h\nu)$ and $\alpha_p^{ac}(h\nu)$, we can extract the density of states in the lower half and in the upper half of the band gap states respectively.

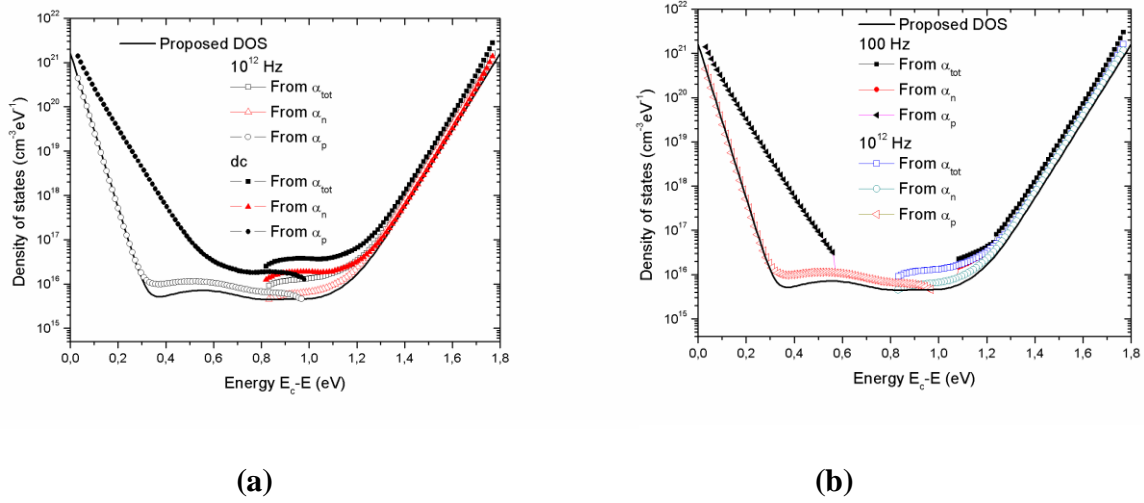


Figure 5.31: (a) Reconstructed $D(E)$ from $\alpha(h\nu)$, $\alpha_n(h\nu)$ and $\alpha_p(h\nu)$ spectra with dc-CPM and ac-CPM at 10^{12}Hz , showing a most reliable recovery in the case of the 10^{12}Hz ac-CPM. (b) Reconstructed $D(E)$ from $\alpha(h\nu)$, $\alpha_n(h\nu)$ and $\alpha_p(h\nu)$ spectra with ac-CPM at two frequencies, 100Hz and 10^{12}Hz , showing a most reliable recovery in the case of ultra-high frequency 10^{12}Hz ac-CPM.

Therefore, the ac-CPM at ultra high frequency can be used to derive the true and the whole DOS (defects and tail states density distribution) but can not be used to get the true optical coefficient absorption while the dc-CPM can give us the true optical absorption coefficient spectra but it can not be used to derive the true DOS.

5.7.6. Light Soaking effect

In this subsection we will discuss the light soaking effect on measured CPM spectra of P-doped hydrogenated amorphous silicon in terms of optical absorption coefficient and energetic defect distribution.

a) Absorption spectrum

Figure 5.32 shows CPM spectra of n-type a-Si:H in the annealed and in the degraded state. It illustrates the evolution of the measured absorption spectrum as function of the illumination time. As we can see from these measurements, while the valence-band tail present no significant change as the sample was degraded, we observe a steady increase of the absorption coefficient in the deep defect region till saturation for the last illumination time. Light soaking causes an increase of the defect absorption and a Fermi level shift towards midgap.

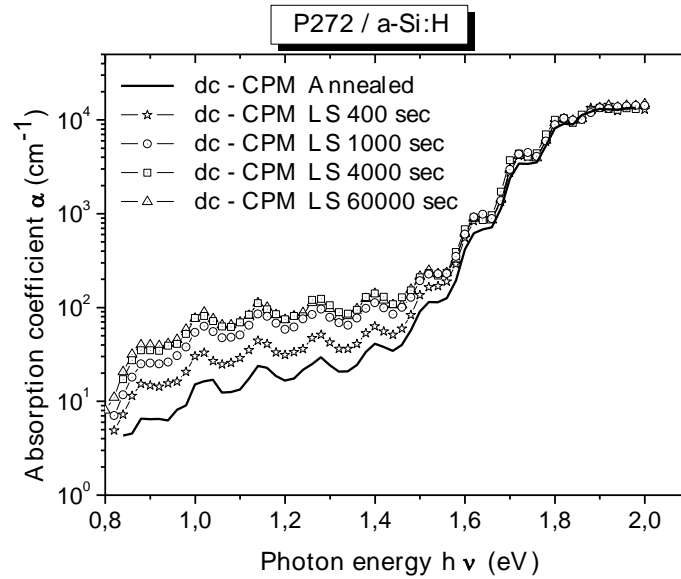


Figure 5.32: Optical absorption coefficient for different illumination times. Annealed state is also shown (solid line)

b) Density of states

In order to obtain the electronic density of states distribution, we have applied a suitable fitting operation for each of the initial CPM data of figure 5.32. We obtain, as shown in figure 5.33, the measured absorption coefficients free of the interference pattern from which we have derived the density of states of our sample by applying the derivative method of Pierz et al [21].

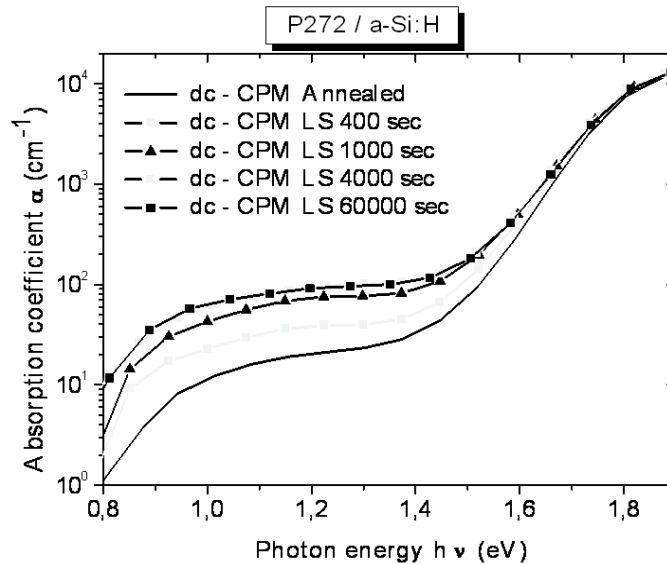


Figure 5.33: Measured optical absorption coefficient for different illumination times after a suitable fitting operation. Annealed state is also shown (solid line)

The resulting DOS is shown in figure 5.34. It can be seen that upon light soaking the defect density increases and the Fermi level shifts towards midgap. Indeed, as the illumination time increases, two peaks grow in the midgap region between the valence band and the Fermi energy in slightly P-doped *a-Si:H*, while the Urbach tail E_0 remains practically unchanged. In a previous work, Sakata et al. [33] and Schmidt et al [27] found two distinct defect states in the lower midgap of undoped *a-Si:H*.

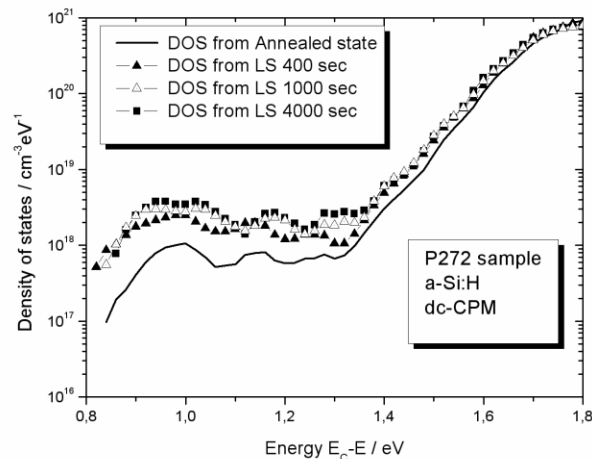


Figure 5.34: Density of filled states, obtained by the derivative method applied to the absorption coefficients data, for different illumination times, annealed state is also shown.

In the following figure, the contribution to optical absorption coefficient from the valence band-tail has been subtracted. As it can be seen in this figure, the occupied densities of defect states consist of two Gaussian peaks that evolve with illumination time until saturation.

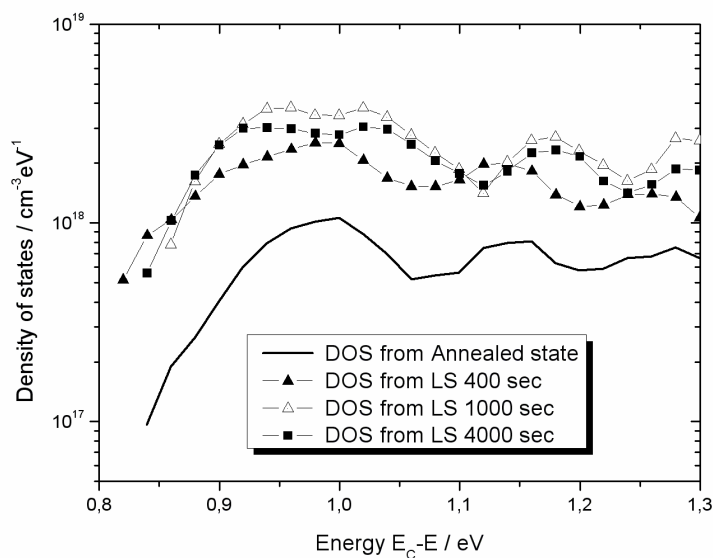


Figure 5.35: Evolution of the defect density of midgap states with illumination time

The Gaussian shape is commonly assumed to describe the deep defect density and it comes from a statistical energy distribution for the defect sites [27]. In accordance with Schmidt et al. [27], the nature of the defect states produced by a strong and prolonged illumination are expected to be unchanged. So, we fit the evolution of the two peaks with Gaussians of constant position and width. The best fit for our complete set of curves was obtained with peak energy position from the conduction band at 0.98 ± 0.01 eV and 1.16 ± 0.01 eV edge, being the width 0.11 ± 0.01 eV and 0.06 ± 0.01 eV respectively. The areas of both peaks tend to increase monotonically as a function of illumination time till saturation, as shown in figure 5.35.

From this figure, two essential results can be obtained: Firstly, the densities of negatively charged defects are greater than the density of neutral ones, in accordance with the prediction of the defect pool model in slightly P-doped materials [34]. Secondly, light induced degradation phenomenon tends to be saturated in the long time limit where the density of defects exceeds the initial defect density by a factor of 2 or more.

References

- [1] Jackson W B, Amer N M, Boccara A C and Fournier D 1981 *Applied Optics* **20** (8) 1333-44.
- [2] Vanecek M, Kocka J, Poruba A and Fejfar A 1995 *J. Appl. Phys.* **78** (10) 6203-10.
- [3] Fejfar A, Poruba A, Vanecek M and Kocka J 1996 *Journal of Non-Crystalline Solids* **198-200** 304-308.
- [4] Hattori K, Adachi Y, Anzai M, Okamoto H and Hamakawa Y 1994 *J. Appl. Phys.* **76** (5) 2841-50.
- [5] Schauer F, Eliat A, Nesladek M and Adriaenssens G J 1994 *Appl. Phys. Lett.* **64** (22) 3009-11.
- [6] Pickin W, Alonzo J C and Mendoza D 1987 *J. Phys. C: Solid State Phys.* **20** 341-345.
- [7] Sladek P, Stahel P and Theye M L 1995 *Philosophical Magazine B* **71** (5) 871-880.
- [8] K. Hattori, S. Fukuda, K. Nishimura, H. Okamoto, and Y. Hamakawa, *Journal of Non-Crystalline Solids* 164-166 (1993) 351-354.
- [9] Sauvain E, Mettler A, Wyrsh N and Shah A 1993 *Solid State Communications* **85** (3) 219-222.
- [10] Shimizu T, Sugiyama H and Kumeda M 2001 *Solar Energy Materials and Solar Cells* **66** 203-207.
- [11] Bube R H, Benatar L E, Grimbergen M N and Redfield D 1992 *J. Appl. Phys.* **72**(12) 5766-77.
- [12] Mettler A, Wyrsh N, Goetz M and Shah A 1994 *Solar Energy Materials and Solar Cells* **34** 533-539.
- [13] Zhang Q and Adriaenssens G J 1997 *J. Appl. Phys.* **81**(10) 6795-99.
- [14] Schmidt J A, Koropecski R R, Arce R D, Rubinelli F A and Buitrago R H 2000 *Thin Solid Films* **376** 267-274.
- [15] Conte G, Irena F, Nobile G and Palma F 1993 *Journal of Non-Crystalline Solids* **164-166** 419-22.
- [16] Sladek P and Theye M L 1994 *Solid State Communications* **89** (3) 199-203.
- [17] Hasegawa S, Nitta S and Nonomura S 1996 *Journal of Non Crystalline Solids* **198-200** 544-547.
- [18] C. Main, S. Reynolds, I. Zrinscak and A. Merazga *Journal of Non Crystalline Solids* **338-340** (2004), 228-231.

- [19] A. Merazga, "Steady state and transient photoconductivity in n-type a-Si", PhD. thesis, Dundee Institute of Technology, Dundee, UK, 1990.
- [20] D. Ritter and K. Weiser, *Optics Communications* Vol.57, No. 5, pp.336-338, 1986.
- [21] K. Pierz, B. Hilgenberg, H. Mell and G. Weiser, *Journal of Non-Crystalline Solids* **97-98**, 1987, pp. 63-66.
- [22] S. Heck, "Investigation of light-induced defects in hydrogenated amorphous silicon by low temperature annealing and pulsed degradation", PhD Thesis, der Philipps-Universität Marburg, Marburg/Lahn 2002.
- [23] J. Tauc, R. Grigorovici and A. Vancu, *Phys. Stat. Sol.* **15** (1966), 627
- [24] R. H. Klazes, M. H. L. M. van der Broek, J. Bezemer and S. Radelaar, *Philos. Mag.* **45** (1983) 377.
- [25] S. Nitta, S. Itoh, M. Tanaka, T. Endo and A. Hatano, *Sol. Energy Mater.* **8** (1982) 249.
- [26] T. Searle, "Properties of Amorphous Silicon and its Alloys", Edited by University of Sheffield, UK, 1998.
- [27] J. A. Schmidt, R. Arce, R.H. Buitrago, and R. R. Koropecski, *Physical Review B*, Vol. 55, No.15, pp. 9621-9627, April 1997-1.
- [28] C. Main, S. Reynolds, I. Zrinscak and A. Merazga, *Journal of Materials Science-Materials in Electronics*, **14** 681-684, 2003.
- [29] S. Reynolds, V. Smirnov, C. Main, R. Carius and F. Finger, *Mat. Res. Soc. Symp. Proc.* Vol. 715 © Materials Research Society, 2002.
- [30] Von Thorsten Dylla, "Electron Spin Resonance and Transient Photocurrent Measurements on Microcrystalline Silicon", PhD. thesis, Fachbereich Physik, Freie Universität Berlin, Germany, 2004.
- [31] H. Belgacem, A. Merazga and C. Longeaud, *Semiconductor Science and Technology* **20** (2005) 56-61.
- [32] C. Longeaud, J. P. Kleider, P. Kaminski, R. Kozłowski, M. Pawłowski, and J. Cwirko, *Semiconductor Science and Technology* **14** (1999) 747-756.
- [33] I. Sakata, M. Yamanaka, S. Numase, and Y. Hayashi, *J. Appl. Phys.*, **71** (9), 4344-4353, 1992.
- [34] J. Schmal, *Journal of Non-Crystalline Solids*, **198-200**, 387-390, 1996.

CHAPTER 6

GENERAL CONCLUSIONS

6.1. Conclusions

Constant Photocurrent Method (CPM) has been used extensively as a means of characterising thin film semiconductors. CPM measurements using steady (dc) or modulated (ac) sub-gap excitation permit the determination of the optical absorption associated with the density of defect states (DOS). However, slow photoresponse times in materials like a-Si:H often influence the ac measurement, and hence optical absorption spectra obtained by ac and dc-CPM can be very different.

In the present work, both measurements and numerical simulation of CPM absorption spectrum for dc and ac optical excitation conditions have been carried out to determine the density of gap-states distribution in amorphous and crystalline semiconductors such as a-Si:H/ $\mu\text{c-Si:H}$, as typical of amorphous semiconductors and GaAs as typical of crystalline semiconductors.

For this reason, a general numerical simulation program of dc and ac constant photocurrent method (dc-CPM and ac-CPM) has been developed. This code program is based on several density of states models typical for hydrogenated amorphous silicon (a-Si:H), hydrogenated microcrystalline silicon ($\mu\text{c-Si:H}$) and gallium arsenide (GaAs) materials and take into account all possible thermal and optical transitions between localised states and extended states.

For the case of hydrogenated amorphous silicon both intrinsic and n-type, a density of states (DOS) model has been chosen according to the improved defect pool model (DPM) of Powell

and Dean. The density of states models for microcrystalline silicon and gallium arsenide have been taken from literature with appropriate parameters.

In addition, we have performed experimental measurement of CPM on semiconductor materials with applications in solar energy. In order to validate the simulation results, measurements of dc and ac-CPM have been performed particularly on the following samples: intrinsic and doped a-Si:H (Intersolar ISB4, P272) and $\mu\text{c-Si:H}$ (00c354) and also semi-insulating Cr-doped GaAs (SI GaAs:Cr #1713)..

We have presented in this thesis the difference observed for the optical absorption coefficients and the density of deep defect states between the ac and the dc modes.

The difference in ac and dc absorption spectra arises from the frequency dependence of the different excitation pathways by which free electrons and free holes can be produced by sub-gap excitation. ac modulated excitation will reveal absorption associated with transitions from occupied states below Fermi level E_F , into the conduction band, while dc excitation will include transitions from the valence band into unoccupied defect states above E_F , followed by slow thermal emission to the conduction band. In the other hand, analysis of the $\alpha_n(h\nu)$ and $\alpha_p(h\nu)$ absorption spectrum components corresponding to optical transitions associated with free electrons and free holes creation, respectively, allows the two regions of the DOS, above and below the Fermi level, to be determined. So, we have been able to obtain the density of states distribution within the gap of such semiconductors materials by applying the derivative method of Pierz et al to the both dc- $\alpha(h\nu)$ and ac- $\alpha(h\nu)$ data and also to the experimentally inaccessible components $\alpha_n(h\nu)$ and $\alpha_p(h\nu)$.

We report on the use of this method in studying the effects of high frequency on different regions of the DOS in a-Si:H (especially ultra high frequency).

Comparative analysis of *DOS* distributions, determined from the dc and ac-CPM at frequencies in the range $1-10^2\text{Hz}$, results in the conclusion that, the indirect transitions involving subsequent slow thermal emissions are responsible of the difference between different frequency-ac-CPM-determined *DOS*. Consequently, at sufficiently high frequency, compared to thermal emission rates, the occupied states below the quasi-Fermi level are revealed from the $\alpha_n(h\nu)$ spectra, while the empty states are revealed from the $\alpha_p(h\nu)$ spectra. High frequency ac-CPM is, therefore, most reliable as a spectroscopy method for the *DOS* distribution.

Furthermore, at ultra-high frequency in the range 10^2 - 10^{13} Hz, the entire ac-CPM-determined *DOS* distribution could be reliably determined by deconvolution of both absorption coefficient spectra $\alpha_n^{ac}(h\nu)$ and $\alpha_p^{ac}(h\nu)$. Our simulations reveal that the dc-CPM and the ac-CPM at ultra-high frequency yield optical absorption spectra with significant differences, not only below the Urbach edge, as for low frequency ac-CPM, but also in the Urbach edge. The reliability to infer the *DOS* distribution by deconvolution of both $\alpha_n^{ac}(h\nu)$ and $\alpha_p^{ac}(h\nu)$ spectra at ultra-high frequency is demonstrated.

In this thesis, by using the constant photocurrent measurement in dc-mode, we have investigated the effect of the light soaking (*LS*) on the deep defect density (N_d) and the slope of the Urbach tail (E_o) of the slightly P-doped *a-Si:H* film prepared by PECVD in term of evolution of the measured sub-gap absorption coefficient and density of states distribution as function of illumination time. The derivative method applied to the *dc- $\alpha(h\nu)$* data allowed us to obtain the occupied density of states. The measurement results in terms of absorption spectrum and deep defect density shows an increase of both with illumination time until saturation. The dominant metastable defects are the dangling bonds. In fact, their densities pass from $5 \times 10^{17} \text{ cm}^{-3} \text{ eV}^{-1}$ in an initial state to $5 \times 10^{18} \text{ cm}^{-3} \text{ eV}^{-1}$ in a degraded state while the tail states remains basically constant. The *DOS* showed the presence of two Gaussian distribution between the valence band and the Fermi energy with two peaks. These two peaks have constant positions and widths which do not changed considerably with illumination. We have assigned the peak closer to the valence band to the negatively charged defects D^- and the other peak (midgap peak) to the neutral dangling bonds D^0 . We have also found that the densities of both defects grow as $t_{ill}^{1/3}$. This is in agreement with ESR measurements, which show a spin density growing with the same time dependence.

The electronic properties of microcrystalline silicon films have been studied in the present thesis, by using constant photocurrent technique in ac regime. We have employed the numerical computer program of ac-CPM to elucidate the experimental results. Analyzing the measured and simulated absorption coefficients, it was found that the density of valence band-tail states falls exponentially towards the gap with a typical band-tail width of 63 meV and a conduction band tail slope of some 30 meV. Combining the information derived in this work

a schematic picture of the density of states in energetic sense has been obtained. Our study indicates then that the constant photocurrent method is able to extract the whole density of localized states in highly-crystalline $\mu\text{c-Si:H}$ films.

Finally, constant photocurrent method (CPM) is used to investigate the defect levels from the optical absorption spectra of semi-insulating Cr-doped GaAs. By deconvolution of the optical absorption spectrum, we have extracted the distribution of the density of states within the gap. We have developed a computer code program which has been used to reconstruct the measured dc and ac- CPM optical absorption spectrum by using the extracted density of states as a model of state distribution. It is also found that with the application of the two complementary techniques: constant photocurrent method (CPM) and modulated photocurrent (MPC), we are able to have a full reconstruction of the density of states distribution for such materials.

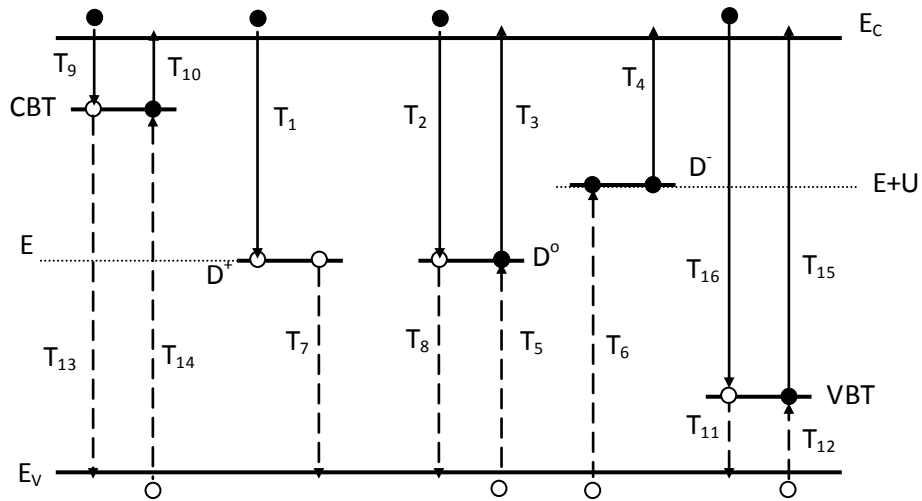
As a conclusion, the dc method have usually been favored in measurement of optical absorption whereas the ac measurements using high chopping frequency is to be preferred to yield to the true density of states distribution. Hence dc- and ac-CPM should be used both as a useful spectroscopy methods for materials characterisation.

6.2. Suggestions for further work

However, we believe that there is still much to do. For example, in recently paper Main et al. reported that the detail knowledge of the differences in ac- and dc- derived absorption spectra give us the possibility to use both ac and dc CPM, not only to obtain information on the DOS below the Fermi level E_F - i.e. occupied states, but also on the density of unoccupied states above E_F .

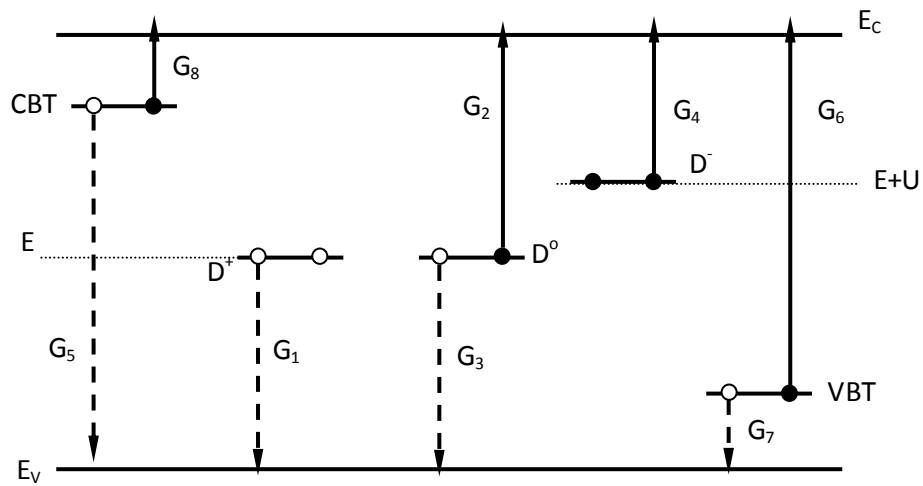
So, we suggest, in one side, to exploring the differences and similarities between dc and ac- CPM which can be helpful to characterise various materials (nano-, micro-, poly crystalline, polymorphous silicon,...etc) with both configuration coplanar (films) and sandwich (solar cells and photoconductors). On the other side, the combination of several similar techniques (CPM, PDS and MPC even TPC and SCLC TOF) can lead to a successful characterisation of such variety and new materials with applications in solar cells and photodetectors.

APPENDICES



\circ : Hole, \bullet : Electron, $- - \rightarrow$: Hole transitions, \longrightarrow : Electron transitions

Figure 1: Carrier transitions involved in the CPM simulation: Thermal transitions



O: Hole, ●: Electron, - - → : Hole transitions, —→ : Electron transitions

Figure 2: Carrier transitions involved in the CPM simulation: Optical transitions

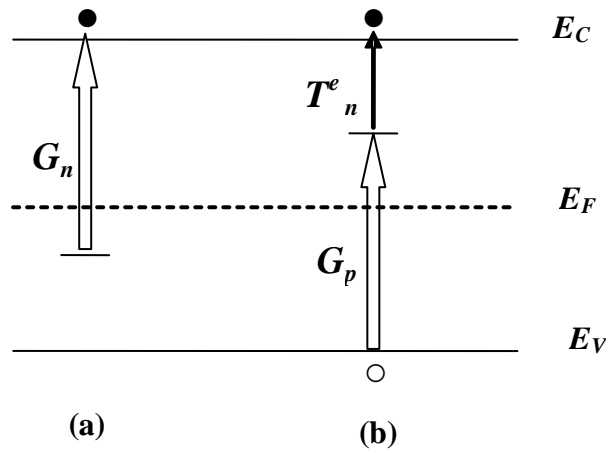


Figure 3: Two optical transition categories according to Main ac-CPM analysis [25]:

(c) Direct transitions creating free electrons (●) with rate $G_n(E, h\nu, \omega)$.

(d) Indirect double transitions creating free holes (○): an optical transition from the valence band to an empty state at E above E_F , with rate $G_p(E, h\nu, \omega)$, followed by a thermal transition from E to the conduction band with rate $T_n^e(E)$.

Appendix A

Expression of the dc thermal transitions

With reference to figure 1 and using equations (4.34) & (4.35), the expressions of possible thermal transitions per unit volume and unit time under dc regime are linked to the capture and emission coefficients and given by the usual Shockley-Read-Hall formulas as follow:

- Dangling bonds:

$$\begin{aligned}
 T_1^{dc}(E) &= C_n^+ n_{dc} D_{dc}^+(E) \\
 T_2^{dc}(E) &= C_n^o n_{dc} D_{dc}^o(E) \\
 T_3^{dc}(E) &= C_n^+ n_1^+(E) D_{dc}^o(E) \\
 T_4^{dc}(E) &= C_n^o n_1^o(E) D_{dc}^-(E) \\
 T_5^{dc}(E) &= C_p^o p_{dc} D_{dc}^o(E) \\
 T_6^{dc}(E) &= C_p^- p_{dc} D_{dc}^-(E) \\
 T_7^{dc}(E) &= C_p^o p_1^o(E) D_{dc}^+(E) \\
 T_8^{dc}(E) &= C_p^- p_1^-(E) D_{dc}^o(E)
 \end{aligned} \tag{A.1}$$

- Tail states:

$$\begin{aligned}
 T_9^{dc}(E) &= C_n^c n_{dc} (D_{cvt}(E) - n_t^{dc}(E)) \\
 T_{10}^{dc}(E) &= C_n^c n_1(E) n_t^{dc}(E) \\
 T_{11}^{dc}(E) &= C_p^v p_1(E) p_t^{dc}(E) \\
 T_{12}^{dc}(E) &= C_p^v p_{dc} (D_{vbt}(E) - p_t^{dc}(E)) \\
 T_{13}^{dc}(E) &= C_p^c p_1(E) (D_{cvt}(E) - n_t^{dc}(E)) \\
 T_{14}^{dc}(E) &= C_p^c p_{dc} n_t^{dc}(E) \\
 T_{15}^{dc}(E) &= C_n^v n_1(E) (D_{vbt}(E) - p_t^{dc}(E)) \\
 T_{16}^{dc}(E) &= C_n^v n_{dc} p_t^{dc}(E)
 \end{aligned} \tag{A.2}$$

where:

C_n^v, C_n^c : Capture coefficient of electrons by VBT and CBT states respectively;

C_p^v, C_p^c : Capture coefficient of holes by VBT and CBT states respectively;

$n_1(E)$: Effective electron emission density for band-tail state

$p_1(E)$: Effective hole emission density for band-tail state

C_n^+, C_n^0 : Capture coefficient of electrons by positively and neutral states respectively;

C_p^-, C_p^0 : Capture coefficient of holes by negatively and neutral states respectively;

$n_1^0(E)$: Effective electron emission density for $D^{0/}$ transition

$n_1^+(E)$: Effective electron emission density for $D^{0/+}$ transition

$p_1^0(E)$: Effective hole emission density for $D^{+/0}$ transition

$p_1^-(E)$: Effective hole emission density for $D^{0/-}$ transition

Under thermodynamic equilibrium conditions when no light is present, the emission coefficients are deduced from the principle of detailed balance [3, 4]. In this case, we have:

$$T_1(E) = T_3(E)$$

$$T_2(E) = T_4(E)$$

$$T_5(E) = T_7(E)$$

$$T_6(E) = T_8(E)$$

(A.3)

$$T_9(E) = T_{10}(E)$$

$$T_{11}(E) = T_{12}(E)$$

$$T_{13}(E) = T_{14}(E)$$

$$T_{15}(E) = T_{16}(E)$$

Taking into account the three set of equations (A.1), (A.2) and (A.3), we obtain the following quantities for the emission coefficients:

$$e_n^o(E) = C_n^+ n_1^+(E) = C_n^+ n_{th} \frac{f_{th}^+(E)}{f_{th}^o(E)}$$

$$e_n^-(E) = C_n^o n_1^o(E) = C_n^o n_{th} \frac{f_{th}^o(E)}{f_{th}^-(E)}$$

$$\begin{aligned}
e_p^o(E) &= C_p^- p_1^-(E) = C_p^- p_{th} \frac{f_{th}^-(E)}{f_{th}^o(E)} \\
e_p^+(E) &= C_p^o p_1^o(E) = C_p^o p_{th} \frac{f_{th}^o(E)}{f_{th}^+(E)} \\
e_n^c(E) &= C_n^c n_1(E) = C_n^c n_{th} \frac{1 - f_{th}^{cbt}(E)}{f_{th}^{cbt}(E)} \\
e_p^v(E) &= C_p^v p_1(E) = C_p^v p_{th} \frac{1 - f_{th}^{vbt}(E)}{f_{th}^{vbt}(E)} \\
e_p^c(E) &= C_p^c p_1(E) = C_p^c p_{th} \frac{f_{th}^{cbt}(E)}{1 - f_{th}^{cbt}(E)} \\
e_n^v(E) &= C_n^v n_1(E) = C_n^v n_{th} \frac{f_{th}^{vbt}(E)}{1 - f_{th}^{vbt}(E)}
\end{aligned} \tag{A.4}$$

where the script “*th*” stands for thermal equilibrium. It is usually supposed that the capture and emission rates under non-equilibrium steady state remain unchanged with respect to thermal equilibrium conditions.

Appendix B

Expression of the dc photogeneration rates

Before setting up the generation rates we define three step functions U , V and W by:

$$U(E - h\nu) = \begin{cases} 1 & \text{if } E - h\nu < E_V \\ 0 & \text{otherwise} \end{cases} \quad (B.1)$$

$$V(E + h\nu) = \begin{cases} 1 & \text{if } E + h\nu > E_C \\ 0 & \text{otherwise} \end{cases} \quad (B.2)$$

$$W(E + U + h\nu) = \begin{cases} 1 & \text{if } E + U + h\nu > E_C \\ 0 & \text{otherwise} \end{cases} \quad (B.3)$$

The following expressions for the individual generation rates in dc mode are obtained using equation (4.36) for a single state at energy E .

- from valence band to the dangling bonds states:

$$G_1^{dc}(E, h\nu) = U(E - h\nu) \phi_{dc} \frac{K}{h\nu} D_{VB}(E - h\nu) D_{dc}^+(E) \quad (B.4)$$

$$G_3^{dc}(E, h\nu) = U(E - h\nu) \phi_{dc} \frac{K}{h\nu} D_{VB}(E - h\nu) D_{dc}^o(E)$$

- from valence band to the tail states:

$$G_5^{dc}(E, h\nu) = U(E - h\nu) \phi_{dc} \frac{K}{h\nu} D_{VB}(E - h\nu) (D_{cbl}(E) - n_t^{dc}(E)) \quad (B.5)$$

$$G_7^{dc}(E, h\nu) = U(E - h\nu) \phi_{dc} \frac{K}{h\nu} D_{VB}(E - h\nu) p_t^{dc}(E)$$

- from dangling bonds states to the conduction band:

$$G_2^{dc}(E, h\nu) = V(E + h\nu) \phi_{dc} \frac{K}{h\nu} D_{CB}(E + h\nu) D_{dc}^o(E) \quad (B.6)$$

$$G_4^{dc}(E, h\nu) = W(E + U + h\nu) \phi_{dc} \frac{K}{h\nu} D_{CB}(E + U + h\nu) D_{dc}^-(E)$$

- from tail states to the conduction band:

$$G_6^{dc}(E, h\nu) = V(E + h\nu) \phi_{dc} \frac{K}{h\nu} D_{CB}(E + h\nu) (D_{vbt}(E) - p_t^{dc}(E)) \quad (B.7)$$

$$G_8^{dc}(E, h\nu) = V(E + h\nu) \phi_{dc} \frac{K}{h\nu} D_{CB}(E + h\nu) n_t^{dc}(E)$$

With:

$$\begin{aligned} n_t^{dc}(E) &= D_{cbt}(E) f_{cbt}^{dc}(E) \\ p_t^{dc}(E) &= D_{vbt}(E) f_{vbt}^{dc}(E) \\ D_{dc}^+(E) &= D_{db}(E) f_{dc}^+(E) \\ D_{dc}^o(E) &= D_{db}(E) f_{dc}^o(E) \\ D_{dc}^-(E) &= D_{db}(E) f_{dc}^-(E) \end{aligned} \quad (B.8)$$

where D_{CB} is the density of states in the conduction band assumed totally empty, and D_{VB} is the density of states in the valence band assumed totally occupied. The expressions presented above can be generalized to the case of a continuous distribution of localized states within the mobility gap (a-Si:H based materials) by integrating these expressions over the gap state energy from E_V to E_C .

Appendix C

Expressions of the coefficients of the dc occupation functions

The expressions of the dc occupation functions coefficients involved in equations (4.26) to (4.28) of chapter 4 are:

$$\begin{aligned}
 tt_1 &= n_{dc} C_n^+ + C_p^o p_1^o(E) + \phi_{dc} \frac{K}{h\nu} D_{VB}(E - h\nu) \\
 tt_2 &= p_{dc} C_p^o + C_n^+ n_1^+(E) + \phi_{dc} \frac{K}{h\nu} D_{CB}(E + h\nu) \\
 tt_3 &= p_{dc} C_p^- + C_n^o n_1^o(E) + \phi_{dc} \frac{K}{h\nu} D_{CB}(E + U + h\nu) \\
 tt_4 &= n_{dc} C_n^o + C_p^- p_1^-(E) + \phi_{dc} \frac{K}{h\nu} D_{VB}(E - h\nu) \\
 tt_5 &= n_{dc} C_n^c + C_p^c p_1^c(E) + \phi_{dc} \frac{K}{h\nu} D_{VB}(E - h\nu) \tag{C.1} \\
 tt_6 &= n_{dc} C_n^c + C_p^c p_1^c(E) + \phi_{dc} \frac{K}{h\nu} D_{VB}(E - h\nu) + p_{dc} C_p^c + C_n^c n_1^c(E) + \phi_{dc} \frac{K}{h\nu} D_{CB}(E + h\nu) \\
 tt_7 &= p_{dc} C_p^v + C_n^v n_1^v(E) + \phi_{dc} \frac{K}{h\nu} D_{CB}(E + h\nu) \\
 tt_8 &= n_{dc} C_n^v + C_p^v p_1^v(E) + \phi_{dc} \frac{K}{h\nu} D_{VB}(E - h\nu) + p_{dc} C_p^v + C_n^v n_1^v(E) + \phi_{dc} \frac{K}{h\nu} D_{CB}(E + h\nu)
 \end{aligned}$$

Appendix D

Expression of the thermal transitions in ac mode

With reference to figure 1 and using equation (4.40) & (4.41), the thermal transitions per unit volume and unit time under ac condition illumination have these expressions:

- Dangling bonds:

$$\begin{aligned}
 T_1^{ac}(E, \omega) &= C_n^+ (n_{dc} D_{ac}^+(E, \omega) + n_{ac}(\omega) D_{dc}^+(E) + n_{ac}(\omega) D_{ac}^+(E, \omega)) \\
 T_2^{ac}(E, \omega) &= C_n^o (n_{dc} D_{ac}^o(E, \omega) + n_{ac}(\omega) D_{dc}^o(E) + n_{ac}(\omega) D_{ac}^o(E, \omega)) \\
 T_3^{ac}(E, \omega) &= C_n^+ n_1^+(E) D_{ac}^o(E, \omega) \\
 T_4^{ac}(E, \omega) &= C_n^o n_1^o(E) D_{ac}^-(E, \omega) \\
 T_5^{ac}(E, \omega) &= C_p^o (p_{dc} D_{ac}^o(E, \omega) + p_{ac}(\omega) D_{dc}^o(E) + p_{ac}(\omega) D_{ac}^o(E, \omega)) \\
 T_6^{ac}(E, \omega) &= C_p^- (p_{dc} D_{ac}^-(E, \omega) + p_{ac}(\omega) D_{dc}^-(E) + p_{ac}(\omega) D_{ac}^-(E, \omega)) \\
 T_7^{ac}(E, \omega) &= C_p^o p_1^o(E) D_{ac}^+(E, \omega) \\
 T_8^{ac}(E, \omega) &= C_p^- p_1^-(E) D_{ac}^o(E, \omega)
 \end{aligned} \tag{D.1}$$

- Tail states:

$$\begin{aligned}
 T_9^{ac}(E, \omega) &= C_n^c (n_{ac}(\omega) (D_{cvt}(E) - n_t^{dc}(E) - n_t^{ac}(E, \omega)) - n_{dc} n_t^{ac}(E, \omega)) \\
 T_{10}^{ac}(E, \omega) &= C_n^c n_1(E) n_t^{ac}(E, \omega) \\
 T_{11}^{ac}(E, \omega) &= C_p^v p_1(E) p_t^{ac}(E, \omega) \\
 T_{12}^{ac}(E, \omega) &= C_p^c (p_{ac}(\omega) (D_{vbt}(E) - p_t^{dc}(E) - p_t^{ac}(E, \omega)) - p_{dc} p_t^{ac}(E, \omega)) \\
 T_{13}^{ac}(E, \omega) &= C_p^c p_1(E) (D_{cvt}(E) - n_t^{ac}(E, \omega)) \\
 T_{14}^{ac}(E, \omega) &= C_p^c (p_{dc} n_t^{ac}(E, \omega) + p_{ac}(\omega) n_t^{dc}(E) + p_{ac}(\omega) n_t^{ac}(E, \omega)) \\
 T_{15}^{ac}(E, \omega) &= C_n^v n_1(E) (D_{vbt}(E) - p_t^{ac}(E, \omega)) \\
 T_{16}^{ac}(E, \omega) &= C_n^c (n_{dc} p_t^{ac}(E, \omega) + n_{ac}(\omega) p_t^{dc}(E) + n_{ac}(\omega) p_t^{ac}(E, \omega))
 \end{aligned} \tag{D.2}$$

Appendix E

Expression of the photogeneration rates in ac mode

Referring to figure 2 & 3 and using equation (4.42), the ac component of the individual photogeneration rates from valence band to localized states are determined by:

$$\begin{aligned}
 G_1^{ac}(E, h\nu, \omega) &= \frac{K}{h\nu} D_{VB}(E - h\nu) (\phi_{dc} D_{ac}^+(E, \omega) + \phi_{ac} D_{dc}^+(E) + \phi_{ac} D_{ac}^+(E, \omega)) \\
 G_3^{ac}(E, h\nu, \omega) &= \frac{K}{h\nu} D_{VB}(E - h\nu) (\phi_{dc} D_{ac}^o(E, \omega) + \phi_{ac} D_{dc}^o(E) + \phi_{ac} D_{ac}^o(E, \omega)) \\
 G_5^{ac}(E, h\nu, \omega) &= \frac{K}{h\nu} D_{VB}(E - h\nu) \begin{pmatrix} \phi_{ac} (D_{cbl}(E) - n_t^{dc}(E)) \\ -\phi_{dc} n_t^{ac}(E, \omega) - \phi_{ac} n_t^{ac}(E, \omega) \end{pmatrix} \\
 G_7^{ac}(E, h\nu, \omega) &= \frac{K}{h\nu} D_{VB}(E - h\nu) (\phi_{dc} p_i^{ac}(E, \omega) + \phi_{ac} p_i^{dc}(E) + \phi_{ac} p_i^{ac}(E, \omega))
 \end{aligned} \tag{E.1}$$

By the same procedure, the individual ac photogeneration rates from localized states to the conduction band are given by:

$$\begin{aligned}
 G_2^{ac}(E, h\nu, \omega) &= \frac{K}{h\nu} D_{CB}(E + h\nu) (\phi_{dc} D_{ac}^o(E, \omega) + \phi_{ac} D_{dc}^o(E) + \phi_{ac} D_{ac}^o(E, \omega)) \\
 G_4^{ac}(E, h\nu, \omega) &= \frac{K}{h\nu} D_{CB}(E + U + h\nu) (\phi_{dc} D_{ac}^-(E, \omega) + \phi_{ac} D_{dc}^-(E) + \phi_{ac} D_{ac}^-(E, \omega)) \\
 G_6^{ac}(E, h\nu, \omega) &= \frac{K}{h\nu} D_{CB}(E + h\nu) \begin{pmatrix} \phi_{ac} (D_{vbl}(E) - p_t^{dc}(E)) \\ -\phi_{dc} p_i^{ac}(E, \omega) - \phi_{ac} p_i^{ac}(E, \omega) \end{pmatrix} \\
 G_8^{ac}(E, h\nu, \omega) &= \frac{K}{h\nu} D_{CB}(E + h\nu) (\phi_{dc} n_t^{ac}(E, \omega) + \phi_{ac} n_t^{dc}(E) + \phi_{ac} n_t^{ac}(E, \omega))
 \end{aligned} \tag{E.2}$$

Where:

$$\begin{aligned}n_t^{ac}(E, \omega) &= D_{cbt}(E) \cdot f_{cbt}^{ac}(E, \omega) \\p_t^{ac}(E, \omega) &= D_{vbt}(E) \cdot f_{vbt}^{ac}(E, \omega) \\D_{ac}^-(E, \omega) &= D_{db}(E) \cdot f_{ac}^-(E, \omega) \\D_{ac}^o(E, \omega) &= D_{db}(E) \cdot f_{ac}^o(E, \omega) \\D_{ac}^+(E, \omega) &= D_{db}(E) \cdot f_{ac}^+(E, \omega)\end{aligned}\tag{E.3}$$

The expressions presented above can be generalized to the case of a continuous distribution of localized states within the mobility gap (a-Si:H based materials) by integrating these expressions over the gap state energy from E_V to E_C .

Appendix F

Expressions of the coefficients of the ac occupation functions

Under small ac signal conditions where the harmonics are neglected, the ac occupation functions f_{cbl}^{ac} , f_{vbt}^{ac} , f_{ac}^+ , f_{ac}^o and f_{ac}^- are deduced from the equations (4.29), (4.30) & (4.31).

We define first, the following parameters related to the dc regime:

$$\begin{aligned}
 I_1 &= D_{VB}(E - h\nu)(1 - f_{cbl}^{dc}(E)) - D_{CB}(E + h\nu)f_{cbl}^{dc}(E) + tt_5 \\
 I_2 &= D_{CB}(E + h\nu)(1 - f_{vbt}^{dc}(E)) - D_{VB}(E - h\nu)f_{vbt}^{dc}(E) + tt_7 \\
 I_3 &= D_{CB}(E + h\nu)f_{dc}^o(E) - D_{VB}(E - h\nu)f_{dc}^+(E) \\
 I_4 &= D_{VB}(E - h\nu)f_{dc}^o(E) - D_{CB}(E + U + h\nu)f_{dc}^-(E)
 \end{aligned} \tag{F.1}$$

The expressions of the coefficients used in ac occupation function equations in chapter 4 are obtained after some manipulation of equations (4.29), (4.30) & (4.31) and given as follow:

- Tail states:

$$\begin{aligned}
 A_{cbl} &= \frac{C_n^c(1 - f_{cbl}^{dc}(E))tt_6 - j\omega C_n^c(1 - f_{cbl}^{dc}(E))}{tt_6^2 + \omega^2} \\
 B_{cbl} &= \frac{-C_p^c f_{cbl}^{dc}(E)tt_6 + j\omega C_p^c f_{cbl}^{dc}(E)}{tt_6^2 + \omega^2} \\
 C_{cbl} &= \frac{g_{ac}I_1tt_6 - j\omega g_{ac}I_1}{tt_6^2 + \omega^2} \\
 A_{vbt} &= \frac{-C_n^v f_{vbt}^{dc}(E)tt_8 + j\omega C_n^v f_{vbt}^{dc}(E)}{tt_8^2 + \omega^2} \\
 B_{vbt} &= \frac{C_p^v(1 - f_{vbt}^{dc}(E))tt_8 - j\omega C_p^v(1 - f_{vbt}^{dc}(E))}{tt_8^2 + \omega^2} \\
 C_{vbt} &= \frac{g_{ac}I_2tt_8 - j\omega g_{ac}I_2}{tt_8^2 + \omega^2}
 \end{aligned} \tag{F.2}$$

- Dangling bonds:

$$\begin{aligned}
A_{db}^+ &= \frac{tt_1 \cdot tt_2 - j \omega tt_2}{tt_1^2 + \omega^2} \\
B_{db}^+ &= \frac{C_p^o f_{dc}^o(E) tt_1 - j \omega C_p^o f_{dc}^o(E)}{tt_1^2 + \omega^2} \\
C_{db}^+ &= \frac{-C_n^+ f_{dc}^+(E) tt_1 + j \omega C_n^+ f_{dc}^+(E)}{tt_1^2 + \omega^2} \\
D_{db}^+ &= \frac{g_{ac} I_3 tt_1 - j \omega g_{ac} I_3}{tt_1^2 + \omega^2} \\
A_{db}^- &= \frac{tt_3 \cdot tt_4 - j \omega tt_4}{tt_3^2 + \omega^2} \\
B_{db}^- &= \frac{-C_p^- f_{dc}^-(E) tt_3 + j \omega C_p^- f_{dc}^-(E)}{tt_3^2 + \omega^2} \\
C_{db}^- &= \frac{C_n^o f_{dc}^o(E) tt_3 - j \omega C_n^o f_{dc}^o(E)}{tt_3^2 + \omega^2} \\
D_{db}^- &= \frac{g_{ac} I_4 tt_3 - j \omega g_{ac} I_4}{tt_3^2 + \omega^2} \\
A_{db}^o &= -\frac{C_{db}^+ + C_{db}^-}{1 + A_{db}^+ + A_{db}^-} \\
B_{db}^o &= -\frac{B_{db}^+ + B_{db}^-}{1 + A_{db}^+ + A_{db}^-} \\
C_{db}^o &= -\frac{D_{db}^+ + D_{db}^-}{1 + A_{db}^+ + A_{db}^-}
\end{aligned} \tag{F.3}$$